AD-A243 286

RL-TR-91-253
Final Technical Report
October 1991

ADAPTIVE PRESORT PROCESSING

North Carolina State University

A. Vanderlugt and Reeder N. Ward

DTIC
ELECTE
DEC 0 5 1991
S D
D

APPROVED FOR PUBLIC RELEASE; DISTRIBUTION UNLIMITED.

91-16629

Rome Laboratory
Air Force Systems Command
Griffiss Air Force Base, NY 13441-5700

91 11 27 031

This report has been reviewed by the Rome Laboratory Public Affairs Office (PA) and is releasable to the National Technical Information Service (NTIS). At NTIS it will be releasable to the general public, including foreign nations.

RL-TR-91-253 has been reviewed and is approved for publication.

APPROVED:

ANDREW R. PIRICH
Program Manager

FOR THE COMMANDER:

JAMES W. YOUNGBERG, Lt Col, USAF
Deputy Director
Surveillance and Photonics Directorate

If your address has changed or if you wish to be removed from the Rome Laboratory mailing list, or if the addressee is no longer employed by your organization, please notify RL6CPA) Griffiss AFB, NY 13441-5700. This will assist us in maintaining a current mailing list.

Do not return copies of this report unless contractual obligations or notices on a specific document require that it be returned.

REPORT DOCUMENTATION PAGE

Form Approved
OMB No. 0704-0188

Public reporting burden for this collection of information is estimated to average 1 hour per response, including the time for reviewing instructions, searching existing data sources, gathering and maintaining the data needed, and completing and reviewing the collection of information. Send comments regarding this burden estimate or any other aspect of this collection of information, including suggestions for reducing this burden, to Washington Headquarters Services, Directorate for Information Operations and Reports, 1215 Jefferson Davis Highway, Suite 1204, Arlington, VA 22202-4302, and to the Office of Management and Budget, Paperwork Reduction Project (0704-0188), Washington, DC 20503.

1. AGENCY USE ONLY (Leave Blank)	2. REPORT DATE	3. REPORT TYPE AND DATES COVERED
	October 1991	Final Feb 90 - Apr 91

4. TITLE AND SUBTITLE

ADAPTIVE PRESORT PROCESSING

5. FUNDING NUMBERS

C - F30602-88-D-0025
PE - 62702F
PR - 4600
TA - P1
WU - P8

6. AUTHOR(S)

A. Vanderlugt and Reeder N. Ward

7. PERFORMING ORGANIZATION NAME(S) AND ADDRESS(ES)

North Carolina University
Raleigh, North Carolina 27695

8. PERFORMING ORGANIZATION REPORT NUMBER

9. SPONSORING/MONITORING AGENCY NAME(S) AND ADDRESS(ES)

Rome Laboratory (OCPA)
Griffiss AFB NY 13441-5700

10. SPONSORING/MONITORING AGENCY REPORT NUMBER

RL-TR-91-253

11. SUPPLEMENTARY NOTES

RL Project Engineer: Dr. George A. Brost/OCPA/(315) 330-7669
Prime Contractor: Georgia Inst. of Technology, 206 O'Keefe Bldg., Atlanta, GA 30332-0490

12a. DISTRIBUTION/AVAILABILITY STATEMENT

Approved for public release; distribution unlimited.

12b. DISTRIBUTION CODE

13. ABSTRACT (Maximum 200 words)

This report summarizes analysis and experiments of an optical signal processing architecture which excises narrow components from wideband signals using frequency plane excision. It is shown that area detection in the frequency plane is equivalent to point detection in the image plane. The design, construction, and testing of a detection system that obtains the Fourier transform of the wideband signal and adaptively searches for strong narrowband components are described. Computer simulations and experimental results of pulsed experiments are presented.

14. SUBJECT TERMS

Acousto-optics, Signal Excision, Notch Filtering, Optical Signal Processing

15. NUMBER OF PAGES

122

16. PRICE CODE

17. SECURITY CLASSIFICATION OF REPORT	18. SECURITY CLASSIFICATION OF THIS PAGE	19. SECURITY CLASSIFICATION OF ABSTRACT	20. LIMITATION OF ABSTRACT
UNCLASSIFIED	UNCLASSIFIED	UNCLASSIFIED	UNL

Table of Contents

List of Figures....iv

List of Symbols....vii

1. Introduction....1

2. Optical Signal Processing Fundamentals....4

2.1 Discussion of signals....4

2.2 The optical Fourier transform....5

2.3 Spatial light modulators....7

2.3.1 Acousto-optic spatial light modulators....8

2.3.2 Angle of deflection....10

2.4 Simple spectrum analysis....10

3. Signal excision....13

3.1 The heterodyne transform....13

3.1.1 Detection in the Fourier plane....15

3.1.2 Detection in the image plane....16

3.2 Notch filtering in the frequency plane....17

3.3 Problem description of point detection versus area detection....19

3.3.1 Derivation of the photocurrent using an area detector in the Fourier plane....20

3.3.2 Derivation of the photocurrent using an area detector in the image plane....21

3.4 Derivation of the photocurrent using a point detector in the image plane....23

3.5 The effect of the detection schemes on the signal-to-noise ratio....25

3.6 Discussion and conclusions....26

4. Presort Processor modification....28

4.1 Description of the Presort Processor....28

4.1.1 TeO_2 longitudinal phased array acousto-optic cell....29

4.1.2 Spatial light modulators 30

4.2 Modification of the Presort Processor 31

4.2.1 Calculation of the required clear aperture 31

4.2.2 Displacement of the second surface reflected wave 32

4.2.3 Analysis of the second surface reflection 34

4.2.4 Effect of the wedge of the optical window at the spatial light modulators 37

4.2.5 Analysis of a shifted signal 37

4.3 Measurements on the optical window 39

4.4 Insertion of the optical window into the Presort Processor 40

4.5 Calculation of the Fourier lens focal length 43

4.5.1 Fourier lens calculation 44

4.5.2 Design an placement of the Fourier transform lenses 45

4.5.3 Image direction calculations 45

4.6 Introduction to the post-processing electronics 46

4.6.1 Description of the post-processing electronics 46

4.6.2 Adaptation mode 47

4.6.3 Operator interaction mode and visual display 48

4.6.4 Excising algorithm 48

4.7 Experimental results 50

5. Pulse Experiments 52

5.1 Signal excision 52

5.2 Computer simulations and experimental results: removing selected frequency components of pulses 52

5.3 Measure of distortion 54

5.3.1 System limitations due to the components 54

5.3.2 The removal of symmetric frequency components on a 78 ns pulse..... 55

5.3.3 The removal of symmetric frequency components on a 468 ns pulse..... 59

5.4 Symmetric removal of the sidelobes of the sinc function.....61

5.5 How many sidelobes make a good pulse?..... 62

5.6 Introduction to narrowband interference experiments..... 62

5.6.1 Excision of a narrowband interferer.....63

5.6.2 Notching capability of the Presort Processor..... 63

5.7 Root mean square error of pulse after a narrowband interferer is excised.....64

6. Conclusions..... 65

7. References..... 66

8. Figures..... 68

Accession For
NTIS GRA&I
DTIC TAB
Unannounced
Justification
By
Distribution/
Availability Codes
Dist
A-1

List of Figures

2.1a Representation of time window of the Fourier transform....68

2.1b Spectrum of received signal....68

2.2 Optical Fourier transform system....69

2.3 Parameters of an acousto-optic cell....69

2.4 Raman-Nath mode of operation....70

2.5 Bragg mode of operation....70

2.6 Relationships of the acousto-optic cells....71

2.7 Fourier transform configuration....71

3.1 Area detection in the Fourier plane....72

3.2 Point detection in the image plane....72

3.3 Wideband spectrum corrupted by narrowband interferers....73

3.4 Notch filter response....73

3.5 Notch filter and interferer....74

3.6 Sinc function with mainlobe excised....74

3.7 Output image plane with mainlobe of sinc function excised....75

3.8 Output image plane with various sidelobes of the sinc function excised....75

4.1 Presort Processor....76

4.2 Passband of the signal acousto-optic cell....76

4.3 Spatial light modulators....77

4.4 The theoretical notch shape....77

4.5 Presort Processor modified....78

4.6 Representation of the displacements of the optical beams....78

4.7 Amplitude and phase reponse of the Presort Processor....79

4.8 Phase response after the optical window is inserted into the Presort Processor....79

4.9 Amplitude reponse before and after the optical window is inserted..... 80

4.10 Phase response after the corrective optical window is inserted..... 81

4.11 Pulse before the primary optical window is inserted, after the primary optical window is inserted, and after the corrective optical window is inserted..... 81

4.12 Fourier transform direction of the optical system.....82

4.13 Image direction of the optical system.....82

4.14 Block diagram of the digital system..... 83

4.15 Spectrum of a signal distorted by narrowband interferers..... 83

4.16 The display with one narrowband interferer excised..... 84

4.17 Experimental setup for the testing of the post-processing electronics..... 84

4.18 The spectrum with the threshold level at a steady-state value..... 85

4.19 The spectrum with two different strength interferers with the threshold at a steady state value..... 85

4.20 The spectrum with multiple narrowband interferers.....86

5.1 Block diagram of the experimental system..... 86

5.2 Experimental equipment setup..... 87

5.3 Signal that is available on a one-shot basis..... 87

5.4 Examples of various frequency components removed from a sinc function.....88

5.5 Computer simulation: root mean error versus spatial light modulators 89

5.6 Experimental results: root mean square error versus spatial light modulators elements.....89

5.7 Spectrum of the 78 ns pulse.....90

5.8 The experimental reference pulse..... 90

5.9 The 78 ns pulse with the d.c. value removed..... 91

5.10 The 78 ns pulse with a symmetric removal of frequency components..... 92

5.11 The 78 ns pulse with a symmetric removal of frequency components in the sidelobes.....93

5.12 Spectrum of the 468 ns pulse.....93

5.13 Root mean square error of the 468 ns pulse.....94

5.14 The 468 ns pulse when the three centered spatial light modulator elements are switched.....95

5.15 The reference 100 ns pulse.....96

5.16 The 100 ns pulse when the second sidelobes are removed.....96

5.17 The 100 ns pulse with the sixth sidelobes removed.....97

5.18 The experimental 100 ns pulse with various sidelobes removed.....98

5.19 The computer simulations of the 100 ns pulse with various sidelobes removed.....99

5.20 The 100 ns pulse with seven sidelobes.....100

5.21 The experimental 100 ns pulse with five sidelobes.....100

5.22 The experimental setup for the narrowband interference experiments.....101

5.23 The reference pulse for the narrowband interference experiments.....101

5.24 The spectrum of the pulse plus the narrowband interferer.....102

5.25 The pulse plus the narrowband interferer after demodulation.....102

5.26 The pulse with the narrowband interferer excised.....103

5.27 The pulse with the narrowband interferer at 304.5 MHz excised.....103

5.28 Spectrum of the pulse plus the narrowband interferer in the mainlobe.....104

5.29 The root mean square error versus spatial light modulator elements with the narrowband interferer in the mainlobe.....104

5.30 The pulse plus the narrowband interferer 2 MHz from the modulating frequency...105

5.31 The pulse with the narrowband interferer excised: RMSE=0.15.....105

List of Symbols

$a(x)$	optical amplitude function
A_j	amplitude of narrowband interferer
B	processing bandwidth
b	second surface reflection coefficient divided by the second surface reflection coefficient
CA	clear aperture
d_o	frequency plane spot size
e	charge of an electron
f	temporal frequency of signal
f_c	temporal carrier frequency
f_j	temporal frequency of narrowband interferer
$f(x,t)$	optical and temporal representation of signal emerging from the acousto-optic cell
F	lens focal length
$F(\alpha,t)$	Fourier transform of signal beam
$g(t)$	photodetector current
$g(w)$	representation of a positive spherical lens
$g(x)$	light reflected from the optical window
h	height of rays in optical system
$H(\alpha)$	amplitude transmittance of frequency plane spatial light modulators
i_s	photodetector signal current
i_{sa}	average photodetector signal current
$I(\alpha,t)$	spatial intensity

$j(t)$	narrowband interferer
L	length of acousto-optic cell
n	index of refraction
$p(u)$	photodetector aperture function
Q	Q factor
R_L	load resistance of photodetector
r_p	reflection coefficient
$r(x)$	reference beam
$R(\alpha)$	Fourier transform of reference beam
RMS	root mean square value
RMSE	root mean square error
t	time
T	time aperture of acousto-optic cell
T_k	temperature in degrees Kelvin
t_{oa}	thickness of optical window
W	bandwidth of signal
x_0	distance from optical axis the point source is located
Z	thickness of acousto-optic cell
α	spatial frequency
α_{co}	spatial frequency
Λ	acoustic wavelength
λ	optical wavelength
ξ	spatial variable
θ	angle an optical wave makes with optical axis

θ_1	incident angle
θ_2	transmitted angle
φ	parallelism

I. Introduction

The trend in communication systems is towards processing larger bandwidth signals. As the bandwidth of the signal increase, the fundamental operations on the signal become more computationally intensive. Optical signal processing systems have a natural parallel structure, so that many computations can be done simultaneously, therefore reducing the signal processing time. For example, a 1024x1024 point Fourier transform of a complex signal can be computed optically in the time it takes light to traverse a fraction of a meter, or about 1 nanosecond.

As the spectral environment becomes more congested, wide bandwidth systems are frequently corrupted by narrowband interference. The narrowband interference could be intentional, or it could be some FM radio energy corrupting a wideband satellite message. We desire to excise the narrowband interference in order to recover the intended signal. Since the optical Fourier transform exist as a spatial light distribution that is physically accessible, we can use spatial light modulators to physically block the undesired light, or narrowband interferers, in the Fourier transform plane. In optical signal processing we use acousto-optic cells to spatially and temporally modulate light in real-time to handle signals having bandwidths that range from 50 MHz to 2 GHz.

In the early 1980's Erickson [1-3] performed analyses and experiments dealing with signal excision. His main interest was in finding the notch shape and depth as various parameters of his optical signal processor were varied. He used wires in the frequency plane as spatial light modulators to perform the excision. In 1980 Lee *et al.* [4] reported on experiments in which they used a threshold detector array to control spatial light modulators in the frequency plane. They used a PLZT ceramic electro-optic modulator in which 18 dB of excision was attained, and 23 dB when an opaque light block was used. In 1982 Roth [5] reported that he used an array of wideband photodiodes in the frequency plane to perform notch filtering; a maximum notch depth of 35 dB was attained. Anderson *et al.* [6] were the first to demonstrate excision using a GaAs photodetector array. They obtained a 40 dB excision depths, therefore making the array useful for

correlation operations in optical adaptive filters.

Bandstetter and Grieve [7-8] built an optical notching filter that uses a recursive technique to obtain the final notch depth. They used a programmable spatial filter in which liquid crystal fingers block the undesired light. Their experiments involves passing an RF pulse through their optical excisor and examining the effect their system has on the pulse; they also added narrowband interferers to the pulse, excised them using their recursive architecture, and then examined the output pulse at RF.

The Presort Processor is an optical signal processor, developed by the Harris Corporation, to excise narrowband interference from wideband signals using frequency plane excision. The Presort Processor is located at Rome Air Development Center, where it is maintained in the Photonics Center. The frequency plane excision is performed by a pair of multi-channel acousto-optic devices currently controlled by a bank of switches. We have designed and constructed a detection, processing, and control system so that the notching can eventually be automated.

The major objective of our work is to modify the Presort Processor so that the frequency excision is open-loop adaptive. Our major accomplishments are:

- the design, construction, and testing of a detection system that obtains the Fourier transform of a wideband signal.
- the design, construction, and testing of a system that adaptively searches a wideband spectrum for narrowband interferers.
- an analysis of area detection in the Fourier plane versus point detection in the image plane of optical processors.
- the effect of excising narrowband interference from wideband signals is studied by simulating the removal of symmetric frequency components of a pulse at an intermediate frequency, and analyzing the pulse shapes at baseband; these computer simulations are confirmed experimentally by utilizing the Presort Processor.

- the operation of the Presort Processor is demonstrated by adding a narrowband interferer to a pulse, excising the interferer at an intermediate frequency, and examining the distortion on the pulse at baseband.

In Chapter 2, we give a discussion of optical signal processing fundamentals; this includes (1) a discussion of wideband signals and advantageous processing architectures, (2) a derivation of the optical Fourier transform, (3) a brief discussion of spatial light modulators with insight into desirable real-time spatial light modulators, and (4) an example of an optical spectrum analyzer. In Chapter 3, we derive the output photocurrent for the optical architecture on which the Presort Processor is based. We then show that area-detection in the frequency plane is equivalent to point-detection in the image plane. In Chapter 4, we describe the Presort Processor in detail, design a system that searches for narrowband interferers in wideband spectrums, and give experimental results of the system. In Chapter 5, we present computer simulations and experimental results of pulse experiments where we used the Presort Processor to notch various frequency components. In Chapter 6, we present our conclusions and suggestions for future work in this area.

2. Optical Signal Processing Fundamentals

In this chapter we explore some of the fundamental concepts of optical signal processing. First, a discussion of signal characteristics is presented with some insight into real-time, large bandwidth processing systems. Second, we develop the optical Fourier transform. Third, we examine spatial light modulators and discuss which ones are useful for real-time signal processing. Finally, we provide an example of an optical spectrum analyzer.

2.1 Discussion of signals

The trend in communication systems is towards processing larger bandwidth signals. As the bandwidth of the signal increase, the fundamental operations on the signal become more computationally intensive. One measure of the complexity of a signal is its time bandwidth product. The time bandwidth product is given by TW, where T and W are the duration and bandwidth of the signal, respectively. The minimum number of samples needed to accurately represent any finite duration, band limited signal is N=2TW, based upon the Nyquist sampling rate. Therefore, a signal that has a short duration and a narrow bandwidth is less complex than a signal that is of long duration and large bandwidth (i.e. N is larger for the latter case).

Computers have yet to provide real-time processing of signals that have large time-bandwidth products. To process a signal which has a time-bandwidth product, TW, in real-time, TW operations must be completed in T_0 seconds, where $T_0=1/2W$ to satisfy the Nyquist sampling rate. Therefore $TW/T_0=2TW^2$ operations must be completed to process signals in real-time. A parallel architecture is advantageous for processing complex signals in real-time; the time required to complete a particular task is significantly reduced by doing many operations in parallel. Optical signal processing systems have a natural parallel structure, so that many computations can be done optically that are cumbersome, or impossible, to do digitally. For example, a 1024x1024 point Fourier transform of a complex signal can be computed optically in the time it takes light to traverse a fraction of a meter, which is about 1 nanosecond.

The spectrum of a signal often contains important information about the signal. The Fourier transform provides a way of obtaining the spectrum of a signal. The continuous time Fourier transform integral is given by

$$F(f,t) = \int_{t-T}^{t} f(z) e^{-j2\pi f z} dz, \tag{2.1}$$

where F(f,t) is the frequency spectrum, evaluated at time t over the past T seconds of signal history, and f(z) is the signal. Notice that the spectrum is computed over a sliding time interval of duration T. We represent the Fourier transform in this form because the spectrum of a signal needs to be computed "on the fly" for real-time signal processing. In real-time systems the signal slides through the time window, T, so that an instantaneous spectrum is computed. Figures 2.1a and 2.1b show a representation of the sliding time window and the corresponding instantaneous spectrum.

We give a simple example to gain further insight into how real-time systems operate. In Figure 2.1a we show a signal that is received from a radio station in which the message is spread over a wide bandwidth using a spread spectrum technique before transmission; e.g. the radio message could be a song named "Nothing Compares 2 U" by Sinead O'Conner. The song is distorted due to narrowband interference encountered during transmission. To listen to her song, we need to compute the spectrum of the signal, and remove, or excise, the narrowband interferers.

For this process to be accomplished in real-time, the spectrum of the signal must be continuously displayed and the narrowband interferers excised as they appear. Therefore, the spectrum, shown in Figure 2.1b, of a section of the signal (T seconds) is computed. The narrowband interferers are excised, using spatial light modulators, and the signal is then demodulated to obtain the message. We therefore need a system that displays the spectrum of a signal instantaneously; we now show how the optical Fourier transform meets our needs for real-time processing.

2.2 The optical Fourier transform

Figure 2.2 shows a system that computes the optical Fourier transform. For convenience

we set the lens one focal length away from the object and the Fourier planes. Let f(x), which is in plane P_1, be illuminated by monochromatic light of wavelength λ ; note that f(x) could be recorded on photographic film or any one of a number of spatial light modulators. First we calculate the light distribution in plane P_2 due to the signal f(x). From Goodman [9], we know that the light distribution at plane P_2 is the Fresnel transform of f(x), given by :

$$g(w) = \int_{P_1} f(x) e^{-j\frac{\pi}{\lambda F}(w-x)^2} dx, \tag{2.2}$$

where the scaling factors of the Fresnel transform have been ignored. We know that a positive spherical lens is represented by the function,

$$g(w) = e^{j\frac{\pi}{\lambda F}w^2}, \tag{2.3}$$

where F is the focal length, and λ is the wavelength of the light source. Therefore, the light distribution at plane P_3 is given by,

$$m(w) = g(w)h(w) = e^{j\frac{\pi}{\lambda F}w^2} \int_{P_1} f(x) e^{-j\frac{\pi}{\lambda F}(w-x)^2} dx. \tag{2.4}$$

Expanding the exponential and simplifying m(w) leads to

$$m(w) = \int_{P_1} f(x) e^{-j\frac{\pi}{\lambda F}(-2xw+x^2)} dx. \tag{2.5}$$

We find the light distribution at plane P_4 by invoking the Fresnel transform on m(w) from plane P_3 to P_4 :

$$m(w) = \int_{P_1} f(x) e^{-j\frac{\pi}{\lambda F}(\xi-w)^2} dx. \tag{2.6}$$

Substituting equation (2.5) into (2.6) we get,

$$F(\xi) = \int_{P_3} \left[\int_{P_1} f(x) e^{-j\frac{\pi}{\lambda F}(-2xw+x^2)} dx \right] e^{-j\frac{\pi}{\lambda F}(\xi-w)^2} dw. \tag{2.7}$$

Expanding and rearranging equation (2.7) we find that

$$F(\xi) = \int_{P_3} \int_{P_1} f(x) e^{-j\frac{\pi}{\lambda F}(\xi^2-2xw+x^2+w^2-2\xi w)} dx dw, \tag{2.8}$$

and, by combining terms in the exponential, we write equation (2.8) as

$$F(\xi) = \int_{P_3} \int_{P_1} f(x) e^{-j\frac{\pi}{\lambda F}(\xi^2-2w(x+\xi)+x^2+w^2)} dx dw. \tag{2.9}$$

We rewrite the exponential term to complete the square with respect to the w variable to get

$$F(\xi)=\int_{P_3}\int_{P_1} f(x)e^{-j\frac{\pi}{\lambda F}(w^2-2w(x+\xi)+(x+\xi)^2-(x+\xi)^2+x^2+\xi^2)}dxdw. \tag{2.10}$$

We change the order of integration and expand the exponential to reveal that

$$F(\xi)=\int_{P_1} f(x)\left[\int_{P_3} e^{-j\frac{\pi}{\lambda F}(w-(\xi+x))^2}dw\right]e^{-j\frac{\pi}{\lambda F}(-x^2-\xi^2+x^2+\xi^2-2x\xi)}dx. \tag{2.11}$$

Equation (2.11) is rearranged as,

$$F(\xi)=\int_{P_1} f(x)\left[\int_{P_3} e^{-j\frac{\pi}{\lambda F}(w-\xi-x)^2}dw\right]e^{j\frac{2\pi}{\lambda F}x\xi}dx. \tag{2.12}$$

This result is result is similar to the Fourier transform, except for the bracketed term. Hence, to put equation (2.11) into standard form, we need to show that the bracketed term is not a function of ξ or x. We do not go through the analysis here; the interested reader can find a more complete analysis by VanderLugt [10].

Hence, if the various scaling factors are ignored, the light distribution in plane P_4, due to a function illuminated by coherent light in plane P_1, is given by,

$$F(\xi)=\int_{P_1} f(x)e^{j\frac{2\pi}{\lambda F}\xi x}dx. \tag{2.13}$$

Notice that this is a one-dimensional Fourier transform integral, where $\xi/\lambda F$ is the spatial frequency and x is the independent variable. Furthermore, we note that, since x is a measure of length, the spatial frequency has units of cycles per unit length.

The two-dimensional Fourier transform integral is a direct extension of equation (2.13) and is given by,

$$F(\xi,\eta)=\int_{P_1}\int f(x,y)e^{j\frac{2\pi}{\lambda F}(\xi x+\eta y)}dxdy. \tag{2.14}$$

Equation (2.14) is useful when dealing with two-dimensional spatial light modulators, such as two-channel orthogonal acousto-optic cells, or with optical image processing.

2.3 Spatial light modulators

We have discussed some of the basic ideas involved with optical signal processing. To process signals optically we need a device that interfaces electrical signals and optical signals (i.e. light distributions). When we need to convert an analog signal to a digital signal, we use an analog

to digital converter; similarly, when converting digital to analog signals, we use a digital to analog converter. In optics we use a spatial light modulator to convert an electrical signal to an optical signal.

Spatial light modulators need the following characteristics to process real-time signals. First, they need a large time bandwidth product and wide dynamic range; the large space bandwidth product ensures that complicated signals can be processed. As with most systems in signal processing, it is advantageous to have linear characteristics over a given range so that linear systems theory applies. A rapid response time is also needed so the spatial light modulators can be updated and refreshed; if the response time is slow, real-time operation is not possible. Good efficiency, phase control, and geometric fidelity are other characteristics which are desirable for a spatial light modulator.

The performance of acousto-optic spatial light modulators is extremely well suited for use in real-time operations. In 1921 Brillouin [11] predicted how light and sound waves would interact. However, it was not until 1932 that Debye-Sears [12] and Lucas-Biquard [13] obtained experimental results. Three years later, in 1935, Raman and Nath [14] mathematically modeled the interaction between light and sound waves. It is worth noting that these experimental results were obtained without the use of a good coherent light source (e.g. a laser), which makes these discoveries even more fascinating. In the late 1950's and early 1960's, the laser was developed and paved the way for better use of spatial light modulators. In the 1970's, some 35 years after Raman and Nath had successfully modeled the phenomenon, spatial light modulators with good optical quality and large bandwidths were developed.

2.3.1 Acousto-optic spatial light modulators

In this section we give a brief discussion of how acousto-optic cells operate. Consider the acousto-optic cell shown in Figure 2.3. Sound waves are used to modulate the light in a linear fashion over a given range. These sound waves are in water, glass, or, as more commonly used

today, an exotic crystal. A piezoelectric transducer is mounted onto one end of the material, and an electrical signal is applied to the transducer. The signal creates an acoustic wave in the material, inducing different pressures in the material. These pressure changes in the material force the density to change, which causes a change in the index of refraction. The index of refraction changes correspond to the applied voltage. In turn, the optical path length changes in the direction of that the light propagates, and the light is phase modulated.

Acousto-optic cells have bandwidths that range from 50 MHz to 2 GHz, depending on the interaction material used. Since the acousto-optic cells cannot support low frequencies, the signal usually is mixed with a local oscillator signal so that the signal falls into the cells frequency range.

The length of the cell with which the light interacts is Z, and L is the length of the cell. In using acousto-optic cells there are two primary modes of operation, the Bragg mode and the Raman-Nath mode. To distinguish between the two modes we define a Q factor:

$$Q = \frac{2\pi}{n_0}\frac{\lambda Z}{\Lambda^2}, \tag{2.15}$$

where λ is the frequency of light, n_0 is the index of refraction of the material, and Λ is the acoustic wavelength inside the acousto-optic cell. If Q>10 the acousto-optic cell is operating in the Bragg mode and if Q<10 the cell is operating in the Raman-Nath mode. Note that

$$\Lambda = \frac{v}{f}, \tag{2.16}$$

where v is the acoustic velocity of the waves inside the cell and f is the frequency applied at the transducer. We substitute equation (2.16) into equation (2.15) yielding,

$$Q = \frac{2\pi}{n_0}\lambda Z\frac{f^2}{v^2}. \tag{2.17}$$

Therefore, the Q factor is proportional to the square of the applied frequency of the signal. We increase the applied frequency of the acousto-optic cell to pass from one mode of operation to another.

The Raman-Nath mode of operation yields several diffracted orders due to the lack of interaction length of the light with the acoustic waves. For most applications, we block all but one diffracted order, using only a small portion of the incident light as depicted in Figure 2.4.

Since good efficiency is desired, the Bragg mode of operation is generally used. Figure 2.5 shows the Bragg mode of operation which yields the undiffracted light and one diffracted order. Since, efficiencies for the Bragg mode can be as high as 90%, this mode is used in practical real-time systems.

2.3.2 Angle of deflection

Let us now examine how the drive frequency, spatial frequency, diffraction angle, and acoustic wavelength are related. Figure 2.6 shows an acousto-optic cell, with the various parameters displayed and how they are related. From equation (2.16) we know how the temporal frequencies relate to the acoustic wavelength within the acousto-optic cell. The spatial frequency is defined as

$$\alpha = \frac{1}{\Lambda}. \tag{2.18}$$

We substitute equation (2.16) into equation (2.18) to get that

$$\alpha = \frac{f}{v}. \tag{2.19}$$

Hence, for every drive frequency f there is a spatial frequency corresponding to the temporal frequency of the signal. The physical angle θ is related to α by the relationship that

$$\theta = \lambda\alpha = \frac{\lambda f}{v}. \tag{2.20}$$

This result further further illustrates how the light is deflected proportional to the applied frequency of the cell, i.e., as the frequency of the signal increases the angle of deflection increases. Therefore, the acousto-optic cell converts the signal into an angular spectrum.

2.4 Simple spectrum analysis

Figure 2.7 shows an optical spectrum analyzer. We assume that the acousto-optic cell is in the Bragg mode of operation, and that the lens is one focal length away. A signal f(t), applied to the transducer of the acousto-optic cell, becomes a traveling pressure wave inside the cell to produce a function of space and time, represented by

$$f(x,t) = f\left(t - \frac{x}{v} - \frac{T}{2}\right), \tag{2.21}$$

where T/2 is a time delay factor due to the optical axis being in the middle of the acousto-optic cell.

We assume that the signal is already in the passband of the cell. The signal completely fills the cell, whose length L is the product of the velocity of the acoustic wave and the transit time of the cell T: L=vT. The light distribution after the acousto-optic cell is given by,

$$s(x,t) = jma(x)f(t - T/2 - x/v), \tag{2.22}$$

where a(x) is the aperture function, and m is the modulation index.

The Fourier transforming property of the lens shows that at plane P_2, we get

$$F(\alpha,t) = \int_{-\frac{L}{2}}^{\frac{L}{2}} f\left(t - \frac{x}{v} - \frac{T}{2}\right) e^{j2\pi\alpha x} dx, \tag{2.23}$$

where the integration is done on the traveling wave over the entirety of the cell, and the aperture function is rectangular; we have ignored the modulation index to illustrate the basic idea. We make a variable substitution by letting

$$u = t - \frac{x}{v} - \frac{T}{2}, \tag{2.24}$$

so that

$$du = -\frac{dx}{v}. \tag{2.25}$$

Hence F(α,t) becomes

$$F(\alpha,t) = \int_{t-T}^{t} f(u) e^{j2\pi f(-u+t-T/2)} (-v du). \tag{2.26}$$

We rearrange equation (2.26) yielding,

$$F(\alpha,t) = -v e^{j(t-T/2)} \int_{t-T}^{t} f(u) e^{j2\pi f u} du. \tag{2.27}$$

Equation (2.27) is the Fourier transform of f(u), where the time window is T seconds in duration. As the signal f(t) completely fills the cell, we recognize that the most recent part of f(t) is at the transducer, while the end of the acousto-optic cell holds the part of the signal that occurred T seconds ago. This explains why the integration is equation (2.27) is over a total time interval of [t-(t-T)]=T seconds.

The spectrum that appears in plane P_2 is called the instantaneous spectrum of f(t) for a couple of reasons. We recall that the most recent part of the signal is at the beginning of the acousto-optic cell and the signal is continuously fed into the cell. The integration is done over time, therefore the spectrum of the T seconds of the signal in the cell appears instantaneously in plane P_2, because the spectrum is computed in the time it takes light to travel less than a meter,

which is about one nanosecond. Since the acousto-optic cells hold a maximum of 50 microseconds of the signal, the spectrum of the signal is available instantaneously.

From this discussion we recognize that an optical system can be implemented to display the instantaneous spectrum of a signal. The time window of the Fourier transform integral slides along the signal which is a desirable quality because we can find the Fourier transform of the signal instantaneously as the signal is received. Hence, if acousto-optic cells are used as the spatial light modulators, the spectrum of wideband signals can be computed in real-time. A more complete discussion of spectrum analysis is given in Chapter 3.

3. Signal Excision

In this chapter we discuss the Mach-Zehnder interferometer when used as an interferometric spectrum analyzer. We derive the heterodyne transform and give an overview of frequency plane notch filtering. We compare image plane detection to Fourier plane detection, and show that the photocurrents for Fourier plane detection and image plane detection using an area photodetector are equal. We show that the cross-product photocurrent, for image plane detection using a point photodetector, is equal to the cross-product photocurrent for Fourier plane detection using an area photodetector, but that the bias photocurrents are not equal. We analyze the effect that the two detection schemes have on the signal-to-noise ratio. Finally, we give a discussion of the effect that the reference beam position has on notch depth.

In Section 2.5 we derived an example of a power spectrum analyzer in which a CCD photodetector array is used to detect the power spectrum of the signal. The photodetector array is a square law device so that the phase of the signal, important in some signal processing applications, is lost. One way of preserving the phase of a signal in optical signal processing is to use heterodyne detection.

To perform heterodyne detection, we add a reference beam to the signal beam, and collect the light onto a wideband photodetector. Figure 3.1 shows an interferometric spectrum analyzer with a signal acousto-optic cell in the bottom branch of the interferometer, and a lens, used to condition the reference beam, in the top branch. In the following examples the reference beam is expressed in terms of its response in plane P_2. The signal and reference beams combine at the beamcombiner, and are Fourier transformed by lens L_4 to plane P_4, where they are collected onto a wideband photodetector.

3.1 The heterodyne transform

Figure 3.1 shows an acousto-optic cell in the lower branch of the interferometer that receives the electrical signal, f(t), and modulates the light in both space and time. The light in the

upper branch of the interferometer passes through a lens at plane P_1 to create a point source at plane P_2. The point source occurs at exactly the same distance from the beam combiner as does the acousto-optic cell. The signal and reference beams combine at the beam combiner, and are Fourier transformed by lens L_4 onto a wideband array photodetector located in plane P_4.

The baseband signal s(t) is translated into the bandpass frequency response of the acousto-optic cell by using a local oscillator, $\cos(2\pi f_c t)$. The positive diffracted order, directly after the acousto-optic cell, is represented by

$$f_+(x,t) = jma(x)s\left(t-\frac{T}{2}-\frac{x}{v}\right)e^{j2\pi f_c\left(t-\frac{T}{2}-\frac{x}{v}\right)}, \tag{3.1}$$

where m is the modulation index, and a(x) is the aperture function. We find the Fourier transform of the signal beam to be

$$F_+(\alpha,t) = \int_{-\infty}^{\infty} jma(x)s\left(t-\frac{T}{2}-\frac{x}{v}\right)e^{j2\pi f_c\left(t-\frac{T}{2}-\frac{x}{v}\right)}e^{j2\pi\alpha x}dx, \tag{3.2}$$

where the Fourier transform is performed with respect to the input spatial variable x. We remove the factors that are not a function of x from the integral to get

$$F_+(\alpha,t) = jme^{j2\pi f_c\left(t-\frac{T}{2}\right)}\int_{-\infty}^{\infty} a(x)s\left(t-\frac{T}{2}-\frac{x}{v}\right)e^{j2\pi x(\alpha-\alpha_c)}dx. \tag{3.3}$$

We now turn our attention to the reference beam, which is a function of x only. Since a point source is created a distance of x_0 from the optical axis in plane P_2, the reference beam is represented by

$$r(x) = \mathrm{sinc}\left[\frac{x-x_0}{d_0}\right], \tag{3.4}$$

where d_0 is the size of the spot, as measured from the centroid of the sinc function to the first zero. We Fourier transform the reference beam to find that

$$R(\alpha) = \mathrm{rect}\left[\frac{\alpha-\alpha_c}{2\alpha_{co}}\right]e^{j2\pi\alpha x_o}, \tag{3.5}$$

where $\alpha_{co}=1/2d_0$, and where the exponential term is generated by the off-axis spot. Also note that we are interested only in the spatial region where the spectrum of the signal and the reference beam are located, which is in the vicinity of α_c.

In optical processors the light can be detected in either the image plane or the Fourier plane,

depending on which one is the most convenient. In Sections 3.1.1 and 3.1.2 we show that the output cross-product photocurrents, when the light is detected in the Fourier plane and image plane, respectively, are equal.

3.1.1 Detection in the Fourier plane

We find the light intensity of the combined beams:

$$I(\alpha,t) = |F_+(\alpha,t)|^2 + |R(\alpha)|^2 + 2\mathrm{Re}\left[F_+(\alpha,t)R^*{}_+(\alpha)\right]. \tag{3.6}$$

A large area photodetector integrates the intensity over the output plane such that the photodetector current, g(t), is given by

$$g(t) = \int_{-\infty}^{\infty} I(\alpha,t)|P(\alpha)|^2 d\alpha, \tag{3.7}$$

where $P(\alpha)$ is the photodetector aperture function. In this analysis we assume that $P(\alpha)$ is uniform over the surface of the photodetector. Since, the intensity bias terms from equation (3.6) are not a function of time, they are rejected by a bandpass filter so that the cross-product photocurrent is given by

$$g_3(t) = 2\mathrm{Re}\left[\int_{-\infty}^{\infty} F_+(\alpha,t)R^*(\alpha)d\alpha\right]. \tag{3.8}$$

We substitute equations (3.3) and (3.5) into equation (3.8) to get

$$g_3(t) = 2\mathrm{Re}\left[jme^{j2\pi f_c\left(t-\frac{T}{2}\right)}\int_{-\infty}^{\infty}\left(\int_{-\infty}^{\infty}\mathrm{rect}\left[\frac{(\alpha-\alpha_c)}{2\alpha_{co}}\right]e^{j2\pi\alpha\,(x-x_o)}d\alpha\right)a(x)s\left(t-\frac{T}{2}-\frac{x}{v}\right)e^{-j2\pi\alpha_c x}dx\right]. \tag{3.9}$$

We evaluate the term inside the parentheses by integrating over α to give

$$F(\alpha) = \left[\frac{e^{j2\pi(\alpha_c+\alpha_{co})(x-x_o)} - e^{j2\pi(\alpha_c-\alpha_{co})(x-x_o)}}{j2\pi(x-x_o)}\right]. \tag{3.10}$$

We simplify equation (3.10) to get

$$F(\alpha) = e^{j2\pi\alpha_c(x-x_o)}\frac{\sin\left[2\pi(x-x_o)\alpha_{co}\right]}{\pi(x-x_o)}. \tag{3.11}$$

Now recall that $d_0=1/2\alpha_{co}$ to give

$$F(\alpha) = \frac{1}{d_o}e^{j2\pi\alpha_c(x-x_o)}\mathrm{sinc}\left(\frac{x-x_o}{d_o}\right). \tag{3.12}$$

We substitute equation (3.12) into equation (3.9) to get

$$g_3(t) = 2\mathrm{Re}\left[jme^{j2\pi f_c\left(t-\frac{T}{2}\right)}\int_{-\infty}^{\infty}\frac{1}{d_o}e^{j2\pi\alpha_c(x-x_o)}\mathrm{sinc}\left(\frac{x-x_o}{d_o}\right)a(x)s\left(t-\frac{T}{2}-\frac{x}{v}\right)e^{-j2\pi\alpha_c x}dx\right]. \tag{3.13}$$

Rearranging equation (3.13), we get that

$$g_3(t) = 2\mathrm{Re}\left[\frac{1}{d_o} jme^{j2\pi f_c\left(t-\frac{T}{2}\right)} e^{-j2\pi\alpha_c x_o)} \int_{-\infty}^{\infty} e^{j2\pi\alpha_c x} \mathrm{sinc}\left(\frac{x-x_o}{d_o}\right) a(x) s\left(t-\frac{T}{2}-\frac{x}{v}\right) e^{-j2\pi x\alpha_c} dx\right]. \tag{3.14}$$

Combining the exponential terms inside the integral we get

$$g_3(t) = 2\mathrm{Re}\left[\frac{1}{d_o} jme^{j2\pi f_c\left(t-\frac{T}{2}\right)} e^{-j2\pi\alpha_c x_o} \int_{-\infty}^{\infty} \mathrm{sinc}\left(\frac{x-x_o}{d_o}\right) a(x) s\left(t-\frac{T}{2}-\frac{x}{v}\right) dx\right]. \tag{3.15}$$

The sinc function is a suitable form of a delta function because no signal information is altered by it in the frequency domain. We therefore apply the sifting property of the delta function to get

$$g_3(t) = 2\mathrm{Re}\left[\frac{1}{d_o} jme^{j2\pi f_c\left(t-\frac{T}{2}\right)} e^{-j2\pi\alpha_c x_o} a(x-x_o) s\left(t-\frac{T}{2}-\frac{x_o}{v}\right)\right]. \tag{3.16}$$

We combine terms and perform the real operation to give,

$$g_3(t) = \frac{2m}{d_o} a(x_o) s\left(t-\frac{T}{2}-\frac{x_o}{v}\right) \cos\left[2\pi f_c\left(t-\frac{T}{2}-\frac{x_o}{v}\right)+\frac{\pi}{2}\right], \tag{3.17}$$

where $g_3(t)$ is proportional to the input signal, s(t), with an associated time delay. We realize that $g_3(t)$ is in the same form as the input double sideband modulation signal, but with some scaling factors. We note that $a(x_0)$ is the aperture function evaluated at the equivalent probe position x_0, f_c is the same frequency as the input carrier, and x_0/v is a time delay which is dependent on the position of the probe. Furthermore, to recover the baseband signal s(t) we need to synchronously demodulate $g_3(t)$. Since we have shown that the signal can be recovered, we therefore can broaden the range of operation and implement arbitrary filter functions, by controlling the shape of the reference beam r(x), or by implementing a frequency plane filter function $R(\alpha)$, both of which can be functions of time.

3.1.2 Detection in the image plane

In this architecture, we detected the light in the Fourier plane of the acousto-optic cell to obtain the signal, however, we now show that we get the same result if the light is detected in the image plane. Figure 3.2 shows the interferometric spectrum analyzer with a point photodetector in the image plane of the acousto-optic cell and the image plane of plane P_2. Since the photodetector

is in the image plane of the acousto-optic cell, we represent the signal beam at the photodetector with

reversed coordinates:

$$f_+(u,t) = jma(-u)s\left(t-\frac{T}{2}+\frac{u}{v}\right)e^{j2\pi f_c\left(t-\frac{T}{2}+\frac{u}{v}\right)}, \tag{3.18}$$

where the various parameters are the same as before. Similarly, we represent the reference beam at the photodetector as

$$r(u) = \operatorname{sinc}\left[\frac{-u-x_0}{d_0}\right]. \tag{3.19}$$

The photodetector integrates the light intensity over its surface, and the bias terms are rejected by a bandpass filter. The cross-product photocurrent term is given by

$$g_3(t) = 2\,\mathrm{Re}\left[\int_{-\infty}^{\infty} f_+(u,t)r^*_+(u)du\right]. \tag{3.20}$$

We substitute equation (3.18) and (3.19) into equation (3.20) to get

$$g_3(t) = 2\,\mathrm{Re}\left[jme^{j2\pi f_c\left(t-\frac{T}{2}\right)}\int_{-\infty}^{\infty} a(-u)s\left(t-\frac{T}{2}+\frac{u}{v}\right)e^{j2\pi f_c\left(\frac{u}{v}\right)}\operatorname{sinc}\left[\frac{-u-x_0}{d_0}\right]du\right]. \tag{3.21}$$

The sinc function is approximated as a delta function to give

$$g_3(t) = 2\,\mathrm{Re}\left[jme^{j2\pi f_c\left(t-\frac{T}{2}\right)}\int_{-\infty}^{\infty} a(-u)s\left(t-\frac{T}{2}+\frac{u}{v}\right)e^{j2\pi f_c\left(\frac{u}{v}\right)}\delta(-u-x_0)du\right]. \tag{3.22}$$

We use the sifting property of the delta function and perform the real operation to get

$$g_3(t) = \frac{2m}{d_o}a(-x_o)s\left(t-\frac{T}{2}+\frac{x_o}{v}\right)\cos\left[2\pi f_c\left(t-\frac{T}{2}+\frac{x_o}{v}\right)+\frac{\pi}{2}\right]. \tag{3.23}$$

Except for the reversal of the spatial coordinates, equation (3.23) is equal to the cross-product photocurrent represented by equation (3.17). The signal is therefore propagating in the opposite direction than in the acousto-optic cell and which does not affect the output detection process. Using this architecture, we can therefore detect the light in either the frequency plane or the image plane of the acousto-optic cell.

3.2 Notch filtering in the frequency plane

Wideband communications systems are frequently corrupted with narrowband interference. The narrowband interference could be intentional or it could be the radio FM band corrupting a

satellite transmission. In any event, the interference corrupts the message at the receiver. We desire to excise the narrowband interference to assist in the recovery of the intended message.

Figure 3.3 shows a wideband spectrum that is corrupted by three narrowband interferers. As discussed before, the Fourier transform exist as a spatial light distribution that is directly accessible. We can therefore use spatial light modulators to physically block, or notch filter, the undesirable light in the Fourier transform plane. Figure 3.4 shows a notching filter function that excises the narrowband interferers. For notch filtering, the ideal spatial light modulator is one that has an infinite on/off ratio and sufficient resolution to notch any width interference signal that is at any position relative to the spatial light modulator elements.

We now derive the general form of the cross-product photocurrent for frequency plane notching. The Fourier transform of the signal is represented by $F(\alpha,t)$, the Fourier transform of the reference beam is $R(\alpha)$, the frequency plane filter is $H(\alpha)$, and the photodetector response is $P(\alpha)$. We collect all the light onto a wideband photodetector, filter the bias terms, and retain the cross-product term to give

$$g_3(t) = 2\,\mathrm{Re}\left\{\int_{-\infty}^{\infty} F(\alpha,t)R^*(\alpha)|H(\alpha)|^2|P(\alpha)|^2 d\alpha\right\}. \tag{3.24}$$

Equation (3.24) gives a general form for the cross-product photocurrent when an arbitrary filter function $H(\alpha)$ is placed in the frequency plane.

As an example, we let the reference beam at the Fourier plane be

$$R(\alpha) = e^{j2\pi\alpha x_0}, \tag{3.25}$$

where $R(\alpha)$ is the Fourier transform of a point source located off-axis by a distance x_0. If we assume a cw interferer at a frequency f_j, the Fourier transform of the signal is

$$F(\alpha,t) = e^{j2\pi f_j\left(t-\frac{T}{2}\right)} A\left(\alpha-\alpha_j\right), \tag{3.26}$$

where $A(\alpha-\alpha_j)$ is the Fourier transform of the illumination function.

$$g_3(t) = 2\,\mathrm{Re}\left\{e^{j2\pi f_j\left(t-\frac{T}{2}\right)}\int_{-\infty}^{\infty} A\left(\alpha-\alpha_j\right)e^{-j2\pi\alpha x_0}|H(\alpha)|^2|P(\alpha)|^2 d\alpha\right\}. \tag{3.27}$$

If we sweep the interferer frequency over the bandwidth of the system, we get a convolution of

$A(\alpha)=\mathrm{sinc}(\alpha L)$ with the magnitude squared of the filter function multiplied by the Fourier transform of the reference beam; $P(\alpha)$ defines the sweep range in terms of spatial frequencies. As Erickson [1] showed, we get some interesting results as we let x_0 vary. Figure 3.5a shows the notch filter and $A(\alpha)$ before the frequency is swept over the band and Figure 3.5b shows the response afterwards. The sidelobe structure of the sinc function shown in Figure 3.5a is caused by the illumination of the signal acousto-optic cell and, more fundamentally, the finite length of the cell. To excise all of the energy at f_j, we need to block the mainlobe plus all of the sidelobes. Blocking all the sidelobe energy is not practical because that would remove too much signal energy. We therefore note that the notch depth is a function of the aperture function, which imposes some fundamental limits on notch depth.

3.3 Problem description of point detection versus area detection

We now explore the differences between point detection in the image plane and area detection in the Fourier plane. Figure 3.1 shows an interferometric spectrum analyzer with a lens in the upper branch and an acousto-optic cell in the lower branch. The signal beam and the reference beam combine at the beamcombiner and are Fourier transformed onto the spatial light modulators, which filter the combined beams, and then are collected onto an area photodetector. The area photodetector collects all light from the signal beam and reference beam. The photodetector integrates the light intensity over its surface producing two bias currents, $g_{1f}(t)$ and $g_{2f}(t)$, and the desired cross-product current $g_{3f}(t)$.

Figure 3.2 shows the same optical signal processor but with the light detected in the image plane of the acousto-optic cell. A point photodetector that is just large enough to accept the reference beam is used to detect the light; the photodetector does not, however, accept all of the signal beam because it is spread over the entire image of the acousto-optic cell. The intensity of the light is integrated over the surface of the photodetector to give the two bias currents, $g_{1i}(t)$ and $g_{2i}(t)$, and the cross-product current $g_{3i}(t)$. It appears that $g_{3f}(t)$ is greater than $g_{3i}(t)$, since less

light is collected by the point photodetector in the image plane. We give an example of a cw interferer to illustrate the apparent discrepancy.

From Section 3.2 we recall that, when the acousto-optic cell is uniformly illuminated, the Fourier transform of a cw signal is a sinc distribution. To successfully notch the cw interferer we remove at least the mainlobe of the sinc function. Figure 3.6 shows the sinc function after the mainlobe is successfully notched, with the area photodetector collecting the energy that is not blocked by the spatial light modulators. We now Fourier transform the sidelobe energy and detect the signal in the image plane of the acousto-optic cell using a point photodetector. Figure 3.7 shows the inverse Fourier transform of the sidelobes of the sinc function with the corresponding point photodetector collecting the light. The point photodetector can therefore be about 1/200 the size of the signal beam in the image plane, since it only needs to be as large as the resolution size of the system, and the acousto-optic cell used in the Presort Processor has a time bandwidth product of 200. We observe that only a small portion of the signal beam in the image plane is detected by the point photodetector. Therefore, it appears that the photocurrents, and hence the notch depths, are different when detecting the light in the Fourier plane as opposed to the image plane. We now show that the cross-product photocurrents are equal and explain the apparent discrepancy.

3.3.1 Derivation of the photocurrent using an area detector in the Fourier plane

We derive the photocurrents when Fourier plane detection is used. We represent the signal directly after the acousto-optic cell as f(x,t), and the reference beam as r(x). We Fourier transform both beams, and represent their Fourier transforms as $F(\alpha,t)$ and $R(\alpha)$. We represent the amplitude transmittance of the spatial light modulator as $H(\alpha)$. After being modified by the spatial light modulator, the signal beam is given by

$$F(\alpha,t)H(\alpha).$$

Similarly, the modified reference beam is represented as

$$R(\alpha)H(\alpha).$$

The intensity of the light incident on the photodetector is

$$I(\alpha,t) = |F(\alpha,t)H(\alpha) + R(\alpha)H(\alpha)|^2. \tag{3.28}$$

We expand equation (3.28) to get

$$I(\alpha,t)=|F(\alpha,t)H(\alpha)|^2+|R(\alpha)H(\alpha)|^2+2\mathrm{Re}\{F(\alpha,t)H(\alpha)R^*(\alpha)H^*(\alpha)\}. \quad (3.29)$$

We integrate the intensity over the photodetector surface to give

$$g(t)=\int_{-\infty}^{\infty} I(\alpha,t)|P(\alpha)|^2 d\alpha, \quad (3.30)$$

where we assume a uniform response over the surface of the photodetector, $P(\alpha)$ equals one in the range of $\alpha_c-\alpha_{co}\leq\alpha\leq\alpha_c+\alpha_{co}$, and is equal to zero elsewhere. We also assume that the signal and the spatial light modulator amplitude transmittance are bandlimited to $\alpha_c-\alpha_{co}\leq\alpha\leq\alpha_c+\alpha_{co}$.

We integrate the signal bias term over the surface of the photodetector to get

$$g_{1f}(t)=\int_{\alpha_c-\alpha_{co}}^{\alpha_c+\alpha_{co}} F(\alpha,t)H(\alpha)F^*(\alpha,t)H^*(\alpha)d\alpha. \quad (3.31)$$

or

$$g_{1f}(t)=\int_{-\infty}^{\infty} |F(\alpha,t)H(\alpha)|^2 d\alpha, \quad (3.32)$$

where we relax the limits of integration to infinity since the signals of interest are bandlimited to $\alpha_c-\alpha_{co}\leq\alpha\leq\alpha_c+\alpha_{co}$. In the following derivations throughout the chapter, we assume that the signals are bandlimited so the photodetector collects all the light, unless otherwise stated. Similarly, we integrate the reference bias term over the surface of the photodetector to give

$$g_{2f}(t)=\int_{-\infty}^{\infty} |R(\alpha)H(\alpha)|^2 d\alpha, \quad (3.33)$$

where the limits on the integration are infinite since all the reference beam and signal beam light is collected. We integrate the cross-product term to get

$$g_{3f}(t)=\int_{-\infty}^{\infty} 2\mathrm{Re}\{F(\alpha,t)H(\alpha)R^*(\alpha)H^*(\alpha)\}d\alpha, \quad (3.34)$$

or

$$g_{3f}(t)=\int_{-\infty}^{\infty} 2\mathrm{Re}\{F(\alpha,t)R^*(\alpha)|H(\alpha)|^2\}d\alpha. \quad (3.35)$$

We have completed the derivation of the photocurrents when Fourier plane detection is used. We now show that the photocurrents represented by equations (3.32), (3.33), and (3.35) are equal to the photocurrents when area detection is used in the image plane.

3.3.2 Derivation of the photocurrents using an area detector in the image plane

We perform a Fourier transform on the filtered beams and detect the light in the image plane. The reference beam in the image plane is represented by

$$\int_{-\infty}^{\infty} R(\alpha)H(\alpha)e^{j2\pi\alpha u}d\alpha, \quad (3.36)$$

where we perform the Fourier transform with respect to the frequency variable α. The signal beam is represented by

$$\int_{-\infty}^{\infty} F(\alpha,t)H(\alpha)e^{j2\pi\alpha u}d\alpha. \tag{3.37}$$

We integrate the intensity over the surface of the area photodetector to get the signal bias term as

$$g_{1i}(t)=\int_{-\infty}^{\infty}\left[2\,\mathrm{Re}\left\{\int_{-\infty}^{\infty}F(\alpha,t)H(\alpha)e^{j2\pi\alpha u}d\alpha\int_{-\infty}^{\infty}F^{*}(\gamma,t)H^{*}(\gamma)e^{-j2\pi\gamma u}d\gamma\right\}\right]du, \tag{3.38}$$

where we have introduced a dummy variable γ in the second integral. We rearrange the integrals to get

$$g_{1i}(t)=2\,\mathrm{Re}\left\{\int_{-\infty}^{\infty}\int_{-\infty}^{\infty}\int_{-\infty}^{\infty}F(\alpha,t)H(\alpha)F^{*}(\gamma,t)H^{*}(\gamma)e^{j2\pi(\alpha-\gamma)u}d\alpha d\gamma du\right\}. \tag{3.39}$$

We integrate over u to get

$$g_{1i}(t)=2\,\mathrm{Re}\left\{\int_{-\infty}^{\infty}\int_{-\infty}^{\infty}F(\alpha,t)H(\alpha)F^{*}(\gamma,t)H^{*}(\gamma)\delta(\alpha-\gamma)d\alpha d\gamma\right\}. \tag{3.40}$$

We use the sifting property of the delta function to get

$$g_{1i}(t)=\int_{-\infty}^{\infty}\left|F(\gamma,t)H(\gamma)\right|^{2}d\gamma. \tag{3.41}$$

We observe that the signal bias term, when image plane detection is used, is equal to the signal bias term when Fourier plane detection is used, since equation (3.41) equals equation (3.32).

We use the same integration technique to find the reference beam bias term:

$$g_{2i}(t)=\int_{-\infty}^{\infty}\left|R(\gamma)H(\gamma)\right|^{2}d\gamma. \tag{3.42}$$

Equation (3.42) is equal to equation (3.33), therefore showing that, when area detection is used in the Fourier plane and area detection is used in the image plane to detect the light, the bias terms are equal.

We now consider the cross-product term which is given by

$$g_{3i}(t)=\int_{-\infty}^{\infty}\left[2\,\mathrm{Re}\left\{\int_{-\infty}^{\infty}F(\alpha,t)H(\alpha)e^{j2\pi\alpha u}d\alpha\int_{-\infty}^{\infty}R^{*}(\gamma)H^{*}(\gamma)e^{-j2\pi\gamma u}d\gamma\right\}\right]du. \tag{3.43}$$

We rearrange the order of integration in equation (3.43) to get

$$g_{3i}(t)=2\,\mathrm{Re}\left\{\int_{-\infty}^{\infty}\int_{-\infty}^{\infty}\int_{-\infty}^{\infty}F(\alpha,t)H(\alpha)R^{*}(\gamma)H^{*}(\gamma)e^{j2\pi(\alpha-\gamma)u}d\alpha d\gamma du\right\}. \tag{3.44}$$

We perform the integration over u to get

$$g_{3i}(t)=2\,\mathrm{Re}\left\{\int_{-\infty}^{\infty}\int_{-\infty}^{\infty}F(\alpha,t)H(\alpha)R^{*}(\gamma)H^{*}(\gamma)\delta(\alpha-\gamma)d\alpha d\gamma\right\}. \tag{3.45}$$

We now use the sifting property of the delta function as we integrate over α to get

$$g_{3i}(t) = 2\,\mathrm{Re}\left\{\int_{-\infty}^{\infty} F(\gamma,t)H(\gamma)R^*(\gamma)H^*(\gamma)d\gamma\right\}. \tag{3.46}$$

Equation (3.46) equals equations (3.35), we therefore have shown that if all the light is collected, frequency plane detection and image plane detection are equivalent.

3.4 Derivation of the photocurrents using a point detector in the image plane

In the previous derivations we relaxed the limits of integration to infinity since all the light is collected. We recall that a *point* photodetector in the image plane is sufficient to collect all the light for which the reference and signal beams overlap. The point photodetector in the image plane does not, however, accept all of the signal beam, and we cannot set the limits of integration to infinity. In the following derivation, we begin by letting the photodetector have a width of L, where L is large enough to collect all the reference beam and signal beam; L is the length of the acousto-optic cell. The cross-product photocurrent in the image plane is given by

$$g_{3i}(t) = \int_{-\frac{L}{2}}^{\frac{L}{2}}\left[2\,\mathrm{Re}\left\{\int_{-\infty}^{\infty} F(\alpha,t)H(\alpha)e^{j2\pi\alpha u}d\alpha\int_{-\infty}^{\infty} R^*(\gamma)H^*(\gamma)e^{-j2\pi\gamma u}d\gamma\right\}\right]du, \tag{3.47}$$

where we represent the first integral by f′(u,t) and the second Fourier integral by r′(u). The cross-product photocurrent is then represented as

$$g_{3i}(t) = 2\,\mathrm{Re}\left\{\int_{-\frac{L}{2}}^{\frac{L}{2}} f'(u,t)r'(u)du\right\}, \tag{3.48}$$

where equation (3.48) is equal to equation (3.35), since L accepts all the light in the reference and signal beams. We recall that, by definition, we obtain a cross-product photocurrent where the signal beam and reference beam overlap. Since the reference beam is much smaller than the signal beam, we can let the size of the photodetector shrink to W, where W equals the extent of the reference beam and W<<L. The cross-product photocurrent then becomes

$$g_{3i}(t) = 2\,\mathrm{Re}\left\{\int_{-\frac{W}{2}}^{\frac{W}{2}} f'(u,t)r'(u)du\right\}. \tag{3.49}$$

We therefore discover that the cross-product photocurrent represented by equation (3.49) is equal to equation (3.48), which is equal, in turn to equation (3.35), where equation (3.35) represents the photocurrent when all the light is collected in the Fourier plane using an area photodetector. We

have therefore shown that the cross-product photocurrents are equal whether we use a point photodetector in the image plane or an area photodetector in the Fourier plane. There is no fundamental difference, as far as the cross-product term is concerned, between Fourier plane detection and image plane detection, provided that all the overlapping and colinear light is collected. However, since we clearly do not collect all the signal beam energy when point detection is used, what affect does this have on the system performance?

The signal bias term, when detected with a finite width photodetector L is given by

$$g_{1i}(t)=\int_{-\frac{L}{2}}^{\frac{L}{2}}\left[2\,\mathrm{Re}\left\{\int_{-\infty}^{\infty}F(\alpha,t)H(\alpha)e^{j2\pi\alpha u}d\alpha\int_{-\infty}^{\infty}F^{*}(\gamma,t)H^{*}(\gamma)e^{-j2\pi\gamma u}d\gamma\right\}\right]du. \tag{3.50}$$

We represent the first Fourier integral as f'(u,t) and the second as its complex conjugate. Therefore, the signal bias term photocurrent becomes

$$g_{3i}(t)=\int_{-\frac{L}{2}}^{\frac{L}{2}}\left|f'(u,t)\right|^{2}du. \tag{3.51}$$

We now let the photodetector size shrink to W so that it is just large enough to collect all the reference beam. Equation (3.51) is therefore represented as

$$g_{1i}(t)=\int_{-\frac{L}{2}}^{\frac{L}{2}}\left|f'(u,t)\right|^{2}\mathrm{rect}\left[\tfrac{u}{W}\right]du. \tag{3.52}$$

Since the photodetector is smaller than the extent of the signal beam we get

$$g_{1i}(t)=\int_{-\frac{W}{2}}^{\frac{W}{2}}\left|f'(u,t)\right|^{2}du. \tag{3.53}$$

Since we are integrating over a small portion of the signal beam, we find that

$$\int_{-\frac{W}{2}}^{\frac{W}{2}}\left|f'(u,t)\right|^{2}du<\int_{-\frac{L}{2}}^{\frac{L}{2}}\left|f'(u,t)\right|^{2}du \tag{3.54}$$

where we assumed that W<<L. We therefore observe that the signal beam bias term is reduced when a point photodetector is used in the image plane to detect the light. As a consequence, collecting a small portion of the signal beam reduces the shot-noise of the optical system, therefore improving the signal-to-noise ratio, as we show in the next section.

Following a similar argument as presented above, and recalling that the point photodetector is large enough to collect all the reference beam, we find that the reference beam bias term is

$$g_{2i}(t)=\int_{-\frac{L}{2}}^{\frac{L}{2}}\left|r'(u,t)\right|^{2}du=\int_{-\frac{W}{2}}^{\frac{W}{2}}\left|r'(u,t)\right|^{2}du. \tag{3.55}$$

Since all the reference beam is collected in both the Fourier plane using an area photodetector and the image plane using a point photodetector, we find that the reference beam bias terms are equal under the two measurement conditions.

3.5 The effect of the detection schemes on the signal-to-noise ratio

The signal-to-noise ratio at the photodetector output is given by

$$SNR = \frac{\langle i_s^2 \rangle R_L}{2eB(i_d + i_{sa})R_L + 4kTB}, \tag{3.56}$$

where i_s is the signal current, e is the charge on an electron, B is the post-detection bandwidth, i_d is the dark current, i_{sa} is the average signal current, k is Boltzmann's constant, T is the temperature in degrees Kelvin, and R_L is the photodetector resistance. The average signal current, i_{sa}, is proportional to the power of the reference beam plus the power of the signal beam plus the power of the cross-product term. Since the cross-product term is constant for these calculations, we examine just the contribution from the bias terms.

We present an example of the effect on the signal-noise ratio to facilitate our discussion of the two detection schemes. Figures 3.1 and 3.2 show an optical processor where the light is detected in the Fourier and image planes of the acousto-optic cell, respectively. We assume the beamsplitters are 50/50 power splitters and that the laser has an output power of 10 mW. In the Fourier plane all the reference and signal beams are collected by an area detector. For 200 simultaneous cw inputs to the acousto-optic cell with a diffraction ratio of one microwatt of optical power per frequency, we get 200 microwatts of signal power at the Fourier plane; these optical power values are from measurements made on the Presort Processor. We have a total reference beam power of 2.5 mW in the Fourier plane. The total power incident on the area photodetector in the Fourier plane is therefore 2.5 mW + 0.2 mW = 2.70 mW.

At the image plane we collect the reference beam plus a portion of the signal beam; we assume that the photodetector is 1/200 the size of the signal beam. The total power incident on the point detector is then

$$2.50 \text{ mW} + 200\text{uW}/200 = 2.501 \text{ mW}.$$

We now calculate the percentage power, relative to the area photodetector power, that is incident upon the point photodetector. The percentage power is

$$\frac{2.501}{2.700} \times 100 = 92.6\%, \tag{3.57}$$

implying that point detection does not have a significant advantage over Fourier plane detection in terms of shot noise reduction. We note that the type of detection scheme used is dependent on the type of signals that are to be processed. We further note that using point detection over area detection would be advantageous when the system is shot-noise limited and the signal and reference beams are the same strength at the photodetector. Finally, point detection is better because its capacitance is smaller than the capacitance for area detectors, and it can therefore be used for wider bandwidth signals.

3.6 Discussion and conclusions

Figure 3.7 shows an envelope of a cw signal, at the image plane, when the mainlobe of the cw interferer is excised in the frequency plane. The small sinc function in the middle of the graph is the image plane representation of the reference beam; the reference beam and the signal beam have an amplitude of one. Recall that the cross-product photocurrent, $g_{3i}(t)$, is proportional to the integral of the reference beam multiplied by the signal beam. The reference beam is positioned on the optical axis (i.e., x_0=0). If we were to slide the reference beam to the left, across the image plane, we observe that the reference beam multiplied by the signal beam decreases until a minimum value is reached at the zero point; the minimum value implies that the notch depth is a maximum. If we normalize the image plane to a length of one with the outer limits being 0.50 and -0.50, the zero-crossing occurs at plus or minus 0.215 from the optical axis. This result agrees with Erickson's work [1], in which he showed that, for the special case of rectangular apodization with three-fourths of the mainlobe excised, a deep, narrow notch occurs at 0.17. Since the entire mainlobe is excised in our example, the distance of the zero-crossings from the optical axis are increased. By using this image plane representation we therefore gain some insight into the relationship between the notch depth and the reference beam position.

Figure 3.8 shows the image plane when the mainlobe and neighboring sidelobes are excised; plot #1 is when the mainlobe is excised, plot #2 is when the mainlobe and the nearest sidelobes are excised, and plot #3 shows when the mainlobe and the nearest two sidelobes are excised. We observe that the photocurrent decreases as successive sidelobes are excised if the reference beam is on the optical axis. We further note that there are a variety of zero-points for the reference beam to dwell as more sidelobes are excised.

We now explore the performance of an optical excisor, namely the Presort Processor, which uses frequency plane notch filtering to excise narrowband interference from wideband signals. We then design and test a system that modifies the Presort Processor so that the frequency excision is open-loop adaptive.

4. Presort Processor modification

In this chapter we discuss the operation of the Presort Processor in detail; this includes the characteristics of the signal acousto-optic cell, the spatial light modulators, and a description of the frequency excision technique used. We describe how we modified the Presort Processor for this study; an analysis is given of the effect, on the Presort Processor, of inserting an optical window in the interferometer to split the signal beam. We describe the operation of the post-processing electronics which are used to determine the location of the narrowband interferers.

4.1 Description of the Presort Processor

The Presort Processor is an optical signal processor, developed by the Harris Corporation, to excise narrowband interference from wideband signals; the description of the Presort Processor in Sections 4.1 through 4.12 is based upon information obtained from the Final Report [15]. Figure 4.1 shows the basic components of the Presort Processor. The solid state laser has a wavelength of 830 nm, with a maximum power output of 40 mW. The laser includes collimating optics which, together with lenses L_1 and L_2, expand the beam to a 4 mm length in the direction parallel to the page. The beam is 250 μm wide in the direction perpendicular to the page.

The Presort Processor is based on a Mach-Zehnder interferometer with an acousto-optic cell and a prism in the lower branch of the interferometer. and with a lens in the upper branch. The prism expands the light in the direction of acoustic propagation from a 4 mm beam to an 8 mm beam to illuminate the acousto-optic cell. The acousto-optic cell receives the electrical signal, f(t), which is distorted by narrowband interferers, and modulates the light in both space and time.

The light in the upper branch of the interferometer passes through lens L_3 to create a point source, 12 μm in size, which is located exactly the same distance from the beam combiner as is the acousto-optic cell. The point source acts as a probe on the acousto-optic cell, causing the wideband photodetector to detect that part of the signal in the acousto-optic cell which overlaps the point source. To further explain this operation, we approximate the point source as a delta

function. At the photodetector, which is in an image plane of the acousto-optic cell, we have the convolution of the signal with a delta function, which recovers the signal, as we discussed in Section 3.2.1.

Since both segments after the second beamsplitter operate identically, we describe just the straight segment in detail. Spherical lenses L_4 and L_6 display the Fourier transform of the signal f(t) at the plane of the spatial light modulator. The spatial light modulator is used to block or pass various parts of the spectrum of the signal. The spatial light modulators used in this system have a 50 percent duty cycle, resulting in half the spectrum being covered by SLM1 in the straight segment, while the other half of the spectrum is covered by SLM2 in the folded segment. Cylindrical lens L_5 increases the waist of the beam from 250 μm, at the acousto-optic cell, to 400 μm at the spatial light modulator. After the beam passes through the spatial light modulator it is collected by spherical lens L_7, which focuses the light onto a wideband photodetector. The photodetector output from the straight segment is then added to the photodetector output of the folded segment, so that, in effect, the two spatial light modulators cover the entire bandwidth.

4.1.1 TeO_2 longitudinal phased array acousto-optic cell

The signal acousto-optic cell in the lower branch of the interferometer is a TeO_2 longitudinal mode, phased array device. Figure 4.2 shows the passband characteristics of the 200 MHz bandwidth cell; the bandwidth of the cell ranges from 250 MHz to 450 MHz. The time-bandwidth product of the cell, given that the length of the cell is 8 mm, that the acoustic velocity of the cell is 4200 m/s, and that the bandwidth is 200 MHz, is 340. The cell is illuminated by a Gaussian distribution which reduces the number of resolvable frequencies by a factor of approximately 1.5 because the Fourier transform of a truncated Gaussian illumination has a wider mainlobe than that for uniform illumination. The number of resolvable frequencies is therefore 200, which is equal to the number of spatial light modulator elements.

4.1.2 Spatial light modulators

Figure 4.3 shows the spatial light modulators, which consist of two 100-channel TeO_2 longitudinal mode, acousto-optic cells. The transducers for each cell are on center-to-center spacings of 250 μm, with transducer widths of 125 μm, and a cell height of 10 mm. These spatial light modulators have a 50 percent duty cycle resulting in both segments of the Presort Processor being dedicated to the frequency excision. The spatial light modulator resolution in the frequency plane is equal to the width of one transducer, which is d_0=125μm. Figure 4.3 shows how the multi-channel acousto-optic cells are interleaved so that one spatial light modulator covers the odd frequency bins and the other covers the even frequency bins. If we were to slide the spatial light modulators vertically along the dashed lines until they overlap, every frequency bin between 250 MHz and 449 MHz, with a resolution of 1 MHz, is represented by a spatial light modulator element. If a narrowband interferer is present, the appropriate acousto-optic channels are turned off, and the light which corresponds to that interferer is no longer incident on the photodetectors.

Figure 4.4 shows the theoretical notch shape provided by the spatial light modulators to notch a narrowband interferer; directly below the graph are the locations of the spatial light modulator elements. Curves one and two show the notch shape with one and two spatial light modulator elements switched, respectively. Notice that switching three consecutive spatial light modulator elements gives an excision depth of 25 dB, while switching five elements provides a notch depth of 28 to 33 dB.

We use an example to illustrate some of the characteristics of the spatial light modulators. We assume that a 25 dB, referenced to the noise level, 1 MHz bandwidth, narrowband interferer is distorting a spectrum. To excise the 25 dB narrowband interferer we need to switch at least three spatial light modulator elements as Figure 4.4 shows; if a N MHz wide notch is desired, N+1 spatial light modulator elements must be switched. Figure 4.4 shows that switching two spatial light modulator elements results in a 22 dB notch and is therefore not sufficient to perform the

excision. Therefore to excise a 25 dB interferer, at least three spatial light modulator elements must be switched.

4.2 Modification of the Presort Processor

The Presort Processor currently has a panel of 200 switches to control the spatial light modulators. We are implementing a power spectrum analyzer, along with post-detection electronics, to provide the control signals needed to adaptively switch the spatial light modulator elements. Figure 4.5 shows how the Presort Processor is modified to split the signal beam to implement a power spectrum analyzer. The amplitude of the signal beam is divided by an optical window, which is inserted at a twenty degree angle after the acousto-optic cell, to reflect 4 percent, while transmitting 96 percent, of the light. The reflected signal beam is then Fourier transformed in the direction of propagation of the acousto-optic cell, and is imaged in the perpendicular direction by lenses L_{12}, L_{13}, and L_{14}. The spectrum is incident on a CCD photodetector array, and sequentially clocked into the post-detection electronics. The description of the operation of the post-detection electronics is deferred until Section 4.5.1.

When we split the signal beam with the optical window, the beam passing through the optical window is displaced in the direction of propagation of the acousto-optic cell. Furthermore, the second surface reflection from the optical window produces a ghost beam parallel to the first surface reflection, which causes a fringe pattern to occur on the spectrum. Finally, the wedge on the optical window, caused by the nonparallel surfaces of the optical window, causes the spectrum of the signal to shift at the spatial light modulators. These effects are explored in the following sections.

4.2.1 Calculation of the required clear aperture

In this section we calculate the window clear aperture needed, based on the length of the optical beam after the acousto-optic cell. The illuminated part of the acousto-optic cell has a length of 8 mm, and the beam is diffracted by the acousto-optic cell at a maximum angle of θ_1=0.0198

radians with respect to the center frequency (350 MHz). Figure 4.6 shows how the optical window is inserted at a 20 degree angle with respect to the optical axis. The required height of the beam at the optical window, which is approximately 100 mm from the acousto-optic cell, is the sum of the apertures needed to collect the diffracted and undiffracted light:

$$h_0=2(100\text{ mm})(0.0198\text{ radians})+8\text{ mm}=11.95\text{ mm}.$$

Hence, the clear aperture needed for this configuration is

$$CA=\frac{11.95\text{mm}}{\sin(90-20)^{\circ}}=12.72\text{mm}. \tag{4.1}$$

The clear aperture for an optical window of length 30 mm, when inserted at a 20 degree angle, is 21.75 mm. Since the clear aperture of the optical window is larger than the height of the optical beam, a 30 mm diameter optical window is sufficient.

4.2.2 Displacement of the second surface reflected wave

Figure 4.6 shows the angle of incidence θ_1, which is twenty degrees, on the optical window. We know from Snell's law that

$$n_1\sin\theta_1=n_2\sin\theta_2, \tag{4.2}$$

where n_1 and n_2 are the indices of refraction of the first medium and second medium, respectively, and θ_1 and θ_2 are the angle of incidence and the angle the transmitted ray makes with respect to the normal, respectively. In our case n_1 is equal to one, and n_2 is equal to the index of refraction of the fused silica, which is 1.45.

We first solve for θ_2 in equation (4.2) to get

$$\theta_2=\sin^{-1}\left(\frac{n_1}{n_2}\sin\theta_1\right) \tag{4.3}$$

Since the thickness of the optical window is equal to t, the component parallel to the optical window that the beam travels is

$$x_1=t\tan\theta_2. \tag{4.4}$$

At the second surface, part of the light is transmitted, part of the light is reflected, and the remaining light is absorbed by the optical coating. From the law of reflection, we know that the angle of incidence is equal to the angle of reflectance, therefore, the total distance the beam travels

along the optical window is equal to $2x_1$.

The reflected beam from the back surface now escapes from the optical window and makes a 20 degree angle with respect to the normal of the front surface. Hence, the ray reflected from the first surface is parallel to the ray which escapes from the optical window from the second surface reflection; for now we are assuming the two surfaces of the optical window are parallel. Therefore, the angle the beam makes with the optical window is 70 degrees, and the total displacement of the beam, x_3, can be calculated by noting that

$$x_3 = x_2 \cos\theta_1. \tag{4.5}$$

We substitute equations (4.3) and (4.4) into equation (4.5) to get

$$x_3 = 2t\tan\left[\sin^{-1}\left(\frac{n_1}{n_2}\sin\theta_1\right)\right]\cos\theta_1, \tag{4.6}$$

where the total displacement is in terms of the input angle, the thickness of the optical window, and the indices of refraction. Since the optical window is 6 mm thick, we substitute the parameters into equation (4.6) and find that the total displacement is x_3=2.74 mm.

We now find the total displacement of the transmitted beam, and we denote this quantity as x_5. We see that the optical path the beam traverses through the material is

$$x_4 = \frac{t}{\cos\theta_2}. \tag{4.7}$$

Furthermore, we recognize that the displacement of the transmitted beam is

$$x_5 = x_4 \sin(\theta_1 - \theta_2). \tag{4.8}$$

We substitute equations (4.2) and (4.7) into equation (4.8) and we get

$$x_5 = \frac{t}{\cos\left[\sin^{-1}\left(\frac{n_1}{n_2}\sin\theta_1\right)\right]}\sin\left[\theta_1 - \sin^{-1}\left(\frac{n_1}{n_2}\sin\theta_1\right)\right]. \tag{4.9}$$

We substitute the values of the parameters into equation (4.9) to find that x_5=0.684 mm.

In summary, we find that the second surface reflected wave is displaced by 2.74 mm with respect to the first surface reflected wave, and that the transmitted beam is displaced by 0.684 mm with respect to the incident beam on the optical window. We now explore the effect these displacements have on the power spectrum at the CCD photodetector array.

4.2.3 Analysis of the second surface reflection

We now model the first and second surface reflections of the optical window. We let the beams of light reflected by the optical window be represented by g(x). Therefore, the reflected light, g(x), is represented by

$$g(x) = g_1(x) + g_2(x), \tag{4.10}$$

where $g_1(x)$ and $g_2(x)$ are the first and second surface reflections, respectively. The second surface reflection has the same content as the first surface reflection but is physically displaced, has an angular shift, and is attenuated with respect to the first surface reflection. The second surface reflection can therefore be represented as a function of the first surface reflection:

$$g_2(x) = bg_1(x - x_3)e^{j2\pi\alpha_6 x}, \tag{4.11}$$

where b is the attenuation constant, x_3 is the physical displacement, and α_6 equals θ_6/λ. We substitute equation (4.11) into equation (4.10) to get

$$g(x) = g_1(x) + bg_1(x - x_3)e^{j2\pi\alpha_6 x}. \tag{4.12}$$

The function g(x) now passes through a series of lenses which perform the Fourier transform. The Fourier transform of g(x) is

$$G(\alpha) = G_1(\alpha) + bG_1(\alpha - \alpha_6)e^{j2\pi\alpha x_3}, \tag{4.13}$$

where the exponential term is caused by the physical displacement of the two reflected beams.

The incident light falls on a photodetector array, which detects the intensity of $G(\alpha)$:

$$I(\alpha) = |G_1(\alpha)|^2 + b^2|G_1(\alpha - \alpha_6)|^2 + 2\mathrm{Re}\{G_1(\alpha)bG_1^*(\alpha - \alpha_6)e^{j2\pi\alpha x_3}\}. \tag{4.14}$$

The desired spectrum is $G_1(\alpha)G_1^*(\alpha)$, while the other two terms are unwanted.

First we analyze the effect of the physical shift, $\xi_1 = \lambda\alpha_1 F$, of the ghost Fourier transform which is caused by the second surface reflection. We calculate the angular deviation from the specifications given in the Melles Griot catalog. The 02 WLQ 306 optical window has a parallelism of five arcseconds; five arcseconds equals 5/3600 degrees or $2.42(10)^{-5}$ radians. Since the second surface reflection occurs on a tilted surface, the angular shift with respect to the first surface reflection is twice the angular error of the two surfaces, so that the total angular shift in radians is

$$\theta_6 = 2(2.42)(10)^{-5} = 4.85(10)^{-5}\text{radians}.$$

We now determine the effect of θ_6 in the Fourier plane using the transformation

$$\xi_6 = \alpha_6 \lambda F = \frac{\theta_6}{\lambda}\lambda F = \theta_6 F = 4.8482(10)^{-5}(263.1\text{mm}) = 12.76\mu\text{m},$$

where the focal length F=263.1 is calculated in Section 4.5. The angular tilt gives a physical shift of 12.76 μm which is approximately the size of a CCD photodetector element (13 μm) or one-fourth of a frequency resolution element.

The effect of the physical displacement of the two reflected beams is now analyzed. Since the shift is approximately one-fourth of the frequency resolution size, we let

$$G_1(\alpha - \alpha_6) \approx G_1(\alpha) \tag{4.15}$$

which simplifies the analysis. We use this approximation in equation (4.14) to get

$$I(\alpha) = |G_1(\alpha)|^2 + b^2|G_1(\alpha)|^2 + 2\text{Re}\{G_1(\alpha)bG_1^*(\alpha)e^{j2\pi\alpha x_3}\}. \tag{4.16}$$

We now take the real part of the last term of equation (4.16) and combine like terms to get

$$I(\alpha) = |G_1(\alpha)|^2\left[1 + b^2 + 2b\cos(2\pi\alpha x_3)\right]. \tag{4.17}$$

The first term in the brackets of equation (4.17) is the desired term. The second and third terms are undesirable, since the second term is caused by the second surface reflection, which also sets up the third term. The magnitude of b determines if the third term is of major concern. If b, which is the normalized second surface reflection, is equal to one, the spectrum of the signal is significantly distorted, since the term inside the brackets is zero when the cosine argument equals 180 degrees.

If the fringe pattern is not resolvable by the photodetector array the third term in equation (4.17) does not affect the output. From Section 4.2.2 we calculated x_3 to be equal to 2.74 mm. The frequency of the fringe pattern is therefore

$$\alpha_f = \frac{x_3}{\lambda F} = \frac{2.74\text{mm}}{(830\text{nm})(263.1\text{mm})} = 12.5\text{Ab}.$$

Since the length of the 800 photodetector elements is 10.4 mm, one cycle of the fringe pattern spans 6.2 photodetector elements, and the photodetector array easily resolves the fringe pattern.

If the optical window is placed in the interferometer without an anti-reflection coating on the second surface, the reflection is large compared to the first surface reflection. We coated the second surface with Hebbar /076 which gives a reflectance of less than 0.4 percent for light whose incident angle ranges from zero to thirty degrees. The 830 nm solid state laser is polarized with the

electric field perpendicular to the acoustic propagation of the acousto-optic cell, hence, in the classical sense, the polarization is parallel to the boundary of the window. To calculate the amount of light reflected by the optical window we use the Fresnel reflection coefficient [16]

$$r_p = \frac{n_1 \cos\theta_1 - n_2 \cos\theta_2}{n_1 \cos\theta_1 + n_2 \cos\theta_2}, \tag{4.18}$$

where n_1 and n_2 are the indices of refraction of the first medium and second medium, respectively, and θ_1 and θ_2 are the angle of incidence and the angle the transmitted ray makes with respect to the normal, respectively. In our case $\theta_1 = 20$ degrees, $\theta_2 = 13.64$ degrees, $n_1 = 1.0$, and $n_2=1.45$, so that

$$r_{p1}=0.20.$$

To calculate the power reflected, we square the reflection coefficient to get

$$R_1 = r_{p1}^2 = 0.040,$$

which is approximately 4 percent of the light at 20 degrees incidence. The power reflected by the second surface is

$$R_2 = r_{p2}^2 = (1-0.040)(0.004)(0.960) = 0.0037.$$

Therefore we have that $r_{p2}=0.061$, and we calculate b as

$$b = \frac{r_{p2}}{r_{p1}} = \frac{0.061}{0.200} = 0.305.$$

We return to equation (4.17), and substitute in the various parameters, to find that

$$I(\alpha) = 1 + 0.0930 + 2(0.305)\cos(2\pi\alpha x_3)$$

or

$$I(\alpha) = 1.0930 + 0.610\cos(2\pi\alpha x_3). \tag{4.19}$$

From equation (4.19) we find that the maximum value of the fringe pattern, relative to the mean, is $I(\alpha) = 1.7$ which is a 2.31 dB increase. The minimum value of the intensity pattern is 0.48 which is a -3.16 dB decrease from the mean. The fringe pattern therefore varies by 5.5 dB which shows that the response to a 30 dB narrowband interferer may range from 26.84 dB to 32.31 dB. This range is acceptable because we are considering the case where the interferer is 20 dB to 30 dB above the signal level, and we do not need fine amplitude resolution to discriminate between the signals.

We summarize this analysis by noting the presence of the ghost spectrum at the photodetector array distortion to the original spectrum. The amount of distortion is dependent on

the strength of the ghost spectrum, and on the physical displacement of the ghost spectrum with respect to the desired spectrum. Since the ghost spectrum is displaced by one-fourth of a resolution element and the second surface reflection is attenuated by 10.3 dB with respect to the first surface reflection, the amount of distortion is small. The fringe pattern on the spectrum will cause some of the narrowband interferers to appear stronger or weaker, however, since the second surface is anti-reflection coated, this effect is small.

4.2.4 Effect of the wedge of the optical window at the spatial light modulators

In this section we explore the effect of the wedge on the optical window on the Fourier planes at the spatial light modulators. Recall that the optical window chosen for this experiment has a parallelism of

$$\phi = 2.42(10)^{-5} rad.$$

How much does this angular tilt affect the Fourier plane? We know that $\theta=\lambda\alpha$ so that

$$\xi = \alpha\lambda F = \theta F. \tag{4.19}$$

Hence, the amount of displacement in the Fourier plane is

$$\Delta\xi = (634mm)(2.42)(10)^{-5} = 15.34um.$$

Since the spatial resolution size in the Fourier plane is 125 μm, the spectrum is shifted by about 1/8 of a resolution element. The shift can be easily corrected in the Presort Processor by moving the spatial light modulators as part of the calibration procedure.

4.2.5 Analysis of a shifted signal

In this section, we examine the effects of the shift, x_5, produced by inserting an optical window at an angle with respect to the optical axis after the acousto-optic cell. The light distribution, immediately after the acousto-optic cell, is represented by

$$f_+(x,t) = jma(x)s\left(t-\frac{T}{2}-\frac{x}{v}\right)e^{j2\pi f_c\left(t-\frac{T}{2}-\frac{x}{v}\right)}e^{j2\pi\alpha_b x}, \tag{4.20}$$

where m is the modulation index, a(x) is the aperture function, and α_b equals θ_b/λ, where θ_b is the illumination angle on the acousto-optic cell. This light distribution passes through the optical window, which translates it in the direction of propagation, or the positive x-direction, of the

acousto-optic cell. The shifted signal light distribution is given by

$$f_+(x,t) = jma(x-x_5)s\left(t-\frac{T}{2}-\frac{(x-x_5)}{v}\right)e^{j2\pi f_c\left(t-\frac{T}{2}-\frac{(x-x_5)}{v}\right)}e^{j2\pi a_b(x-x_5)}. \tag{4.21}$$

We now turn our attention to the reference beam, which is a function of x only. The lens creates an effective point source a distance x_0 from the optical axis, the reference beam is therefore represented by

$$r(x) = \mathrm{sinc}\left[\frac{x-x_0}{d_0}\right], \tag{4.22}$$

where d_0 is the size of the point source. The reference beam and the signal beam combine at the beam combiner, and are imaged onto two wideband photodetectors.

Since the photodetectors are in an image plane of the acousto-optic cell, the signal beam and the reference beam are represented by reversed coordinates. We let u be the coordinate at the photodetectors. The signal light distribution at the photodetectors is represented by

$$f_+(u,t) = jma(-u-x_5)s\left(t-\frac{T}{2}-\frac{(-u-x_5)}{v}\right)e^{j2\pi f_c\left(t-\frac{T}{2}-\frac{(-u-x_5)}{v}\right)}e^{j2\pi a_b(-u-x_5)}. \tag{4.23}$$

Similarly, the reference beam at the photodetectors is represented by

$$r(u) = \mathrm{sinc}\left[\frac{(-u-x_0)}{d_0}\right]. \tag{4.24}$$

The intensity of the combined beams is

$$I(u,t) = |f_+(u,t)|^2 + |r(u)|^2 + 2\,\mathrm{Re}\left\{f_+(u,t)r^*(u)\right\}, \tag{4.25}$$

where we are interested in only the cross-product term, since the others are removed by a bandpass filter. The photodetector integrates the light intensity over the output plane such that g(t) is given by

$$g(t) = \int_{-\infty}^{\infty} I(u,t)|P(u)|^2 du, \tag{4.26}$$

where P(u) is the photodetector aperture function. In this analysis, we assume that P(u) equals over the surface of the photodetector. The third element is the cross-product term, which is given by

$$g_3(t) = 2\,\mathrm{Re}\left\{\int_{-\infty}^{\infty} f_+(u,t)r^*(u)du\right\}. \tag{4.27}$$

We substitute equations (4.23) and (4.24) into (4.27) to get

$$g_3(t) = 2\mathrm{Re}\left\{\int_{-\infty}^{\infty} jma(-u-x_5)s\left(t-\frac{T}{2}-\frac{(-u-x_5)}{v}\right)e^{j2\pi f_c\left(t-\frac{T}{2}-\frac{(-u-x_5)}{v}\right)}e^{j2\pi u_b(-u-x_5)}\mathrm{sinc}\left[\frac{(-u-x_0)}{d_0}\right]du\right\}. \tag{4.28}$$

We take the temporal terms outside the integral and simplify $g_3(t)$ to get

$$g_3(t) = 2\mathrm{Re}\left\{jme^{j2\pi f_c\left(t-\frac{T}{2}\right)}\int_{-\infty}^{\infty} a(-u-x_5)s\left(t-\frac{T}{2}-\frac{(-u-x_5)}{v}\right)e^{j2\pi f_c\left(\frac{(-u-x_5)}{v}\right)}e^{-j2\pi u_b(-u-x_5)}\mathrm{sinc}\left[\frac{(-u-x_0)}{d_0}\right]du\right\}. \tag{4.29}$$

We approximate the sinc function as a delta function, as we did in Section 3.2.2, to get

$$g_3(t) = 2\mathrm{Re}\left\{jme^{j2\pi f_c\left(t-\frac{T}{2}\right)}\int_{-\infty}^{\infty} a(-u-x_5)s\left(t-\frac{T}{2}-\frac{(-u-x_5)}{v}\right)e^{j2\pi f_c\left(\frac{(-u-x_5)}{v}\right)}e^{-j2\pi u_b(-u-x_5)}\delta(-u-x_0)du\right\}. \tag{4.30}$$

We invoke the sifting property of the delta function to get

$$g_3(t) = ma(-x_0-x_5)s\left(t-\frac{T}{2}+\frac{(x_0+x_5)}{v}\right)\cos\left[2\pi f_c\left(t-\frac{T}{2}+\frac{(x_0+x_5)}{v}\right)+\frac{\pi}{2}\right]. \tag{4.31}$$

where we realize that the output of the photodetector is proportional to the input signal, as in Section 3.2.2, but with an added time delay of x_5/v. We note that the carrier is also shifted by a phase factor which is directly proportional to the amount of the physical shift, but this does not affect the recovery of the signal. Finally, a scaling factor is introduced because the aperture function is probed at a slightly different place then when the light distribution is unshifted, however, the difference in amplitude is minute and does not significantly affect the current output.

4.3 Measurements on the optical window

Before inserting the optical window into the Presort Processor, we evaluated the optical window's baseline performance. An 830 nm laser produces 10 mW of power incident on the optical window. The transmitted power is 94.6 percent or 9.46 mW of the incident light. The reflected power off the first surface (uncoated) is 390 μW, and the power reflected off the second surface (coated with Hebbar /076) is 16.6 μW. We calculate the percent of reflected light off the first surface as

$$\frac{0.390mW}{10mW}100 = 3.9\%.$$

Since we showed in Section 4.2.3 that the theoretical power reflected off the first surface is

4 percent, the measured value and the calculated value are in close agreement. The power reflected off the second surface is 0.166 percent of the incident power, which compares to a specification (from Melles Griot) value of 0.37 percent. If we add up the percentages calculated above, the total power reflected and transmitted is 98.77 percent. We attribute the 1.23 percent of light unaccounted for as the amount the optical coating absorbs.

Returning to Section 4.2.3, we compare the measured value of the fringe pattern to the theoretical value. The amount of light reflected off the first and second surfaces are 3.9 and 0.166 percent of the incident light, respectively. We calculate the first surface Fresnel reflection coefficient as

$$r_{p1} = \sqrt{0.039} = 0.1975.$$

Similarly, we compute the second surface reflection coefficient as

$$r_{p2} = \sqrt{0.00166} = 0.0407.$$

We calculate b as

$$b = \frac{r_{p2}}{r_{p1}} = \frac{0.0407}{0.01975} = 0.2061.$$

Hence, we now calculate the intensity in the Fourier plane as

$$I(\alpha) = 1 + b^2 + 2b\cos(2\pi\alpha x_3),$$

or, after substituting the value of b, we get

$$I(\alpha) = 1 + 0.0425 + 0.4122\cos(2\pi\alpha x_3).$$

Therefore a 30 dB narrowband interferer will range between 28 dB to 31.64 dB depending on the value of α; the difference between the experimental results and the calculated values is attributed to the anti-reflection coating value being a worst case specification. Hence, the amount of distortion is small and therefore tolerable for our application.

4.4 Insertion of the optical window into the Presort Processor

Figure 4.7 shows the amplitude and phase response of the Presort Processor before the optical window is inserted. The amplitude response is flat to within 3 dB, except for the six notches, denoted by the numbers one through six, in the passband. These notches are caused by six disfunctioning spatial light modulator elements; the elements, which have a one-to-one correspondence to frequencies in MHz, are 266, 308, 348, 355, 421, and 446. The bottom part of

the trace shows the phase response of the Presort Processor. Notice that there is 45 degrees of phase variation over the 200 MHz bandwidth.

We then inserted the optical window into the interferometer of the Presort Processor at approximately a twenty degree angle and the amplitude response remained unchanged. Figure 4.8a shows that the phase response of the Presort Processor is linear; note the sawtooth phase waveform is caused by the network analyzer having a modulo 2π scale. The linear phase, which corresponds to a time delay, is caused by the 0.558 mm shift of the optical beam in the direction of propagation of the acousto-optic cell.

We null out the linear phase by introducing an electrical time delay of 0.1328 μs; this time delay corresponds to a physical shift in the beam of 0.558 mm. Although the theoretical value calculated in Section 4.3.2, based on a nominal window angle of 20 degrees, is 0.684 mm, the experimental result given here implies that the window angle was actually inserted at an angle of 17 degrees.

Figure 4.8b shows the phase of the Presort Processor after the optical window is inserted and after the linear phase is nulled. Notice that the phase, when compared to the phase response in Figure 4.7, is quadratic. The change in the phase response is attributed to the path difference obtained when the optical window is placed at an angle in the interferometer of the Presort Processor. Recall that the focus of the lens in the upper branch should be an equal distance from the beam combiner as the signal acousto-optic cell. However, when the optical window is placed inside the interferometer at an angle, the path length in the lower branch increases by the cosecant of the angle the ray inside the material makes with respect to the normal. Therefore, the focal plane of the lens in the upper branch of the interferometer and the acousto-optic cell are no longer the same distance from the beam combiner. The lens in the upper branch can be moved closer to the first beamsplitter, to correct the path difference, thus increasing the distance from the focus to the beamcombiner. Other solutions are to place an optical window, with the same thickness and at the

same angle, in the upper-branch, or to move the acousto-optic cell closer to the beam combiner.

Figure 4.9a shows an expanded view of the amplitude response before the optical window is inserted in the interferometer of the Presort Processor. Notice that the notch is a fraction of a MHz to the right of 330 MHz. Figure 4.9b shows the amplitude response when the optical window is inserted. The notch has moved to the right of the vertical line by approximately one-sixth of a megahertz; the shift is caused by the wedge on the optical window. The physical shift of the spectrum does not affect the performance of the Presort Processor because the spatial light modulators are moved a corresponding amount, using their micrometer adjustments, to accommodate the shifted spectrum.

Figure 4.10 shows the phase response when a second optical window is positioned in the upper branch of the interferometer, at the same angle as the first optical window. Figure 4.10 shows that the phase response is similar to the phase response before the optical windows are inserted, as shown in Figure 7, therefore correcting the path length mismatch between the reference beam and the signal beam. The sudden jumps in phase are due to the fact that six of the spatial light modulator elements are not functioning, causing six notches in the spectrum. Since the noise floor is greater than the notched depth, the random phase jumps occur at the disfunctioning spatial light modulator element locations.

As a completion to this exercise, we modulated a pulse, passed it through the Presort Processor, demodulated the pulse, and displayed it on an oscilloscope. We performed this experiment before the primary optical window is inserted, after the primary optical window is inserted, and after the corrective optical window is inserted. Figure 4.11 shows the results of this experiment. The top trace is without the primary optical window, the second is with the primary optical window, and the third is after the corrective optical window is inserted.

Note that the rise-time and fall-time of the pulse increases, hence spreading the pulse, from the top trace to the middle trace. The spreading of the pulse is readily understood by considering

the path difference created by the optical window. Since the path length from the acousto-optic cell to the beam combiner is greater than the path length from the focus to the beam combiner, the focal plane of the lens in the upper branch is effectively outside the plane of the acousto-optic cell. The light goes through its focus and to a Fresnel plane, the function at the Fresnel plane can be thought of as a larger point source, but not a delta function, that probes the signal in the acousto-optic cell. We approximate the larger source as a rect function so that, at the photodetector plane, the convolution of the signal with the rect function causes the pulse to spread, as second trace shows. From the third trace, we notice that when the second optical window is inserted in the upper branch of the interferometer to bring the reference focal plane into coincidence with the acousto-optic cell, the rise-time and fall-time return to normal, and the passband of the pulse is restored to its original value.

4.5 Calculation of the Fourier lens focal length

First we calculate the length of the D series linear, 1024 element CCD photodetector array that is to be illuminated. We choose the Fourier transform to illuminate 800 photodetector elements, which are 13 micrometers wide, so that a frequency resolution element is sampled at a four-to-one ratio. Hence, the array length illuminated is

$$\Delta\xi=800(13\mu m)=10.4 \text{ mm}.$$

The spatial variable in the Fourier plane is related to the parameters of the signal and the acousto-optic cell by

$$\Delta\xi = \frac{\lambda\Delta f}{v}F, \tag{4.32}$$

where Δf is the bandwidth of the signal, λ is the wavelength of the light, v is the acoustic velocity within the cell, and F is the focal length of the Fourier lens. We have Δf=200 MHz, λ=830 nm, v=4200m/s, and $\Delta\xi$= 10.4 mm in this design. We rearrange equation (4.32) to calculate the required focal length of the lens as F=263.1 mm.

The beam height at the acousto-optic cell is 250 micrometers and the height of the elements on the photodetector array is 13 micrometers. Therefore, to collect all the light, a demagnification

on the order of 20 must be accomplished by using a cylindrical lens.

4.5.1 Fourier lens calculation

We first calculate the focal lengths of the lenses used for the Fourier transform, and we then calculate the focal length of the imaging lens. The closest focal length lens available off-the-self is 260 mm. To accurately illuminate the photodetector array, we must therefore use two lenses. The equivalent power of two lenses is

$$K_{eq} = K_1 + K_2 - d_{12}K_1K_2, \tag{4.33}$$

where K_1 and K_2 are the powers of the two lenses, and d_{12} is the distance between the lenses; the power of a lens is the reciprocal of its focal length. We use two available lenses whose focal lengths are F_1=350 mm and F_2=750 mm. To achieve an equivalent focal length of 263.1 mm, we calculate the distance between the lenses as d_{12}=101.9 mm.

Figure 4.12 shows the top view of the optical system. Using ray tracing techniques, h_3, the output height, is derived in terms of the input angle, the distances between the lenses, and the power of the lenses. The height, h_1, at the first lens is

$$h_1 = \theta_1 d_1, \tag{4.34}$$

where d_1 is the distance from the input plane to the lens, and θ_1 is the cutoff angle. We calculate the angle, θ_2, shown in Figure 4.12, using the refraction equation

$$\theta_2 = \theta_1 - h_1K_1, \tag{4.35}$$

where K_1 is the power of the first lens. We continue with the ray tracing technique to get the following equations:

$$h_2 = h_1 + \theta_2 d_2, \tag{4.36}$$

$$\theta_3 = \theta_2 - h_2K_2, \tag{4.37}$$

$$h_3 = h_2 + \theta_3 d_5, \tag{4.38}$$

where the various parameters are shown in Figure 4.12. We substitute equations (4.34) through (4.37) into (4.38) to get

$$h_3 = \theta_1\left(d_1 + d_2 + d_5 - d_1d_2K_1 - d_2d_5K_2 - d_1d_5K_{eq}\right), \tag{4.39}$$

Since d_2, θ_1, the height, h_3, in the output plane, and the power of the lenses are known, we can

express d_5 as a function d_1:

$$d_5 = \frac{h_3 - \theta_1(d_1 + d_2 - d_1 d_2 K_1)}{\theta_1(1 - d_2 K_2 - d_1 K_{eq})}. \tag{4.40}$$

Since we have the output distance as a function of input distance, we can design the optical system based on total length considerations.

4.5.2 Design and placement of the Fourier transform lenses

Figure 4.1 shows a top view of the interferometer of the Presort Processor. The distance from the acousto-optic cell to the optical window is 105 mm. We choose the distance from the acousto-optic cell to the first lens as 150 mm, which places the lens 45 millimeters outside of the interferometer. The lenses in the optical design are placed outside of the interferometer so they do not disturb the operation of the Presort Processor.

Using the relationship developed in the last section between the input and output distance, we calculate the distance, d_5, from the second Fourier transforming lens to the photodetector array. We have that h_3=5.2 mm, θ_1=0.01976 radians, d_1=150 mm, d_2=101.9 mm, F_1=350 mm, F_2=750 mm, and F_{eq}=263.1 mm. We substitute the parameters into equation (4.40) to get that d_5=187 mm. Therefore the total length of the optical system is $d_1+d_2+d_5$=439 mm.

4.5.3 Image direction calculations

Figure 4.13 shows the image direction of the optical system. Since the output spot size, the input spot size, the distances of the Fourier transform lenses, and the powers of the first two lenses are known, the unknown parameters in the system are the distances d_3, d_4, and F_3. We derive d_3 as a function of d_4, using ray tracing techniques, to get

$$d_3 = \frac{-\theta_4 d_4 - \theta_1(d_1 + d_2 - d_1 d_2 K_1)}{\theta_1(1 + d_1 K_{eq} - d_2 K_1)}, \tag{4.41}$$

where all the parameters except for d_3 and d_4 are known. We substitute in the values of the parameters to get

$$d_3 = 65.41 d_4 - 708.24. \tag{4.42}$$

From the Fourier transform design we know that

$$d_3 + d_4 = 187\text{mm}. \tag{4.43}$$

We solve equation (4.43) for d_4 and substitute its value into equation (4.42) to get

$$-d_4 + 187\text{mm} = 65.41 d_4 - 708.24. \tag{4.44}$$

We solve equation (4.44) to get that d_4=13.5 mm. We now substitute the value of d_4 into equation (4.43) to get that d_3=173.5 mm. From the transfer equation we have that

$$K_3 = \frac{\theta_3 - \theta_4}{h_3} = \frac{\theta_2 - h_2 K_2 - \theta_4}{-\theta_4 d_4}, \tag{4.45}$$

where all the parameters in the equation are known. We find that K_3=0.075317 mm, so that the focal length of F_3 is 13.27 mm. Melles Griot has a cylindrical lens with a focal length of 12.7 mm in stock, which gives sufficient light on the photodetector array for the integration time we are using. Summing up, we have F_3=12.7 mm, d_3=173.5 mm, and d_4=13.5 mm.

4.6 Introduction to the post-processing electronics

The major purpose of this study is to show that the switching of the spatial light modulator elements can be automated in an open-loop fashion. To achieve this goal we implemented an optical power spectrum analyzer to read out the power spectrum into post-processing electronics; the post-processing electronics were constructed using wire-wrapping techniques. The post-processing electronics locate the narrowband interferers in the spectrum, and output a location corresponding to the spatial light modulator element where the narrowband interferer occurs. A thresholding scheme is used to achieve this operation, along with a feedback loop, to adaptively set the threshold.

4.6.1 Description of the post-processing electronics

Figure 4.14 shows a block diagram of the post-processing electronics. The power spectrum of the signal is detected by the CCD photodetector array, and is sequentially clocked into the analog-to-digital converter, which converts the spectrum to a digital number stream. The digital numbers are compared to a threshold which is adaptively set by the post-processing electronics, or, alternately, the threshold can be set by the operator. If the digital number, which corresponds to the magnitude of the spectrum, is greater than the threshold, we decide that a narrowband interferer is present; conversely, if the digital number is less than the threshold, we decide that no interferer is

present. The location of the pixels in the photodetector array which exceed the threshold are counted and clocked into the excising routine. The excising routine, which uses a look-up table format, outputs the spatial light modulator element location information required to perform the switching.

4.6.2 Adaptation mode

In the adaptation mode of operation, the post-processing electronics dynamically adapts to a steady-state solution. Suppose that switches one and two of the block diagram shown in Figure 4.14 are closed, while switch three is open. In this mode of operation, the operator inputs the number of narrowband interferers to be excised, and the threshold search feedback loop sets a threshold level where the number of narrowband interferers input by the operator are excised. We use an example to illustrate the adaptation mode of operation.

Figure 4.15 shows a spectrum, distorted by six narrowband interferers. Suppose that the operator sets the number of narrowband interferers to be excised at four. The first time the spectrum is read out, the system automatically sets the threshold to the largest value. The threshold search depends on whether the number of narrowband interferers input by the operator exceeds, is less than, or is equal to the number of narrowband interferers that the threshold excises from the spectrum. Since none of the narrowband interferers exceed the threshold, none of the spatial light modulator elements are switched. The number of narrowband interferers exceeding the threshold, which is zero, is then compared to the number of interferers the operator wants to excise. Since this number is less than the number set by the operator, the search routine continues. The second time the array is clocked out, the post-processing electronics sets the threshold to the step below the initial value, where there are 16 equally spaced steps across the range of an eight-bit word. The number of narrowband interferers exceeding this threshold are counted, compared to the number of narrowband interferers the operator wants to excise and the appropriate spatial light modulator elements are switched to remove those narrowband interferers that exceed the threshold.

For each readout of the array, the number of narrowband interferers excised is compared to the number of narrowband interferers the operator desires excised, and sets a new threshold depending on whether the number of narrowband interferers excised is greater than, or less than the desired number. When the desired number of narrowband interferers excised is met, the threshold is stationary until a new value of narrowband interferers is input by the operator or until some narrowband interferers disappear or new ones appear in the spectrum.

4.6.3 *Operator interaction mode and visual display*

In the operator interaction mode, switches one and two are open while switch three is closed. The spectrum is sequentially clocked off the array, converted to digital numbers while the operator sets a threshold to which the values of the spectrum are compared. Figure 4.15 shows a spectrum of a signal that is distorted by six narrowband interferers. The operator reduces or increases the threshold depending upon how many of the six narrowband interferers he wants to excise. If he prefers to have only four excised, the position shown is correct. Since the operator monitors the spectrum and the threshold via the display in this mode of operation, the operator completes the feedback loop.

The visual display enhances the operation of the system by showing the power spectrum of the signal and the threshold level of the post-processing electronics. Figure 4.16 shows a spectrum on the oscilloscope display with an associated threshold. The spectrum of the signal is tapped directly off the CCD photodetector array and feeds channel one of the oscilloscope; the display is triggered from channel one. The threshold feeds channel two of the oscilloscope which appears as a horizontal line across the display. Every part of the spectrum appearing above the horizontal line is excised while the remaining spectrum is undisturbed, the lone interferer in Figure 4.18 is therefore excised.

4.6.4 Excising algorithm

The excising algorithm is a versatile part of the post-processing electronics. The operator

decides the expected type of spectral environment, and programs an algorithm that models the environment into the post-processing electronics. The excising algorithm uses the width of the interferer, which is counted by a threshold counter, together with the location of the interferer relative to the spatial light modulator elements to decide which spatial light modulator elements to switch. As an example, suppose an interferer is located in the center of the fourth spatial light modulator element and has a width of one spatial light modulator element. If the operator wants to switch only the spatial light modulator element on which the interferer occurs, the excising algorithm outputs the address which corresponds to spatial light modulator element number four. However, if the operator desires to switch the neighboring spatial light modulator elements, he can change the algorithm by reprogramming the post-processing electronics.

The CCD photodetector array samples the spatial light modulator elements at a ratio of four CCD photodetector elements per one frequency resolution element, equal to a spatial light modulator element width, so that the electronics can decide where the interferer is located relative to the spatial light modulator elements; the excising algorithm is stored in electrically programmable read-only-memories that are ultraviolet erasable. The excising algorithm, used for our experiments, searches for interferers that have a width of one frequency resolution element. If the interferer is located directly on a spatial light modulator element, that element is switched plus the neighboring elements; no more than three elements are ever switched for one interferer. If the interferer is principally located on two spatial light modulator elements, then both spatial light modulator elements are switched, plus the spatial light modulator element that is the nearest neighbor to the element on which the most energy of the interferer is incident. If the interferer is located directly between two spatial light modulator elements, they are switched, plus the spatial light modulator element that is the nearest neighbor to the lower number spatial light modulator element upon which the interferer is incident. The two primary spatial light modulator elements plus a nearest neighbor needed to be switched; the nearest neighbor could be the higher number or

the lower number spatial light modulator element. To verify the operation of the post-processing electronics a variety of interferer scenario's were implemented and the results are given in the Section 4.6.

4.7 Experimental results

Our primary design goal is to sort the spectrum of the signal, locate the narrowband interferers, and supply the spatial light modulator element addresses in less than 10 milliseconds. The post-processing electronics, which were wire-wrapped and delivered to RADC, sorts the entire spectrum, including the 224 CCD elements that are not illuminated, and outputs the spatial light modulator addresses for a particular scan time in 5.4 milliseconds; we therefore have met our primary design goal. Figure 4.17 shows the experimental setup used to test the electronics. The laser beam is expanded by lenses L_1 and L_2, and passes through a polarizer which is used to control the beam intensity. The beam is incident upon a phase-grating which produces several diffracted orders. The Fourier transform of the phase grating is formed by lens L_3 at the plane of the CCD photodetector array, resulting is numerous spots, which simulate narrowband interferers, along the length of the array. The addresses from the electronics are decoded and fed to a 10 element LED display, which are used to observe which spatial light modulators are switched.

We test the adaptation mode of operation by inputting the number of interferers to be excised, and showing that the post-processing electronics adapt to meet out specification. The first test consists of one interferer dominating the spectrum and we vary the number of interferers to be excised. We input zero interferers causing the threshold to remain at the maximum value. We increase the interferers desired excised to one and the threshold decreased to the steady-state value, as Figure 4.18 shows, therefore outputting the correct addresses. Since, the location of the interferer is known, we confirmed that the correct spatial light modulator elements are switched.

The second experiment is to have two interferers of different strengths while the number of interferers desired excised is varied. If we require that no interferer be excised, the threshold

remains at the maximum value. Figure 4.19 shows the result when we require that one interferer be excised; the electronics successfully finds the correct steady-state threshold. When we require that two interferers be excised, the threshold decreased until both interferers were successfully notched.

In dynamic environments, narrowband interferers are not necessarily stationary in amplitude or frequency, but are more likely to be agile interferers that hop through the spectrum according to a pseudo-random sequence. To simulate an interferer hopping through the spectrum, we varied the location of the interferers on the CCD array, and monitored the spatial light modulator elements that were switched. We changed the position of the interferer by sliding the CCD photodetector array horizontally while the electronics processed the new data. The electronics tracked the interferer to its new location and output the addresses to switch the correct spatial light modulator elements. We noticed that it took the post-processing electronics at most two scan times to successfully provide the address needed to notch the interferer.

Figure 4.20 shows the final interferer scenario used to test the electronics. There are four total interferers with two having equal amplitudes and the remaining two having different strengths. The purpose of this experiment is to show that a threshold can be set where we might only want to excise the three largest interferers. We manually varied the threshold until the position shown in Figure 4.20 was reached. The electronics output the correct addresses to successfully notch the three interferers, while leaving the smallest interferer untouched. We performed the same battery of tests as performed in the adaptation mode with the electronics in the operator interaction mode. In all cases, the addresses to the correct spatial light modulator elements were output. We have therefore completed the testing of the electronics, and now move ahead to the experimental results obtained on the Presort Processor.

5. Pulse experiments

In this chapter we explore the effect of removing frequency components of a pulse in the Presort Processor. We describe the results of computer simulations and experiments in which we remove spectral components of a pulse at an intermediate frequency, translate it to baseband, and characterize the distortion; these experiments utilize the multi-channel acousto-optic cells in the Presort Processor to perform the frequency removal. We study how this frequency removal relates to the final pulse shape at the photodetector, using the root mean square error as a measure of the distortion. Finally, we add a narrowband interferer to the pulse, excise it, and characterize the distortion after the pulse is translated back to baseband.

5.1 Signal excision

In the early 1980's Erickson [1-3] performed analyses and experiments dealing with signal excision. He used a Mach-Zehnder interferometer with an acousto-optic cell in one branch and beam shaping optics in the other branch to perform his experiments. His main interest was in finding the notch shape and depth in the frequency plane, using different reference beam shapes and a variety of illuminations on the acousto-optic cell.

Bandstetter and Grieve [7-8] built an optical notching filter that uses a recursive technique to obtain the final notch depth. They use a programmable spatial filter in which liquid crystal fingers block the undesired light. Their experiments involves passing an RF pulse through their optical excisor, and examining the effect their system has on the pulse. Narrowband interferers are then added to the RF pulse, excised using the recursive architecture, and then examined at the output at RF.

5.2 Computer simulation parameters and the experimental setup

In the computer simulation model that simulates the Presort Processor, we use a Gaussian distribution that is truncated at the $1/e^2$ points to illuminate the acousto-optic cell. The reference beam is represented as a Gaussian distribution, also truncated at the $1/e^2$ points, at the frequency

plane. We let the contrast ratio of the spatial light modulators be infinite, and assume that all signals are modulated to the center frequency of the signal acousto-optic cell.

In the first set of experiments we remove certain frequency components of the spectrum of a pulse at an intermediate frequency, and analyze the resulting distortion on the pulse after it is brought to a baseband frequency range. Figure 5.1 shows a block diagram of the experimental setup. The input baseband pulse is multiplied by a cw signal, translating the spectrum of the pulse to the intermediate frequency f_c. The drive signal to the acousto-optic cell is given as

$$f(t) = s(t) \cos(2\pi f_c t).$$

The Presort Processor modulates the light in both space and time, and Fourier transforms it at the frequency plane containing the spatial light modulators. Part of the spectrum is removed by the spatial light modulators and the remaining light is collected onto the photodetectors. The output of the Presort Processor is a pulse f_c, with part of its spectrum removed.

The signal from the photodetectors is then mixed with the same local oscillator at f_c, yielding a term at baseband and a term at twice the intermediate frequency. The double frequency term is rejected by a low-pass filter, and we denote the remaining distorted pulse by d(t). The distortion is measured relative to the output signal, b(t), which represents the signal when none of the spatial light modulators are switched.

Figure 5.2 shows a more complete block diagram of the experimental setup. The HP 8116A pulse/function generator produces a pulse which is fed into mixer 1. An intermediate frequency is generated by the HP 8640B signal generator, and is supplied to the power splitter. The number 2 output of the power splitter is connected into mixer 1 to translate the baseband pulse to the bandpass of the Presort Processor. The signal out of mixer 1 is then amplified by 30 dB, using a one watt Amplifier Research/Model 1W1000 amplifier. The amplified signal drives the acousto-optic cell in the Presort Processor.

The signal which is detected at the photodetectors is connected to mixer 2. Port 3 of the power splitter feeds the local oscillator to mixer 2. The output of mixer 2 is filtered by a 100 MHz

low-pass filter, and the baseband signal is displayed on a Tektronix 11403 Digitizing Oscilloscope.

5.3 Measure of distortion

There are various methods for measuring signal distortion. In the frequency domain, filters are characterized by parameters such as passband ripple, overshoot, and undershoot. Time domain distortion if often measured by parameters such as rise-time and fall-time. For our experiments we chose to use the root mean square error criterion as a measure of distortion. The root mean square value of a waveform, $v(t)$, is given by

$$RMS = \sqrt{\frac{1}{T}\int_0^T v^2(t)dt}, \tag{5.1}$$

where T is the duration of the waveform. From Section 5.2 we recall that the undistorted signal is denoted as b(t) and the distorted signal is given as d(t). Therefore, the error of the distorted pulse relative to the undistorted pulse is

$$e(t) = b(t)-d(t).$$

The root mean square error is given by

$$RMSE = \sqrt{\frac{1}{T}\int_0^T e^2(t)dt},$$

or

$$RMSE = \sqrt{\frac{1}{T}\int_0^T [b(t)-d(t)]^2 dt}. \tag{5.2}$$

In the following experiments, we normalize the root mean square error to the root mean square value of the undistorted pulse b(t).

5.3.1 System limitations due to the components

Several components in this experimental setup limit the performance of the system. For example, the local oscillator has a tendency to jump suddenly by one-half of a megahertz. The pulse generator produces pulse shapes that have large overshoot and slow fall times. The mixers limit the operation of the system because the local oscillator input has a low maximum input voltage. If the maximum input voltage level is exceeded, the mixer electronics are overdriven, causing spurs which are similar to narrowband interferers.

Figure 5.3 shows the cleanest signal obtainable from the experimental setup without overdriving the mixers; this pulse is what a receiver would see on a one-shot basis. The height of

the pulse is 7 millivolts with a noise level of 2 millivolts, which corresponds to a 10.9 dB signal-to-noise ratio. The Presort Processor has a signal-to-noise ratio of 25 dB, while the mixers have a signal-to-noise ratio that is much less than 25 dB, resulting in the mixers limiting the overall system performance. Triggering the oscilloscope to display the waveform was difficult due to the limitations of the test equipment. We therefore elected to overdrive the local oscillator input, yielding a larger signal level as well as a larger noise level at the output. We subsequently averaged the output signal 256 times to reduce the noise level. Since the averaging is equivalent to coherent detection, the signal-to-noise ratio attained in the following set of experiments is larger than the actual signal-to-noise ratio at the output of the system.

5.3.2 The removal of symmetric frequency components on a 78 ns pulse

In dynamic environments there are numerous emitters that may render a communication system useless. We want to excise these interferers, using frequency plane excision, to recover the intended message. When we excise the narrowband interferers, however, part of the energy of the intended message is also removed. In this experiment, we study the effects of removing symmetric frequency components of a 78 ns pulse at an intermediate frequency, and analyze the output pulse shapes at baseband. To further illustrate these experiments, we consider the sinc function in Figure 5.4a which represents the Fourier transform of a pulse. Figure 5.4b shows that the center value of the sinc function is removed and Figure 5.4c shows that symmetric frequency components are removed about the center value. The removal of symmetric frequency components of the sinc function is equivalent to notching a sinusoid whose frequency is equal to the frequency distance in Hertz from the center value of the sinc function, and an amplitude equal to the height of the sinc function at that particular distance.

Before we analyze the results of the computer simulation, let us first conjecture what we expect to obtain. Since the frequency components are removed symmetrically, we should expect the error to be largest in the middle of the band and roll off as we remove frequency components

further from the center frequency until we reach the first null; because the sinc function has 90 percent of its energy in the mainlobe and the amplitude of the sinc function rolls off to zero as we approach the first null. At the first null, the error should be a minimum and then oscillating in magnitude as we continue notching frequency components away from the null.

The spectrum of the pulse in the computer simulations is centered at 350 MHz with sidelobes as described in the previous section. First, we simulate the switching of the spatial light modulator element 350, which removes the central value of the sinc function. Although three spatial light modulator elements are switched to get a 25 dB notch in the Presort Processor, the notch positions are represented, in the following discussions, by the frequency of just the central spatial light modulator element. In subsequent experiments, we remove frequency components centered at 348 and 352, which removes symmetric frequency components of the pulse. The notches, which are equal to three spatial light modulator elements wide, are then incremented away from the center of the spectrum in steps of one spatial light modulator element. Therefore the next frequency components removed are centered at 347 as well as at 353.

Figure 5.5 shows the computer simulation results of the root mean square error as a function of spatial light modulator element position. The root mean square error begins at 0.50 and increases to 0.68 at 352 MHz. The increase in error is due to the removal of the central frequency components, which requires that only three spatial light modulator elements be switched off, while the removal of the first set of symmetric frequency components requires that six spatial light modulator elements be switched off. Since the symmetrical notches are near the highest amplitude of the spectrum, the root mean square error increases initially.

Since the mainlobe is 25.6 MHz wide, the sinc function reaches a minimum at 362.8 MHz; we therefore expect the root mean square error to be a minimum at 362 or 363 MHz. Figure 5.5 shows a minimum at 362 MHz with the value at 363 MHz being only slightly larger. Therefore, the computer simulation results agree with our expectations. We further expect the root mean

square error to follow the general shape of a sinc distribution, as shown in Figure 5.5, since we are removing the energy of the pulse symmetrically about the central value.

Figure 5.6 shows the experimental results of symmetrically removing frequency components of the spectrum of a 78 ns pulse; the graph shows the root mean square error as a function of spatial light modulator element position, which has a one-to-one mapping to frequencies in MHz. Note that the pulse is centered at 350 MHz in the computer simulations, but in our experiments the pulse is centered at 332 MHz. Since we are calculating the root mean square error relative to the undistorted pulse, as symmetric frequency components are removed, the results are the same since we remove the same frequency components in both the experimental and computer simulations. Therefore, to make the comparison between experimental and the computer simulations straightforward, we match the frequency scale of the experimental results to those of the simulation. The root mean square error, at the center frequency of 350 MHz, begins at 0.29 and increases to 0.37 at 352 MHz. The experimental root mean square error is smaller than the computer simulation results because infinite notch depths were used in the computer simulations. We expect the root mean square error to be minimized at 362 or 363 MHz. Since Figure 5.6 shows a minimum at 362 MHz, with the value at 363 MHz being only slightly larger, the experimental results agree with the computer simulation results.

We expect the root mean square error to increase as we symmetrically notch through the first sidelobe. This phenomena extends to 367 MHz, where it begins to decrease instead of increasing as we expect. The root mean square error does not increase because the output pulse displayed on the oscilloscope is unstable. The instability is caused by the temperature dependence of the system and by drifting of the local oscillator frequency. The oscillator frequency was readjusted at 367 MHz to obtain a good input pulse shape, and the renormalized data causes the results to be off by a gain factor. With this in mind, we recognize the root mean square error would trace out the first sidelobe and then produce a null at spatial light modulator element 374.

The root mean square error is a minimum at 374 MHz, and increases after that point. Another minimum should occur at 386 MHz, which is backed up experimentally by the minimum at 386 MHz in Figure 5.6.

Figure 5.7 shows the spectrum of the experimental pulse, after being passed through the system, but before being demodulated with the local oscillator. We observe that the mainlobe and the first two sidelobes of the sinc function are strong enough to recognize; however, we observe that the third sidelobe is close to the noise floor. The root mean square error after 386 MHz generally increases, without following the sidelobe pattern, since the energy level of the signal at the output is close to the noise floor.

Before we consider the experimentally obtained pulse shapes as a function of removing frequency components, we predict the effect on the pulse shapes. Fourier series analysis shows that all signals consists of weighted frequency harmonics. The frequency harmonics of an isolated pulse consists of a d.c. value, since the pulse is offset from the horizontal axis, plus a continuum of weighted harmonics. The fundamental harmonic is added to the d.c. value to get a pulse that is rounded, then successive harmonics are added to obtain the sharp transitions associated with the rise-time, the fall-time and the flatness on the top of the pulse. The d.c. value and the fundamental reside in the mainlobe of the sinc function, while the higher frequency components reside in the sidelobes of the sinc function. We therefore expect that the removal of the mainlobe frequency components will produce the most distortion on the pulse, and the removal of the higher frequency components will mostly affect the top of the pulse, the rise-time, and the fall-time.

We now consider the shape of the pulses as various frequency components are removed. Figure 5.8 shows the experimental reference pulse, while Figure 5.9 shows the experimental pulse after the three central spatial light modulator elements are switched. Notice that a d.c. value has been subtracted from the pulse, which is intuitively correct, since the d.c. value is located at 350 MHz. A comparison of the reference pulse with the distorted pulse reveals that the shape of

the pulse is preserved, but with a d.c. value subtracted.

We now examine the simulated pulse when elements 344 and 356 are switched and compare it to the experimental pulse when the same symmetric removal of frequency components is performed. Figures 5.10a and 5.10b, which are the simulated and experimental pulses, respectively, show that part of the fundamental is removed, as is evident by the sinking of the middle of the pulse. The simulated and experimental pulses have similar shapes, confirming that our computer model is correct.

When we remove the frequency components in the first sidelobe, the edges of the pulse become rounded, as Figures 5.11a and 5.11b show, because we are removing the higher frequency components. The fundamental is evident by the hump in the center of the pulse; this simulated pulse is with spatial light modulator elements 332 and 368 switched.

A similar effect happens as we remove frequency components in the second sidelobe and beyond. The edges on the pulse become rounded and ripple is evident on the top of the pulse due to the removal of the higher frequency components.

5.3.3 The removal of symmetric frequency components on a 468 ns pulse

The effects of excising narrowband interferers on the pulse shape is a function of the pulse duration. A given notch width represents removing a large fraction of the signal spectral components when the pulse is wide, because the spectrum of the pulse is narrow. To illustrate this effect, we repeated the frequency removal experiments using a 468 ns pulse as the input signal. Figure 5.12 shows the spectrum of a 468 ns pulse after it is mixed to baseband by the local oscillator. A long pulse in the time domain produces a larger signal-to-noise ratio in the frequency domain than a short pulse because the energy is spread over a smaller region. The nulls of the sinc function occur every 2.14 MHz. The spectral components of the pulse are removed in the same manner as for the 78 ns pulse, but in this case there are only two spatial light modulator elements per sidelobe and that the mainlobe spans only four spatial light modulator elements. Since 90

percent of the energy in a sinc function is in the mainlobe, the root mean square error should decline quickly.

Figure 5.13a and Figure 5.13b show the computer simulation and experimental results of the root mean square error as a function of spatial light modulator element position, respectively. The root mean square error is the largest when we switch spatial light modulator element 350. The large root mean square error is due to the concentration of energy near the center spatial light modulator element. By switching off three spatial light modulator elements we are eliminating over 50 percent of the mainlobe. We note that the shape of the root mean square error of the computer simulations are similar to the experimental results.

The first removal of symmetric frequency components, which corresponds to elements 348 and 352 being switched, is less traumatic on the pulse shape as confirmed by the decrease in the root mean square error. The decrease in the root mean square error is reasonable, since the notches are centered two spatial light modulator elements from the center of the spectrum, therefore not seriously affecting the energy in the mainlobe.

When we move the symmetric notches one more increment from the center of the spectrum, we notice that the root mean square error drops off significantly because the notches now are outside the mainlobe of the sinc function. The root mean square error does not follow the shape of a sinc function because the width of the spatial light modulator elements are large with respect to the distance to successive nulls on the sinc function.

Figure 5.14a and Figure 5.14b show the computer simulation and experimental results, respectively, of the pulse when we switch the three most centered spatial light modulator elements. Notice that we notched the d.c. component, plus a significant amount of the fundamental, resulting in a differentiation to occur on the pulse. Also note the similarity in the simulation results when compared to the experimental results; the small discrepancy of the two plots is caused by the removal of more than the mainlobe of the sinc function in the experimental results. The remaining

pulse shapes due to the excisions follow a pattern similar to those of the 78 ns pulse shapes discussed in Section 5.3.2.

5.4 Symmetric removal of the sidelobes of the sinc function

In another experiment, we symmetrically remove one of the sidelobes of the sinc function, and examine the effect of this frequency content removal on the shape of the pulse. We use a 100 ns pulse, as Figure 5.15 shows, for these experiments so that the sidelobes are 10 MHz wide, and the mainlobe is 20 MHz wide. After we have symmetrically removed the sidelobes, we perform another experiment where the mainlobe is removed. The final experiment, presented in this section, we remove all the sidelobes, with the mainlobe remaining intact, and examine the pulse shape.

Figure 5.16 shows the pulse after the second sidelobes are removed. Notice that there is a sinusoid on the passband of the pulse with two cycles across it. We therefore conclude that the second sidelobes provide significant energy to help flatten the pulse. This pattern continues, as successive sidelobes are removed, to generate a sinusoid with a number of cycles equal to the sidelobe number is present on the top of the pulse. For example, Figure 5.17 shows the pulse with the sixth sidelobes removed; six cycles appear across the top of the pulse.

Figure 5.18a shows that when we remove the mainlobe of the sinc function, the pulse is devoid of the d.c. value and of the fundamental. The remaining sidelobe spectral energy contains the higher frequency components, which produce the sharp rise-time and fall-time. Figure 5.18b shows the pulse with all the sidelobes of the sinc function removed, but with the mainlobe intact. We note the presence of the d.c. value plus the fundamental frequency, which contribute significantly to the pulse shape. Figure 5.19a and 5.19b show the computer simulation results when the mainlobe is removed and then all the sidelobes of the sinc function are removed, respectively. Notice the similarity in the pulse shapes when they are compared to Figure 5.18a and 5.18b. Therefore having the experimental results agree, in general, with the computer simulations.

5.5 How many sidelobes make a good pulse?

In this section we answer the question "How many sidelobes of the sinc function in the frequency plane is needed to represent a good pulse in the time domain?". In this experiment we use a 100 ns pulse and begin the experiment with the spatial light modulator elements switched so that seven symmetric sidelobes are present. Successive sidelobes are truncated, starting at the seventh sidelobe, and proceeding inward towards the center of the sinc function. Figure 5.20a and 5.20b show the computer simulation and experimentally obtained pulse when seven sidelobes are present in the frequency plane. From the data, we conclude that seven sidelobes clearly reconstructs the pulse.

Figure 5.21 shows the experimental pulse when five sidelobes are present in the frequency plane; note that there is an increase in the ripple from 7 sidelobes to 5 sidelobes. The rise-time and fall-time of the pulse is starting to increase due to the loss of the frequency components in the six and seventh sidelobes. We conclude that seven sidelobes is the minimum to cleanly reconstruct a pulse and, for some applications, six sidelobes can be used.

5.6 Introduction to narrowband interference experiments

Figure 5.22 shows the setup used to perform narrowband interference excision experiments. After the pulse is translated to f_c, a narrowband interference signal is added, the composite signal is passed through the Presort Processor and is demodulated after detection. We denote the narrowband interferer as j(t) and represent the signal fed into the Presort Processor as

$$f(t) = s(t) + j(t). \tag{5.3}$$

For these experiments the narrowband interference is a single frequency at the frequency f_j. Therefore, equation (5.3) becomes

$$f(t) = s(t)\cos(2\pi f_c t) + A_j\cos(2\pi f_j t), \tag{5.4}$$

where f(t) is the signal into the acousto-optic cell, the signal is Fourier transformed, the appropriate spatial light modulator elements are switched, and the output signal is translated to baseband to recover the signal s(t).

5.6.1 Excision of a narrowband interferer

In this section we present the results of adding a narrowband interferer to the signal, and performing the excision of the interferer to illustrate the operation of the Presort Processor. The power of the local oscillator is adjusted so that the acousto-optic cell is not overdriven. The reference pulse for the remainder of the experiments is shown in Figure 5.23; note that the pulse has a 5 mV peak and a width of 100 nanoseconds. Recall that the sidelobes are 10 MHz wide thus giving a mainlobe width of 20 MHz.

A narrowband interferer is introduced at 307 MHz, which is in the center of the second sidelobe of the pulse. Figure 5.24 shows the spectrum of the narrowband interferer plus the pulse at the intermediate frequency. Notice the narrowband interferer is 30 dB above the noise floor. Figure 5.25 shows the narrowband interferer plus the pulse waveform, showing that the pulse is completely obscured.

Figure 5.26 shows the pulse when spatial light modulator elements centered at 307 are switched to excise the narrowband interferer. The output pulse has the same shape as the reference pulse except for the rise-time overshoot, which is apparent in the reference pulse, that is partially removed when we excise the narrowband interferer. This result illustrates that the Presort Processor is capable of removing narrowband interferers, without seriously affecting the pulse shape.

5.6.2 Notching capability of the Presort Processor

In this experiment we explore the notching capability of the Presort Processor by locating the narrowband interferer between two spatial light modulator elements. We use the same strength narrowband interferer as in the first experiment, but we locate the narrowband interferer at 304.5 MHz. We then notch only two spatial light modulator elements at 304 and 305, with Figure 5.27 showing the output pulse shape. Note that the excision of the narrowband interferer is nearly complete, and a comparison with the reference pulse from Figure 5.23 reveals a good shape match.

The differences are the distortion caused by excising part of the spectrum of the pulse. We therefore conclude that if a narrowband interferer is centered between two spatial light modulator elements, only those two elements need be switched.

5.7 Root mean square error of pulse after a narrowband interferer is excised

Since 90 percent of the energy is in the mainlobe of a sinc function we are highly concerned with the resulting pulse shape when the narrowband interferer is inside the mainlobe of the sinc function. We use a 100 ns pulse which gives a 20 MHz wide mainlobe, centered at 331.7 MHz.

Figure 5.28 shows the spectrum of the pulse plus the narrowband interferer. Note that the narrowband interferer is roughly 30 dB above the noise level. Suppose that we move the narrowband interferer through the mainlobe from left to right, distorting the spectrum of the pulse as the interferer is excised.

Figure 5.29 shows the root mean square error as a function of the frequency of the interferer. The root mean square error is smallest at the edge of the mainlobe, which is intuitively correct since the mainlobe has a lower amplitude at the notch position.

As we increment the frequency of the narrowband interferer through the mainlobe we notice that the root mean square error increases until 332 MHz, which is approximately the center frequency of the pulse, and then decreases until the first null at 342 MHz. Since the excision of the pulses was thoroughly explored in earlier sections, we refer the reader to those sections to get a flavor of the pulse shapes with these frequency components excised.

As a final example, consider the case where the narrowband interferer is at 330 MHz. Since this frequency is close to the center frequency of the pulse, we should see a large amplitude 2 MHz beat frequency, if the interferer is not removed. Figure 5.30 shows the narrowband interferer obscuring the pulse waveform. Figure 5.31 shows the pulse when we form the appropriate notch at 330. This is an extremely pleasing and dynamic result. The pulse waveform is largely preserved, with some distortion caused by the removal of some frequency components.

6. Conclusions

Frequency plane excision is one method for removing narrowband interference from wideband signals. We showed that the Presort Processor, which utilizes frequency plane excision, can be modified so that the frequency excision can eventually be automated. The control signals to the spatial light modulators, which perform the notching of the interference, are updated every 5.4 milliseconds exceeding the design goal of 10 milliseconds. We showed both experimentally and theoretically that the proposed modification of the Presort Processor did not affect its performance.

We analyzed area detection in the Fourier plane versus point detection in the image plane and showed that the two detection schemes are essentially equal and produce notches of equal depth. We further showed that the point detection signal bias term is slightly less than the area detection signal bias term, thereby reducing the shot-noise. We also developed an image plane analysis technique that adds insight into the inter-relationship of the parameters used in frequency plane excision.

We tested the operation of the Presort Processor by removing various frequency components of a pulse and analyzing the resulting distortion at baseband. As expected, these experiments showed that the distortion is most severe when the removal is performed in the mainlobe of the sinc function. Further experiments added insight into the relationship between removing symmetric sidelobes in the frequency plane and the resulting distortion of the image plane pulse. We also added a narrowband interferer to the pulse, performed the excision using the Presort Processor, and analyzed the image plane pulse. These experiments showed, as expected, that the distortion on the pulse is small if the interferer is outside the mainlobe and is more pronounced if the interferer is inside the mainlobe of the sinc function.

Suggestions for future research include:

- increasing the speed of the post-processing electronics by using higher speed logic chips.
- performing multi-interference experiments where the interferers can be agile or stationary.

7. References

[1] Jerry Erickson, Linear Acousto-Optic Filtering with Heterodyne and Frequency-Plane Control, Ph.D. Thesis, Stanford University Electrical Engineering Department, June 1981.

[2] Jerry Erickson, "Optical excisor performance limits versus improved signal detection," SPIE, vol. 639, pp. 232-239, 1986.

[3] Jerry Erickson, "Linear acousto-optic filters for programmable and adaptive filtering," SPIE, vol. 341, pp. 173-180, 1982.

[4] John N. Lee, N. J. Berg, M. W. Casseday, and P. S. Brody, "High-Speed Adaptive Filtering and Reconstruction of Broad-Band Signals Using Acousto-Optic Techniques," 1980 Ultrasonics Symposium, pp. 488-492, 1980.

[5] Patrick J. Roth, "Optical excision in the frequency plane," SPIE, vol. 352, pp. 17-23, 1982.

[6] Gordon Wood Anderson, Francis J. Kub, Rebecca L. Grant, Nicolas A. Papanicolaou, John A. Modolo, and Douglas E. Brown, "Programmable frequency excision and adaptive filtering with a GaAs/AlGaAs/GaAs heterojunction photoconductor array," Optical Engineering, vol. 29, pp. 1243-1248, 1990.

[7] Robert W. Bandstetter and Philip G. Grieve, "Recursive optical notching filter," SPIE, vol. 1154, pp. 206-226, 1989.

[8] Robert W. Bandstetter and Philip G. Grieve, "Excision of interference from radio signals by means of a recursive optical notching filter," Optical Engineering, vol. 29, pp. 804-815, July 1990.

[9] J. W. Goodman, Introduction to Fourier Optics, McGraw-Hill, New York, 1968.

[10] A. VanderLugt, "Operational notation for the analysis and synthesis of optical data-processing systems," Proc. IEEE, vol. 54, pp. 1055-1063, Aug. 1966.

[11] L. Brillouin, "Diffusion de la luimiere et des rayons X par un corps transparent homogene," Ann. Phys. (Paris), vol. 17, p. 88, 1922.

[12] P. Debye and F. W. Sears, "Scattering of Light by Supersonic Waves," Proc. Nat. Acad. Sci., vol. 18, p. 409, 1932.

[13] R. Lucas and P. Biquard, "Proprietes milieux solides et liquides soumis aux vibrations elastiques ultra sonores," J. Phys. Radium, vol. 3, p. 464, 1932.

[14] C. V. Ramam and N. S. Nagendra Nath, "The Diffraction of Light by High Frequency Sound Waves: Part I," Proc. Indian Acad. Sci., vol. 2A, p. 406, 1935; "Part II," vol. 2A, p. 413, 1935; "Part III-Doppler Effect and Coherent Phenomena," vol. 3A, p. 75, 1936; "Part IV-Generalised Theory," vol. 3A, p. 119, 1936; "Part V-General Considerations-Oblique Incidence and Amplitude Changes," vol. 3A, p. 359, 1936.

[15] Harris Corporation, Presort Processor Final Report, 1986.

[16] E. Hecht, Optics, Addison-Wesley, Reading, MA 1987.

8. Figures

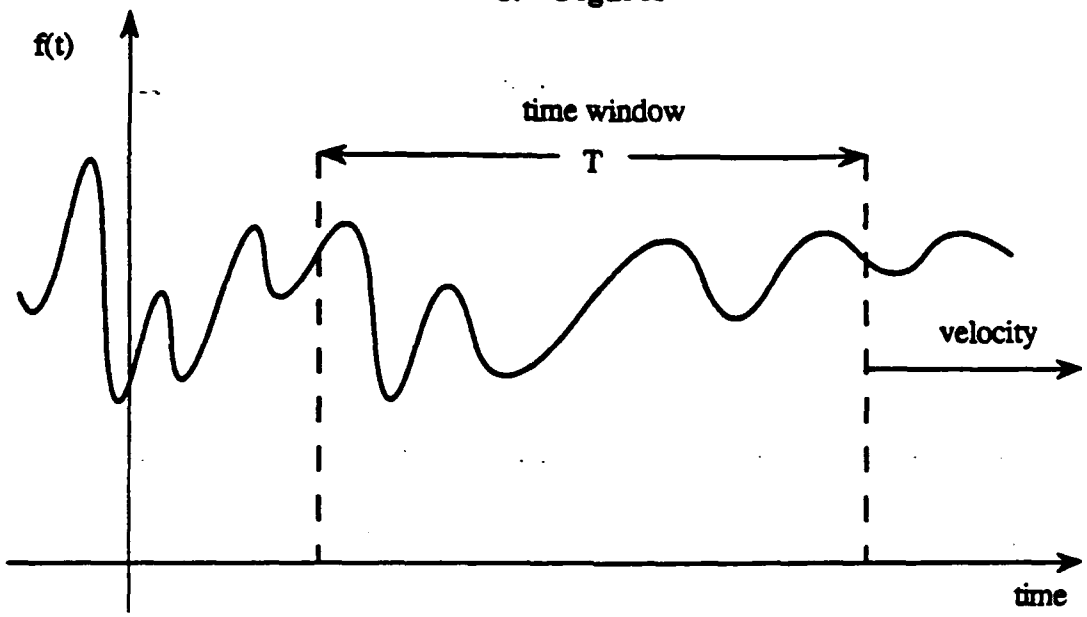

Figure 2.1a: Representation of time window of the Fourier transform

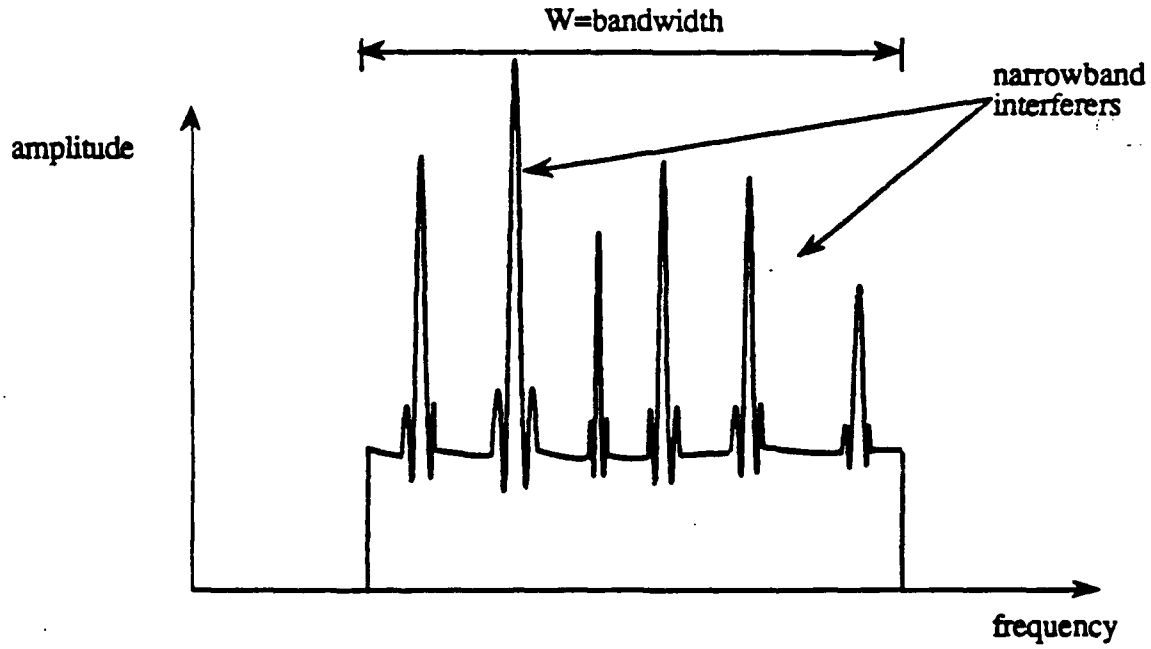

Figure 2.1b: Spectrum of received signal

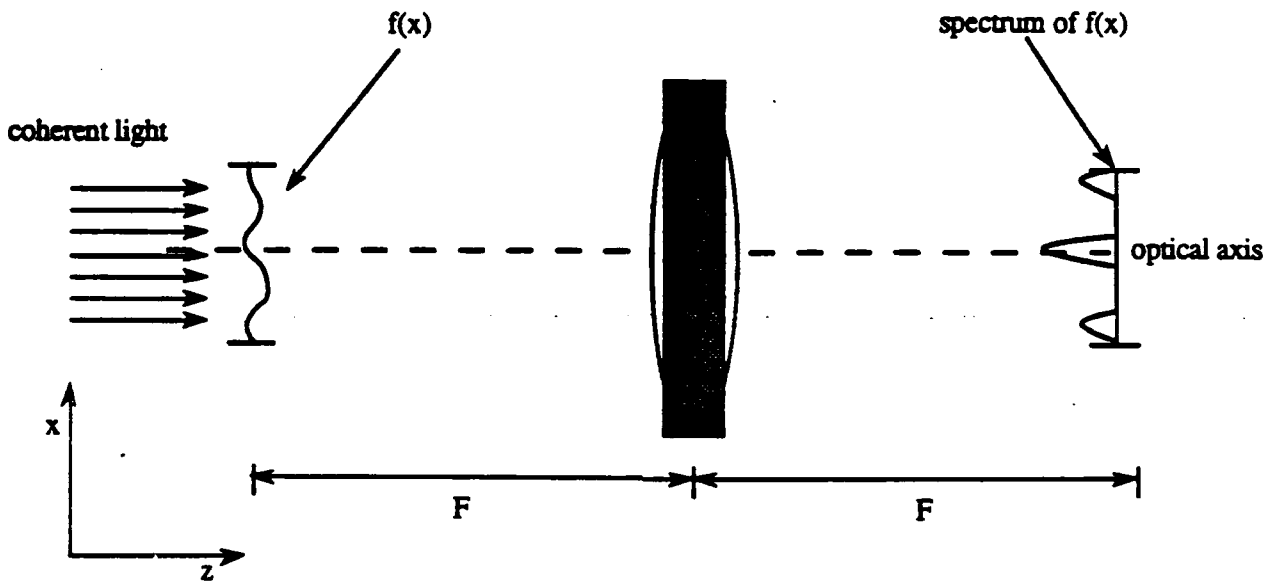

Figure 2.2: Optical Fourier transform system

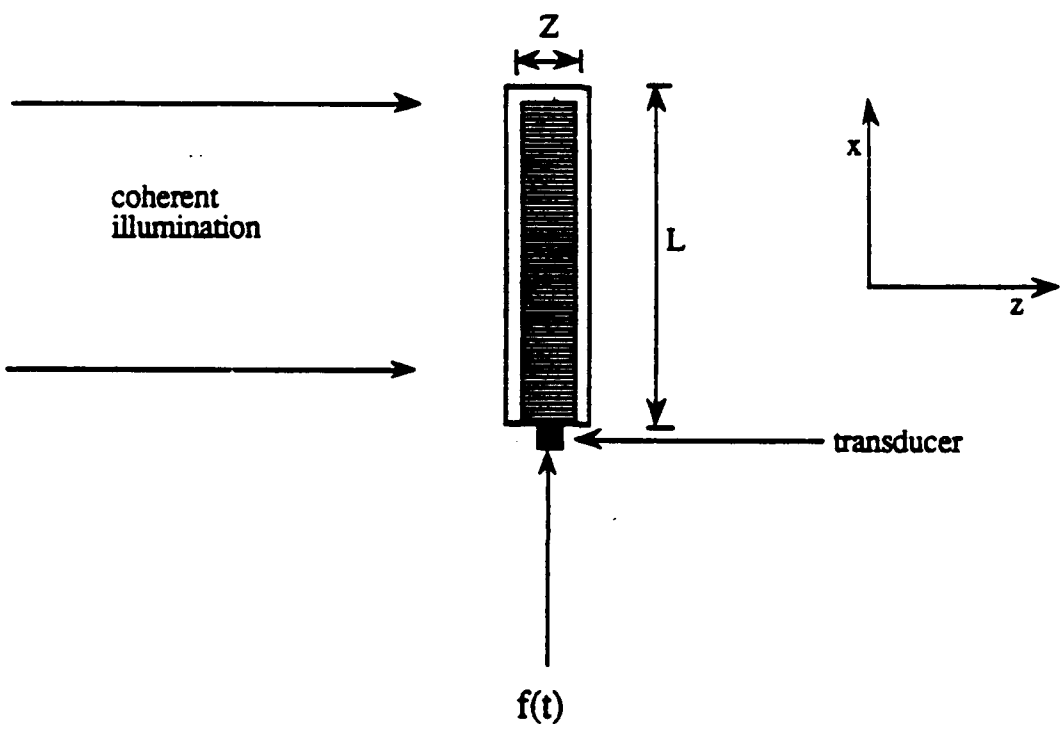

Figure 2.3: Parameters of an acousto-optic cell

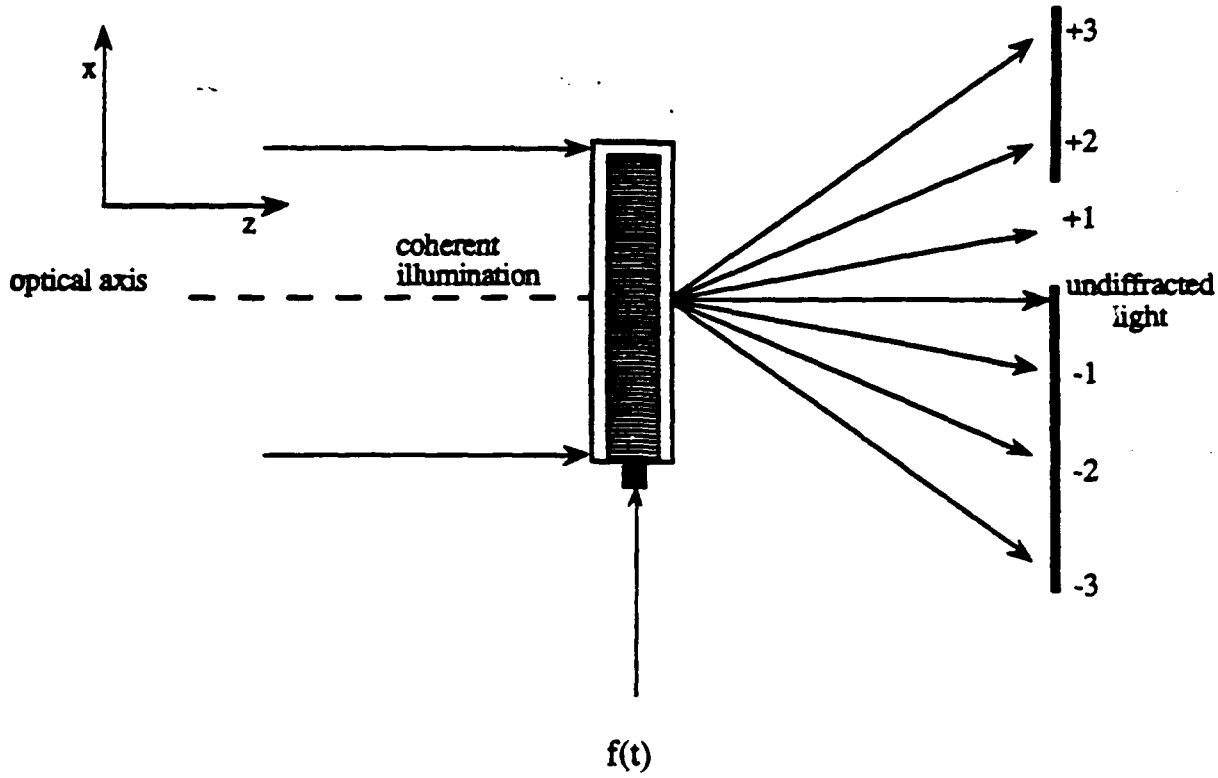

Figure 2.4: Raman-Nath mode of operation

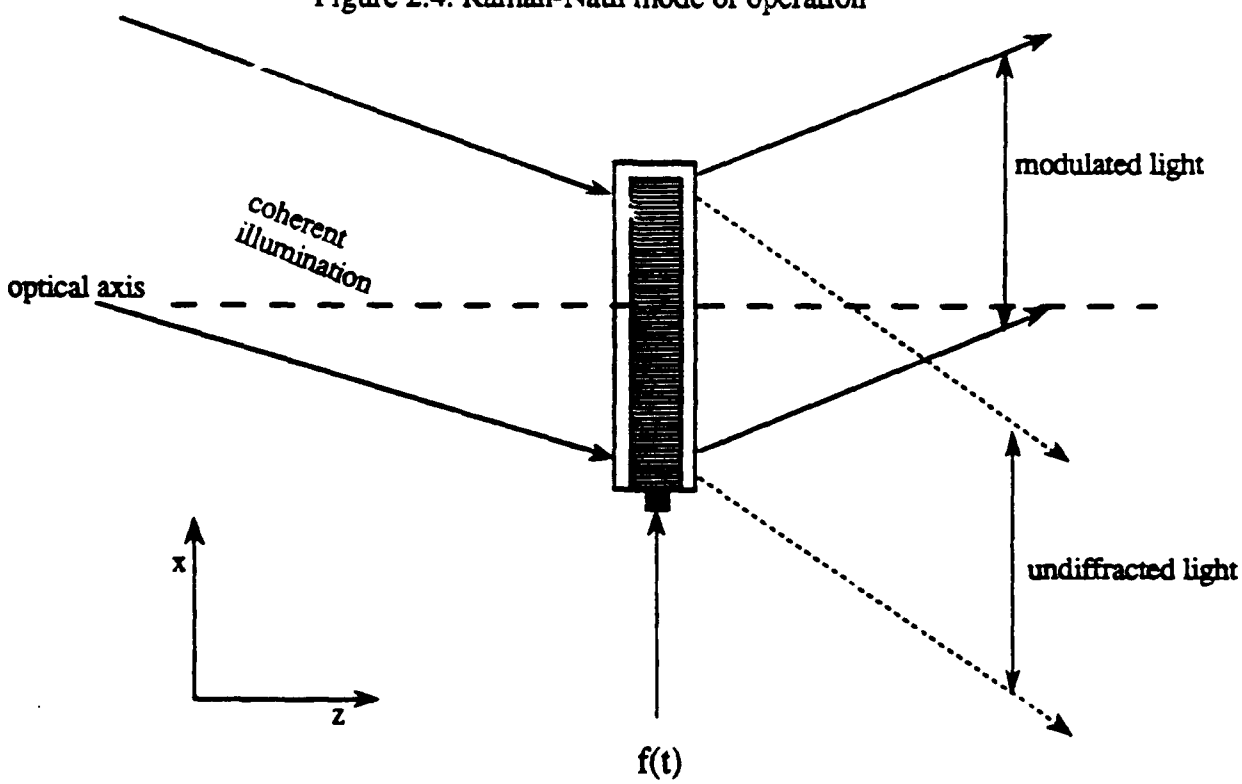

Figure 2.5: Bragg mode of operation

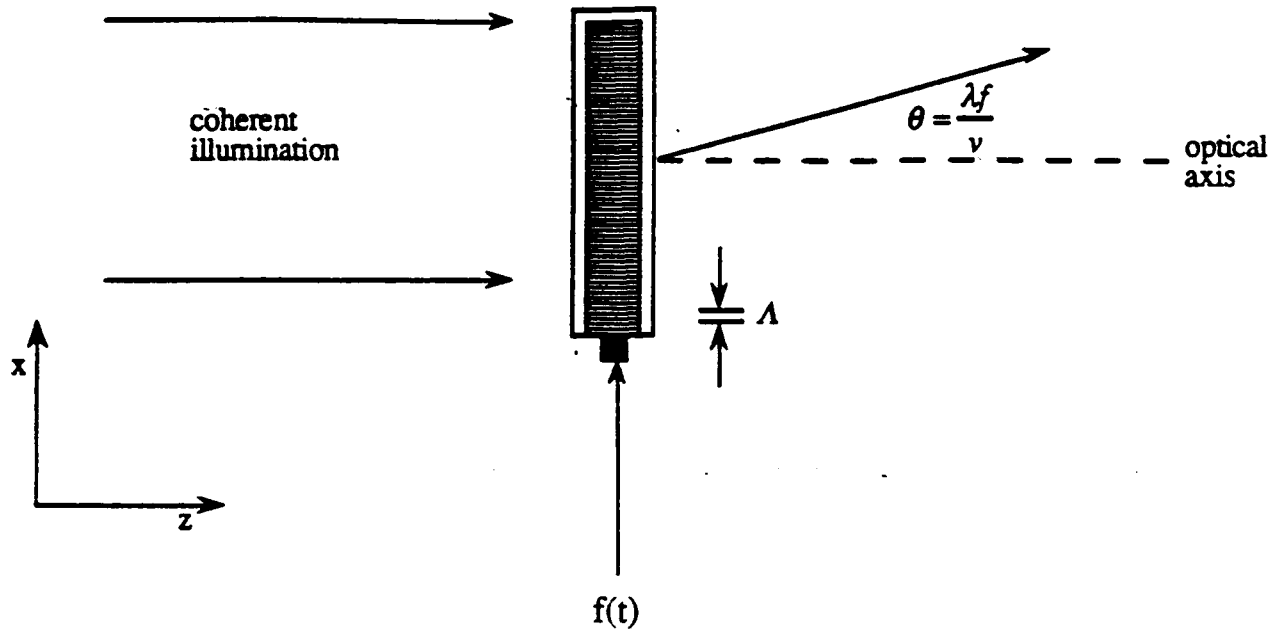

Figure 2.6: Relationships of the acousto-optic cells

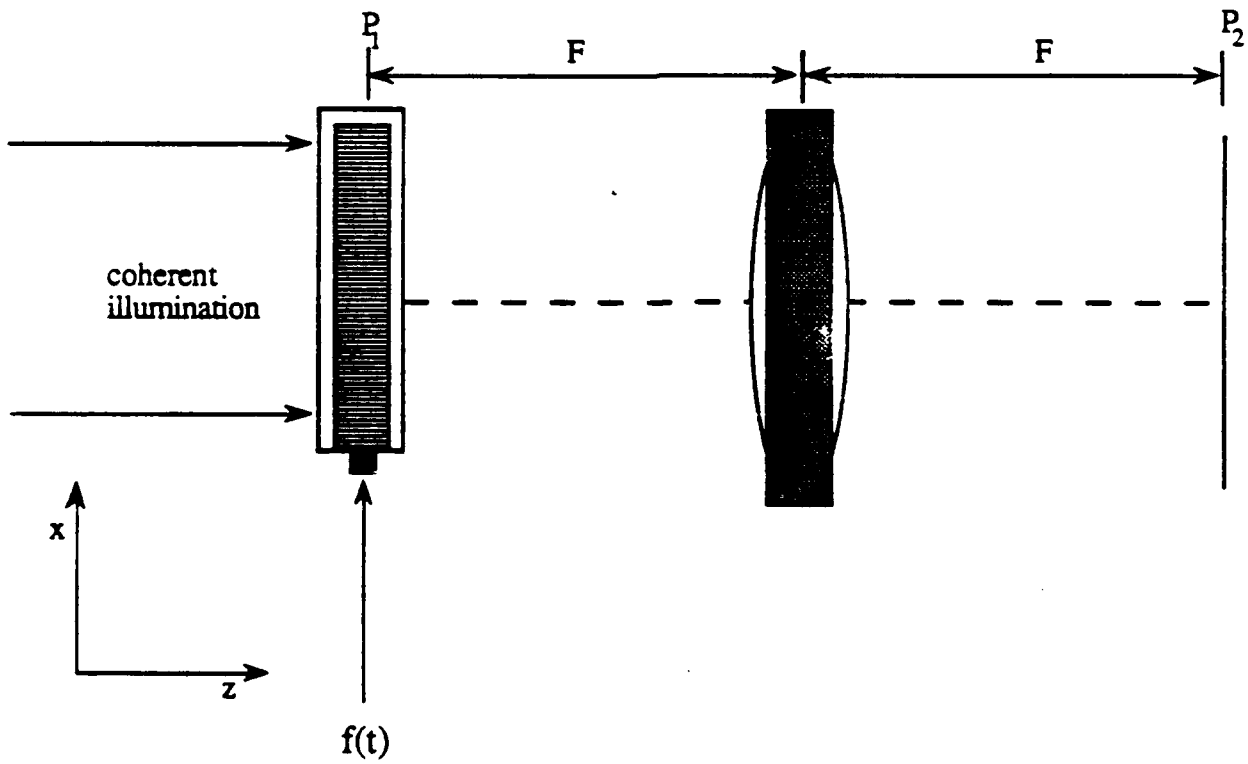

Figure 2.7: Fourier transform configuration

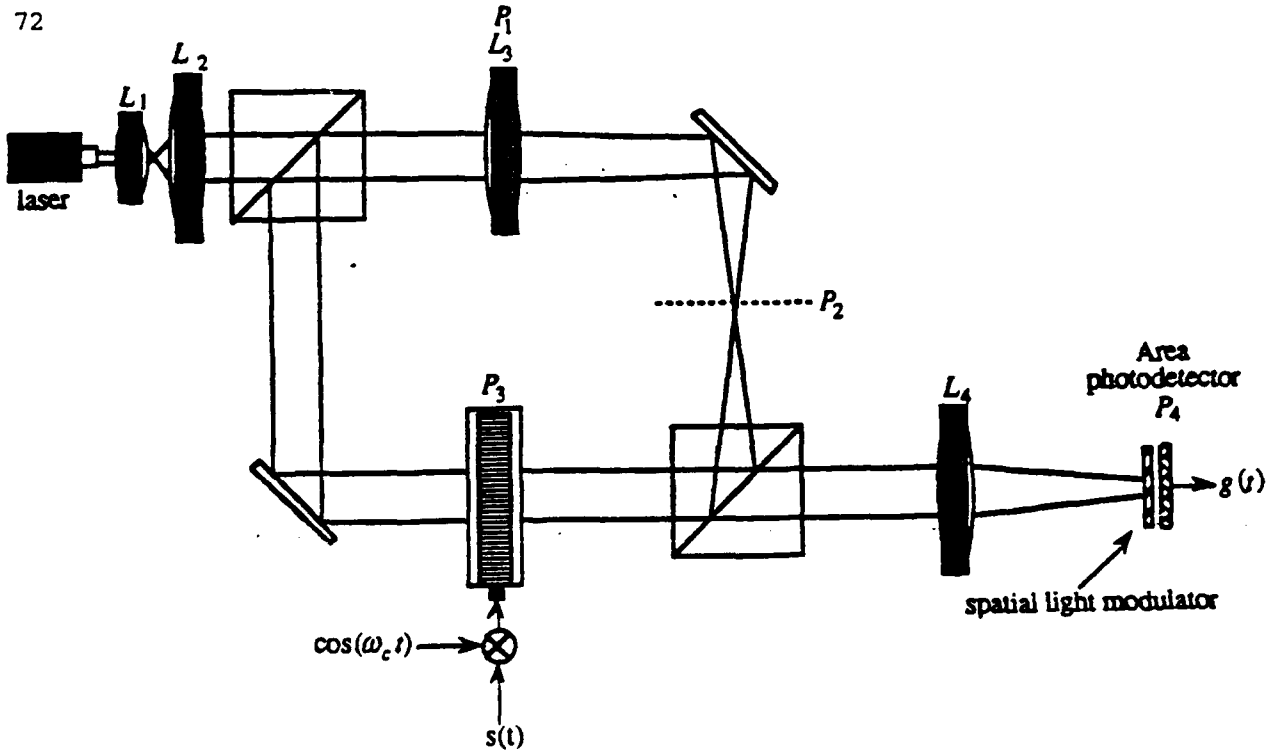

Figure 3 1: Area detection in the Fourier plane

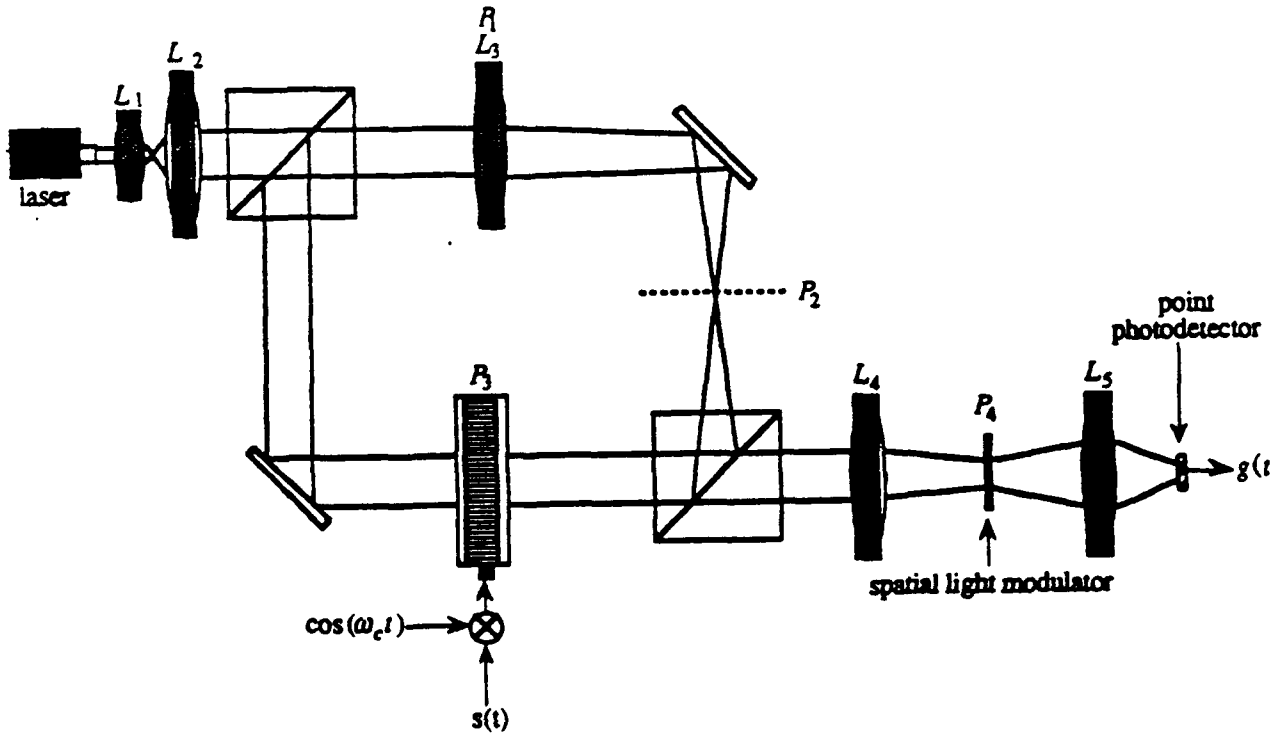

Figure 3.2: Point detection in the image plane

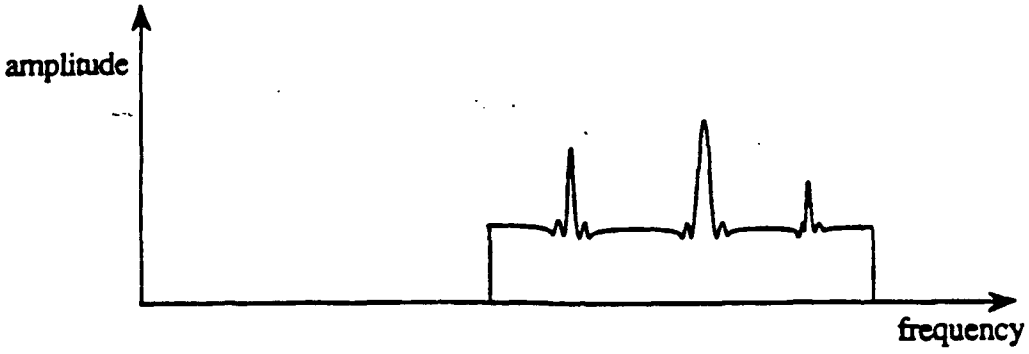

Figure 3.3: Wideband spectrum corrupted by narrowband interferers

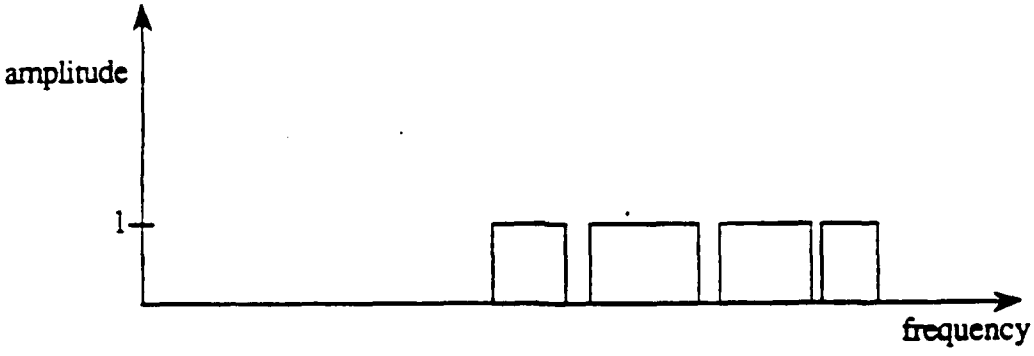

Figure 3.4: Notch filter response

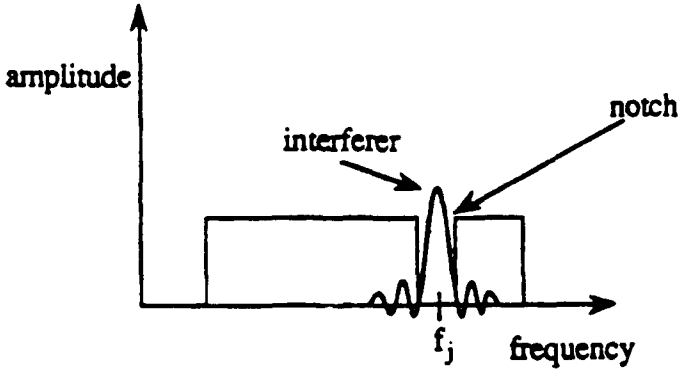

Figure 3.5a: Notch filter and interferer

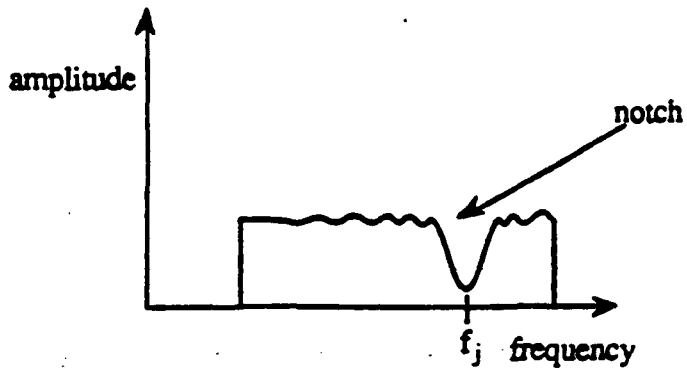

Figure 3.5b: Filter response

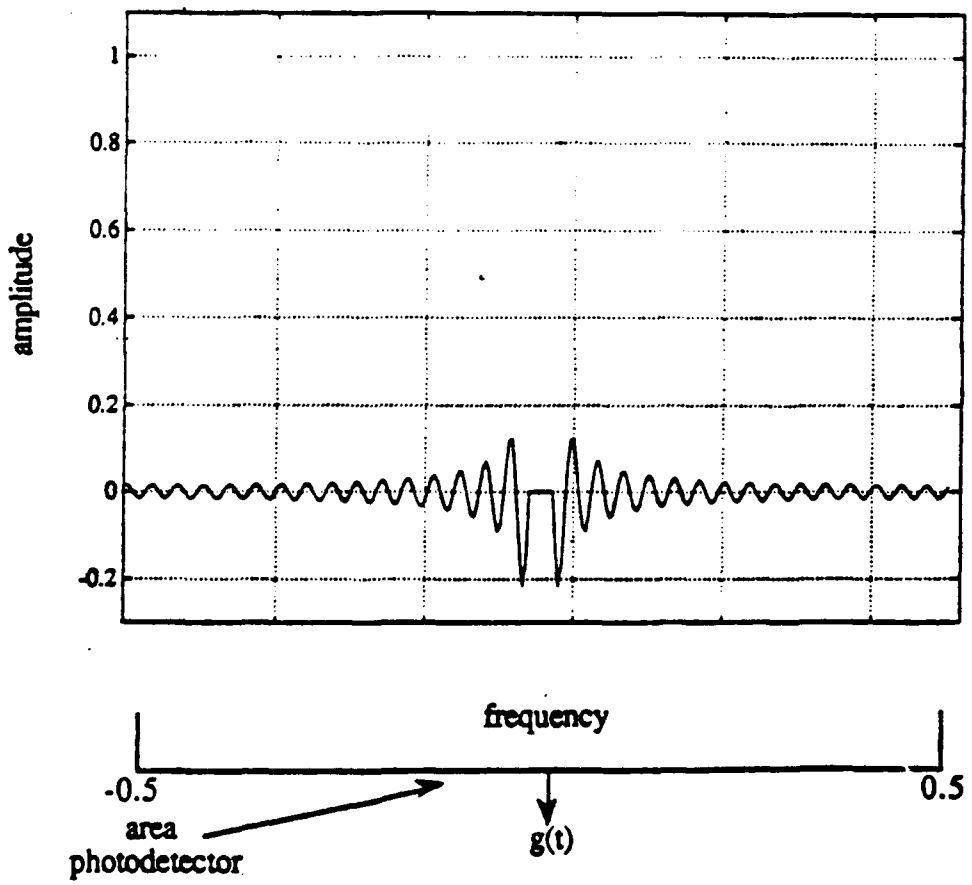

Figure 3.6: Sinc function with mainlobe excised

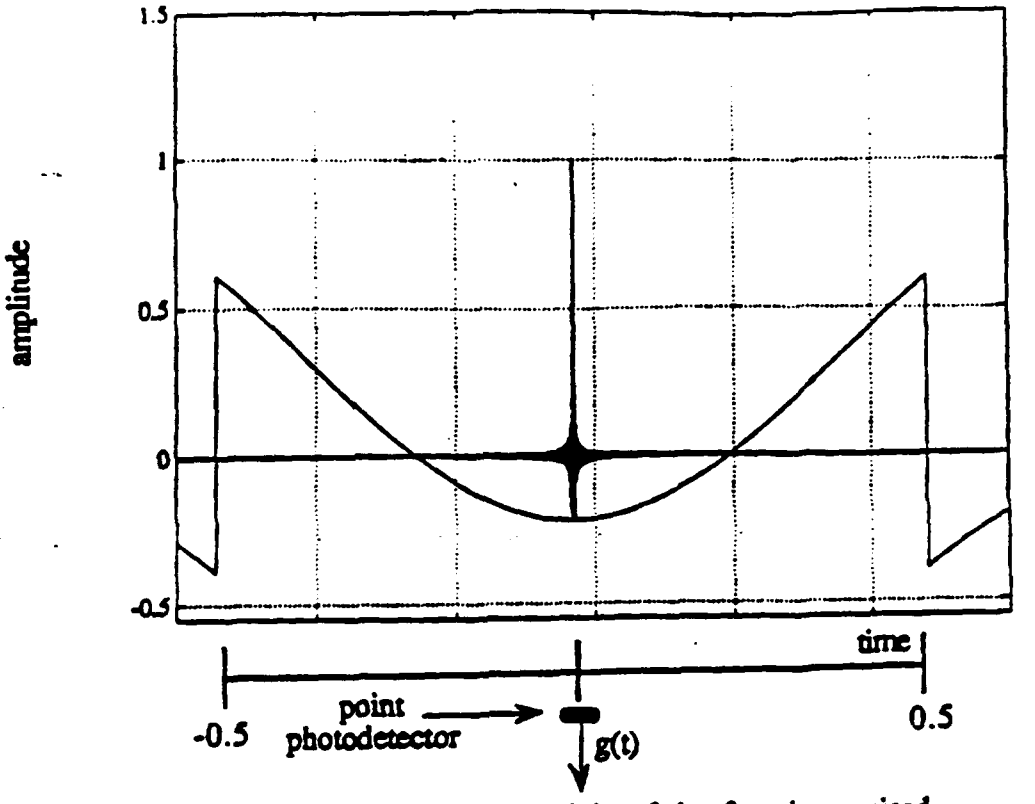

Figure 3.7: Output image plane with mainlobe of sinc function excised

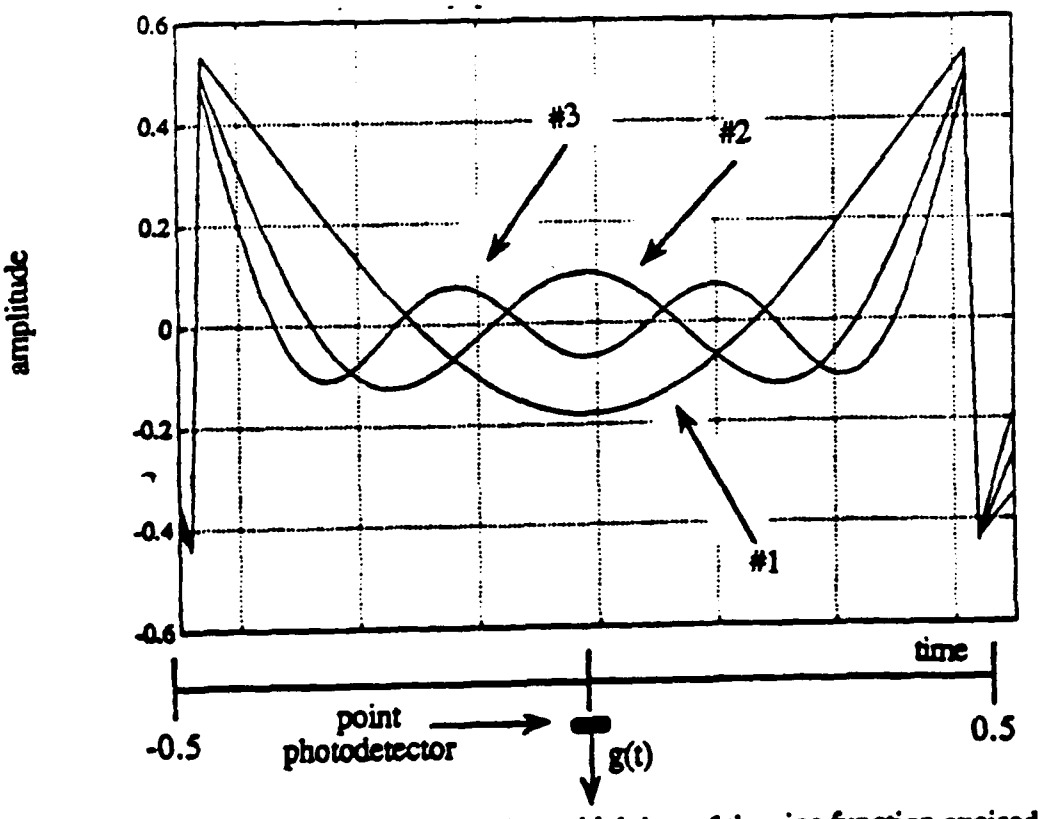

Figure 3.8: Output image plane with various sidelobes of the sinc function excised

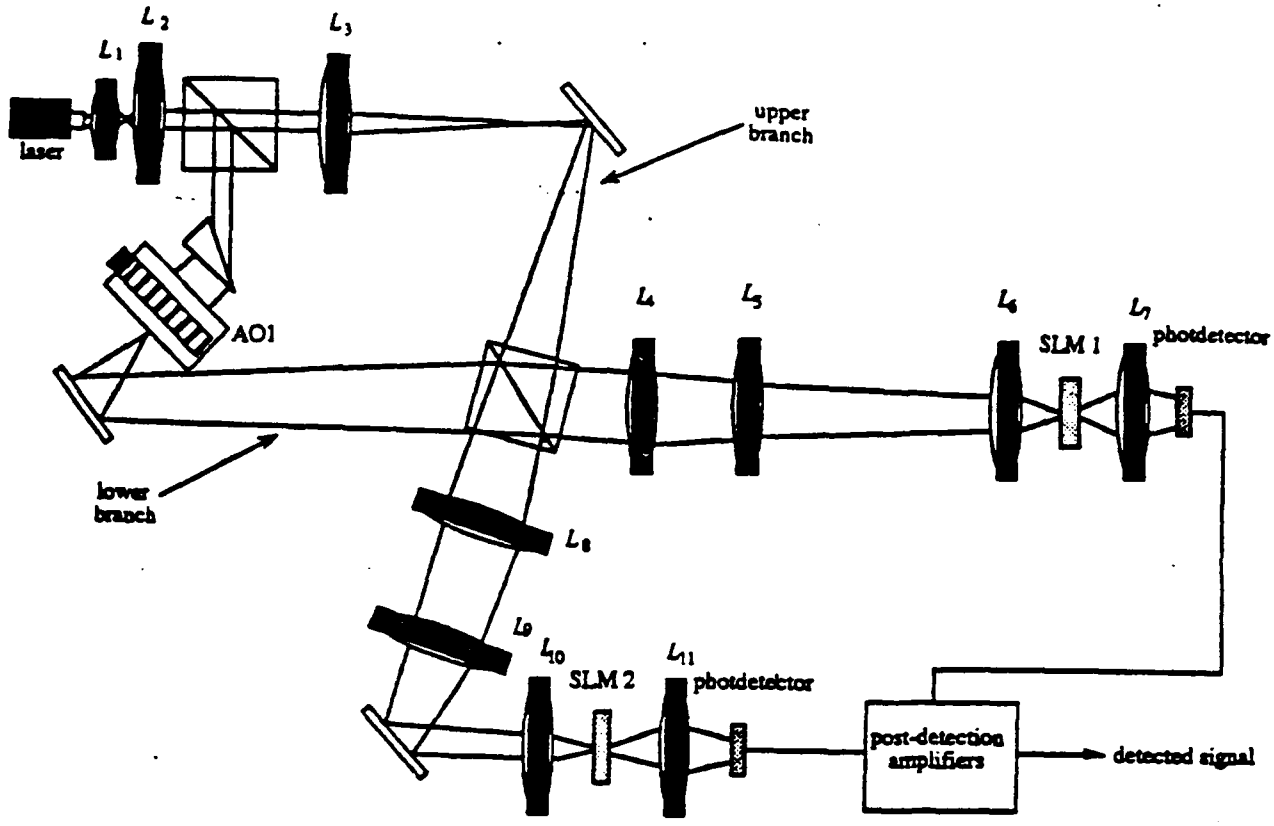

Figure 4.1: Presort Processor

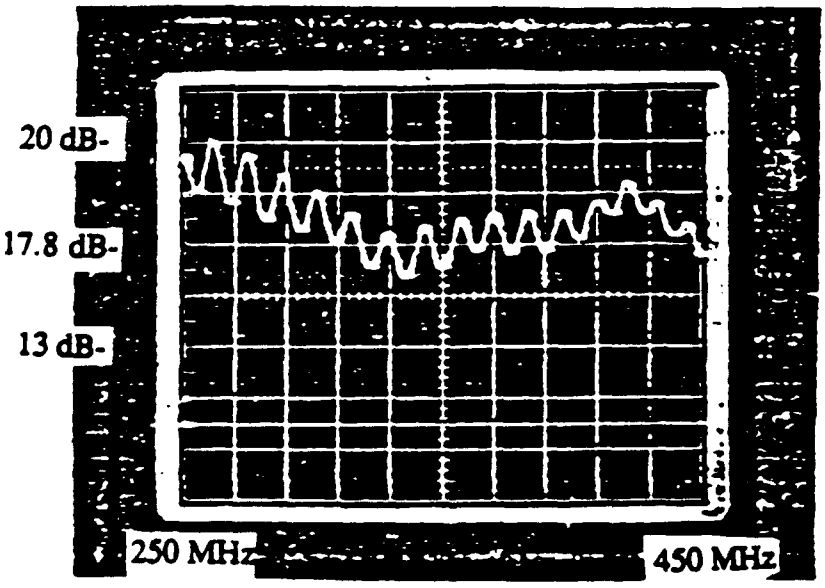

Figure 4.2: Passband of the signal acousto-optic cell

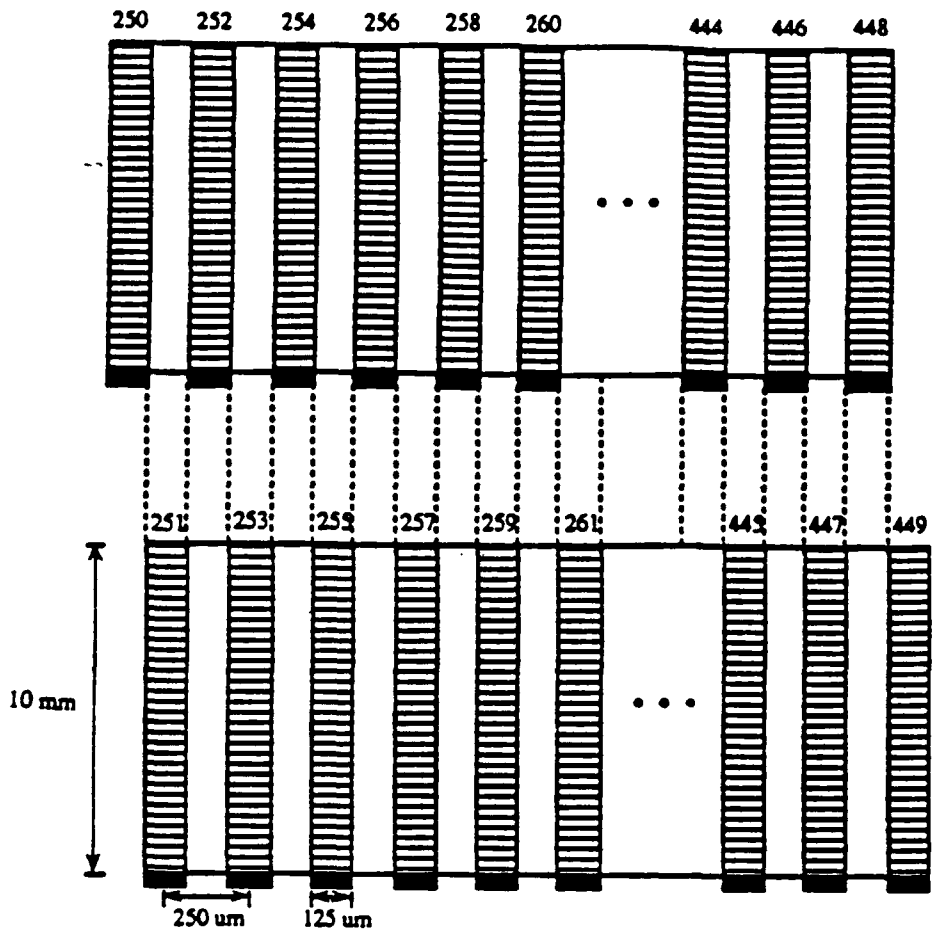

Figure 4.3: Spatial light modulators

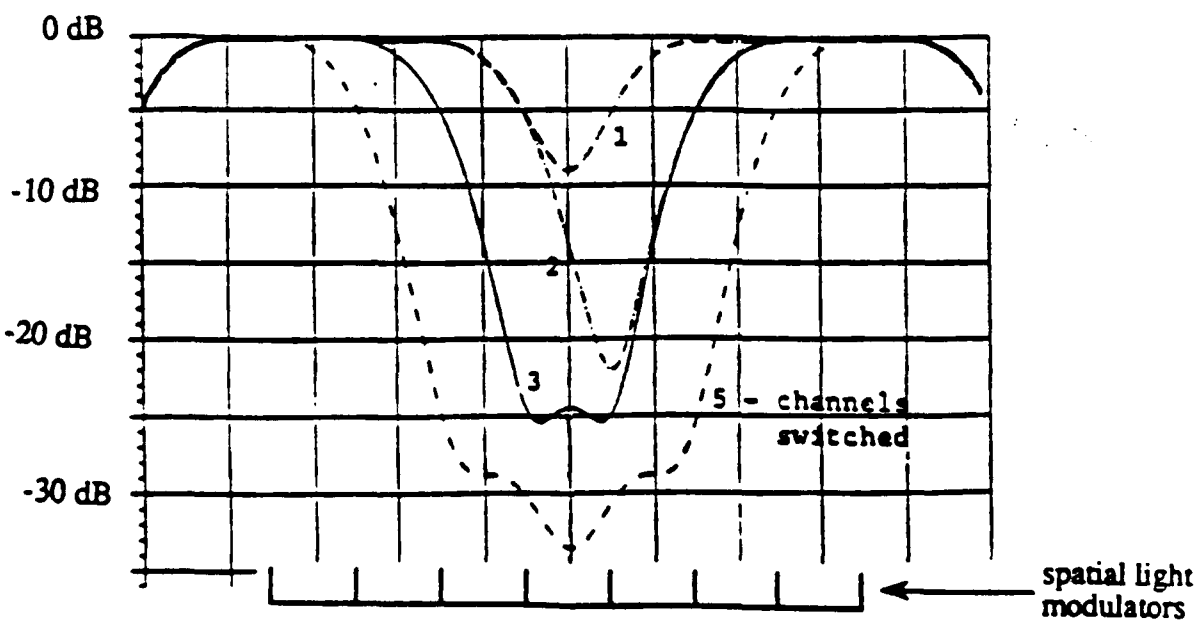

Figure 4.4: The theoretical notch shape

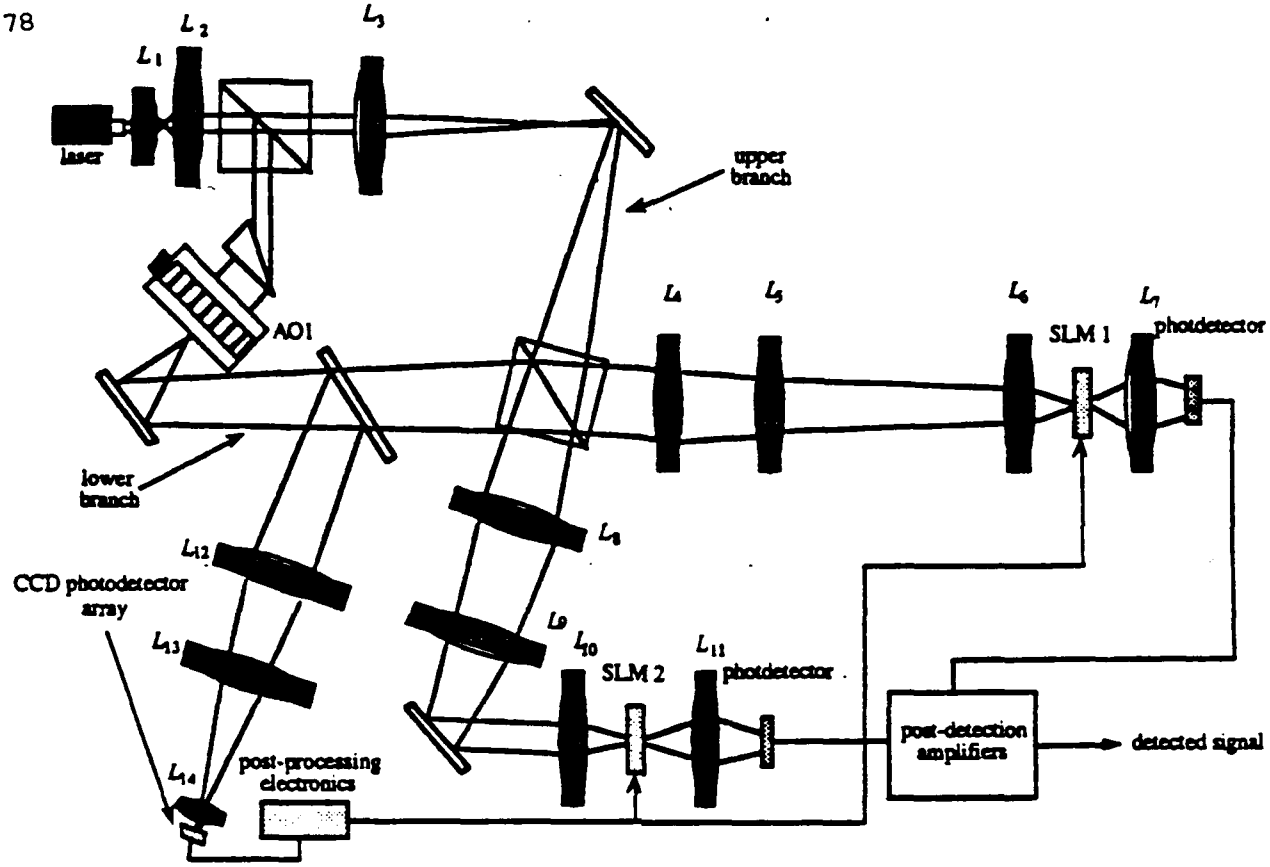

Figure 4.5: Presort Processor modified

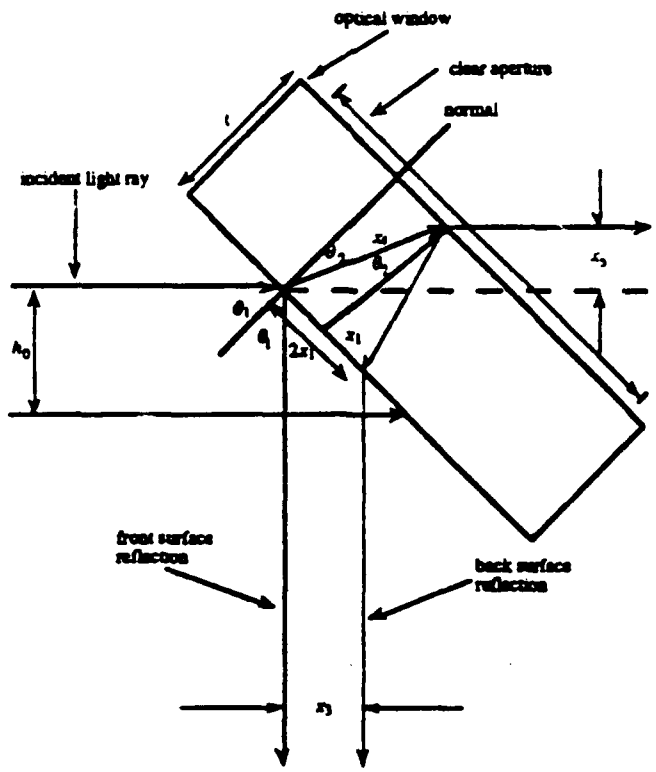

Figure 4.6: Representation of the displacements of the optical beams

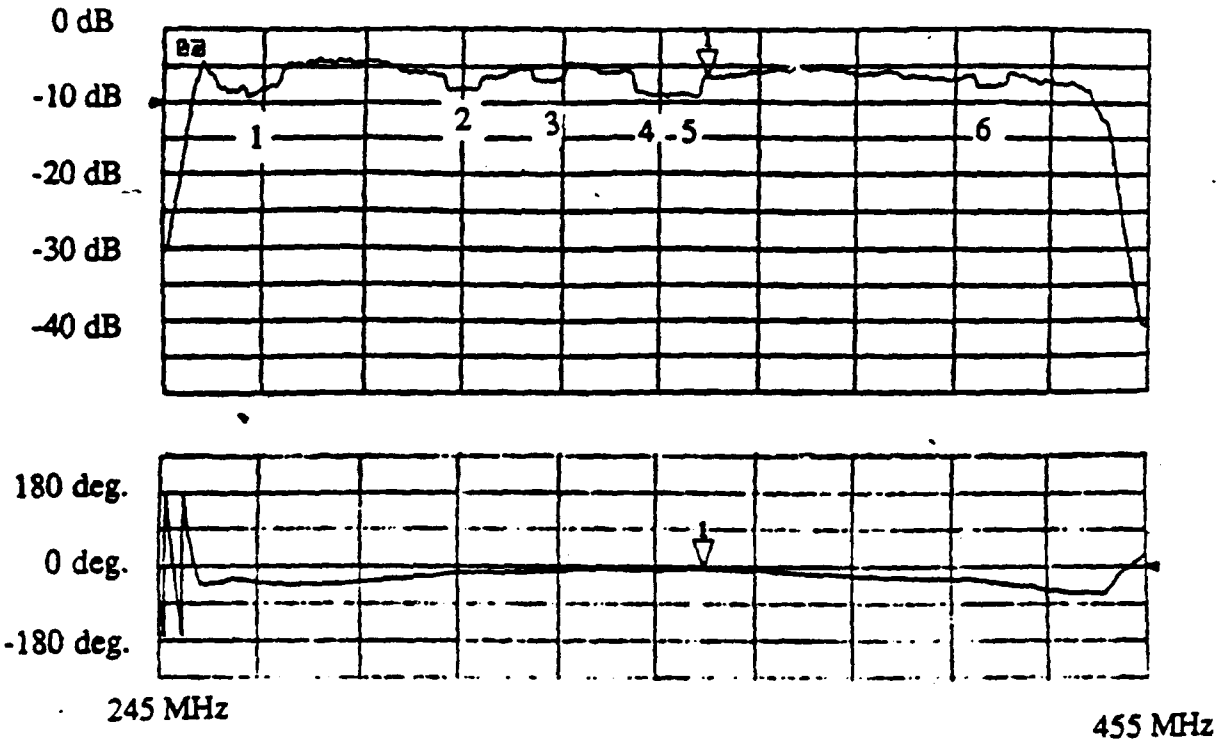

Figure 4.7: Amplitude and phase response of the Presort Processor

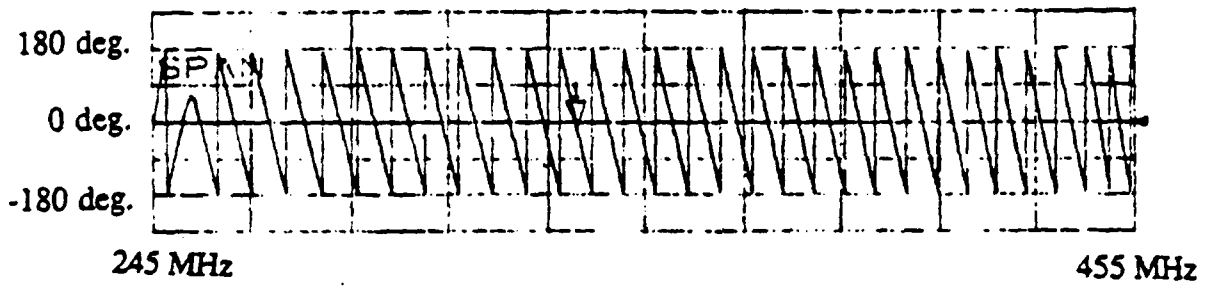

(a) phase response after window is inserted

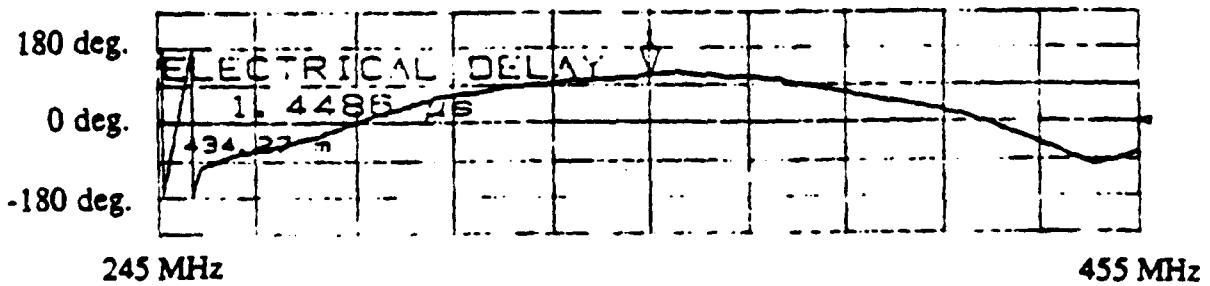

(b) phase response after linear phase is nulled

Figure 4.8: Phase response after the optical window is inserted into the Presort Processor

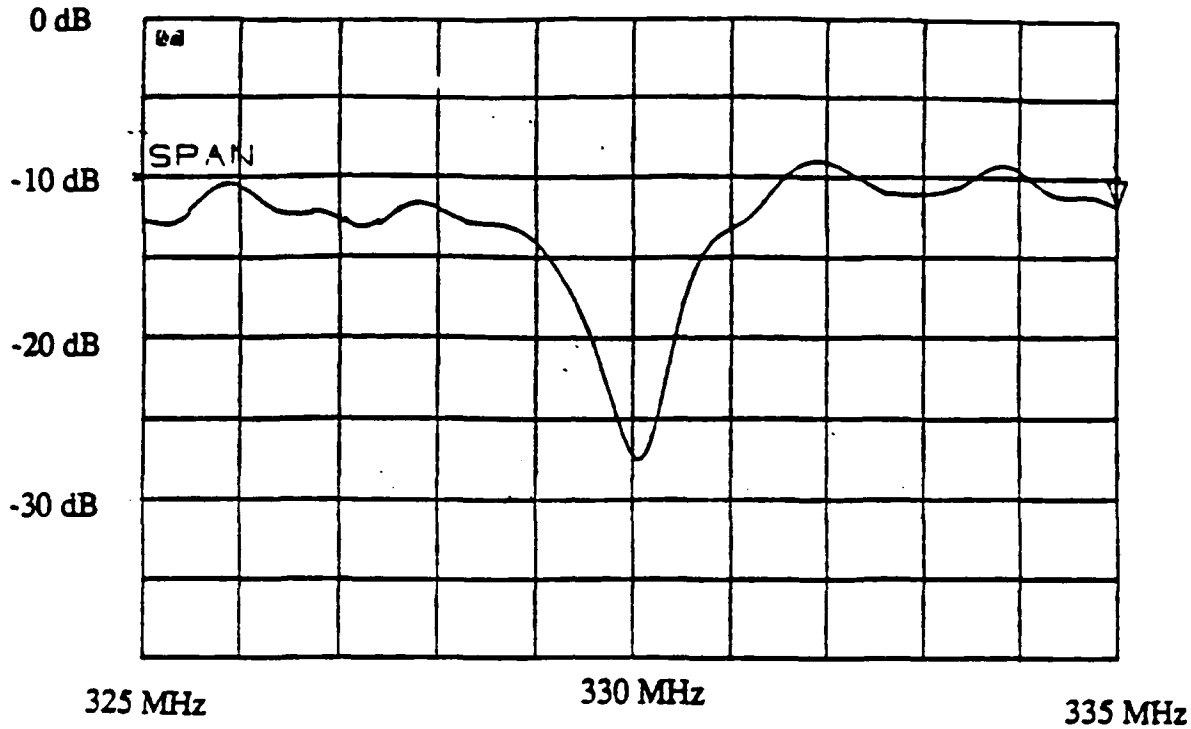

(a) Expanded view of the amplitude response before the optical window is inserted

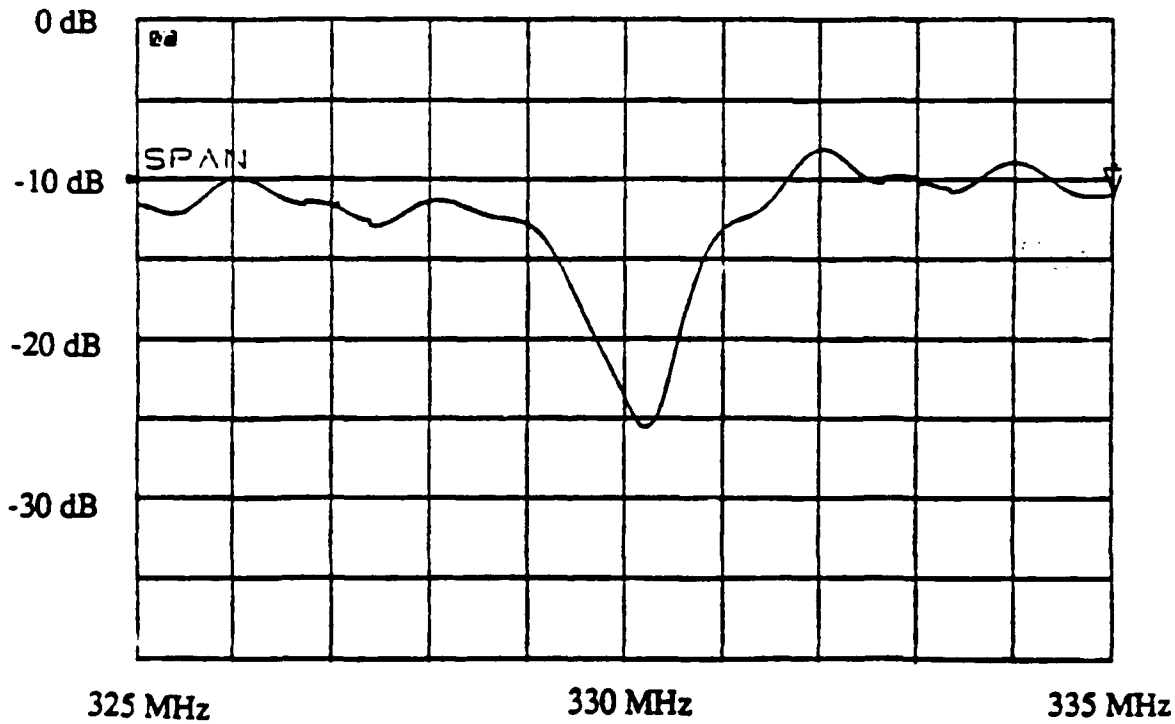

(b) Expanded view of the amplitude response after the optical window is inserted

Figure 4.9: Amplitude response before and after the optical window is inserted

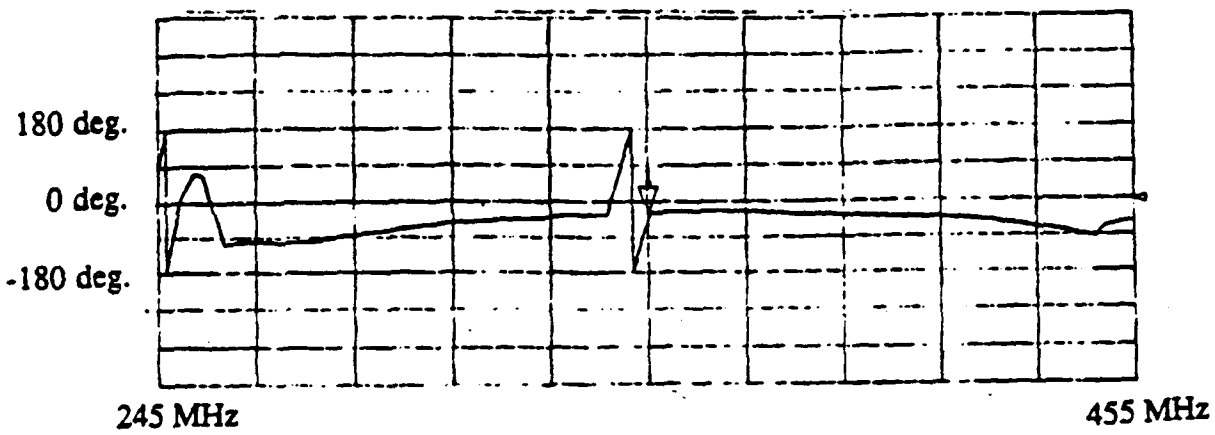

Figure 4.10: Phase response after the corrective optical window is positioned in the upper branch

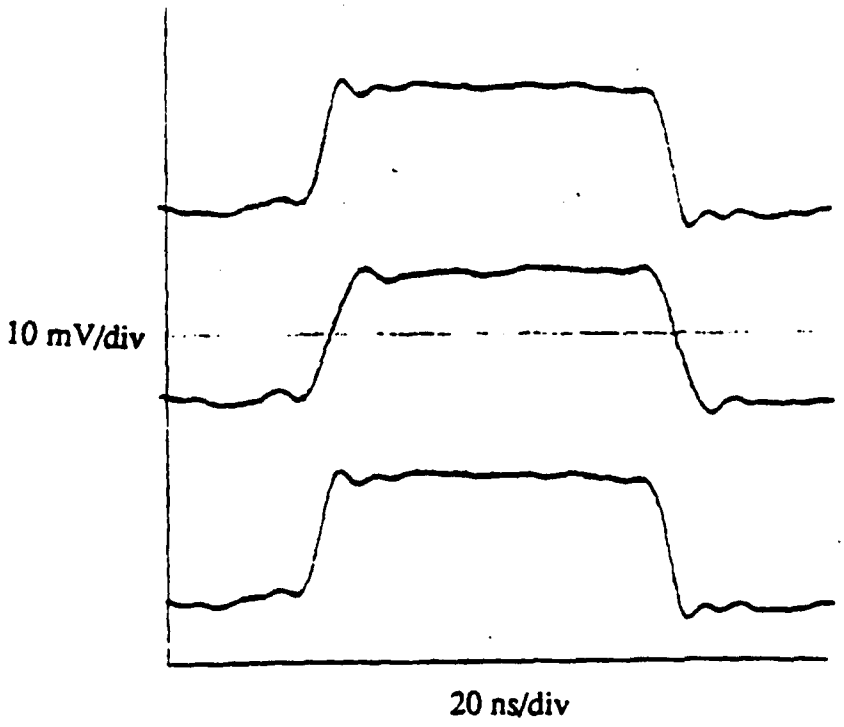

Figure 4.11: Pulse before the primary optical window is inserted, after the primary optical window is inserted, and after the corrective optical window is inserted.

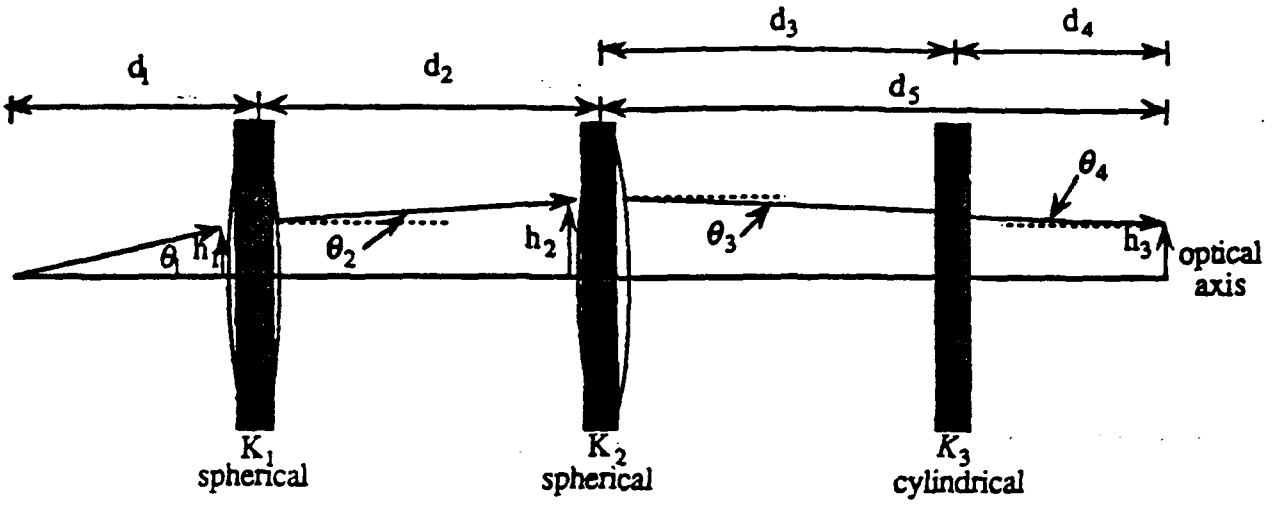

Figure 4.12: Fourier transform direction of the optical system

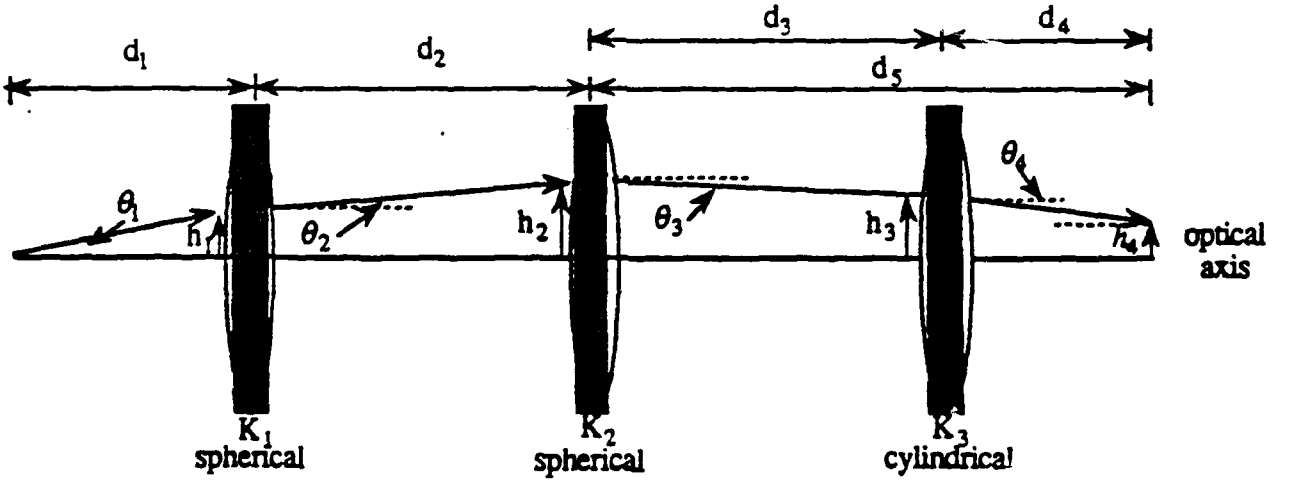

Figure 4.13: Image direction of the optical system

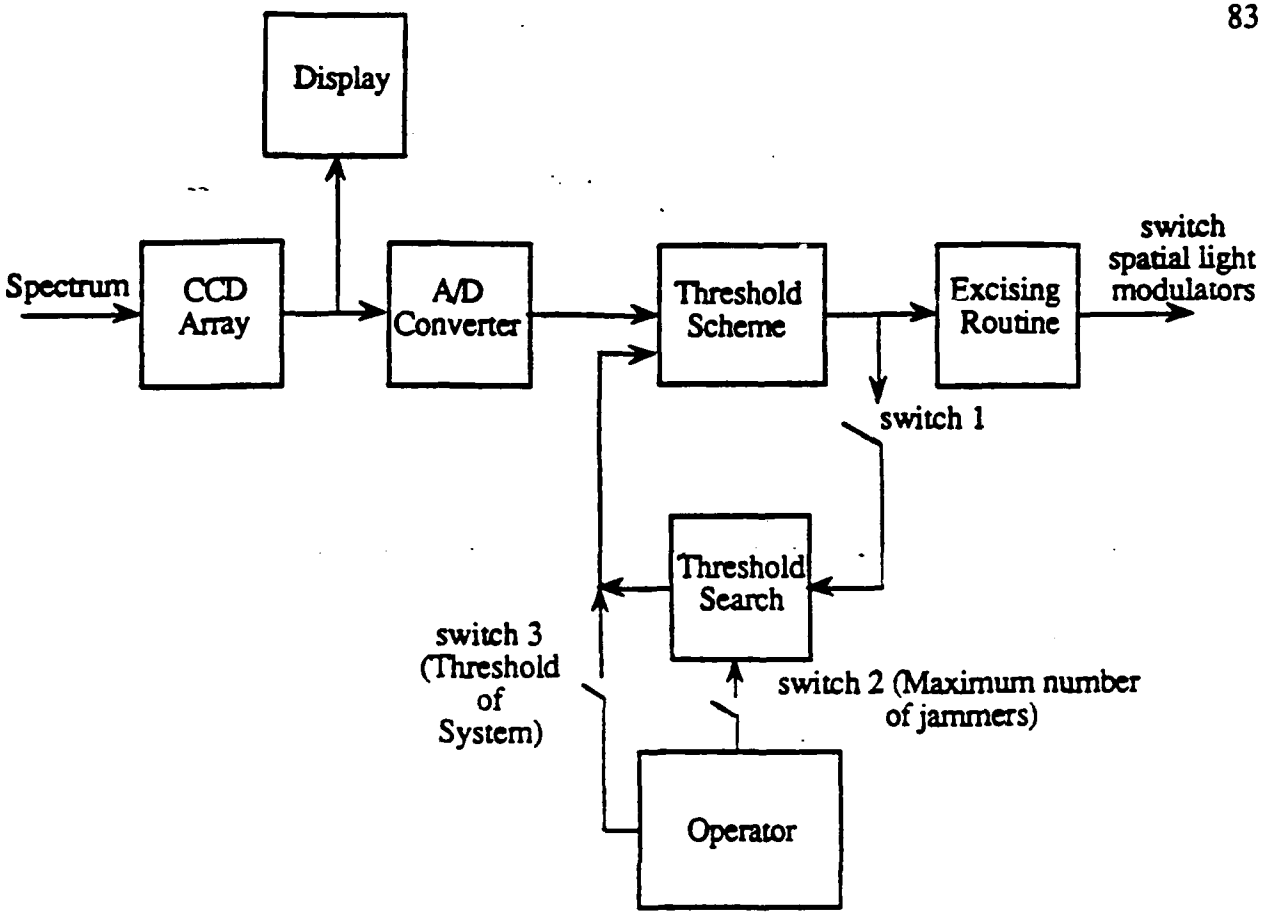

Figure 4.14: Block diagram of the digital system

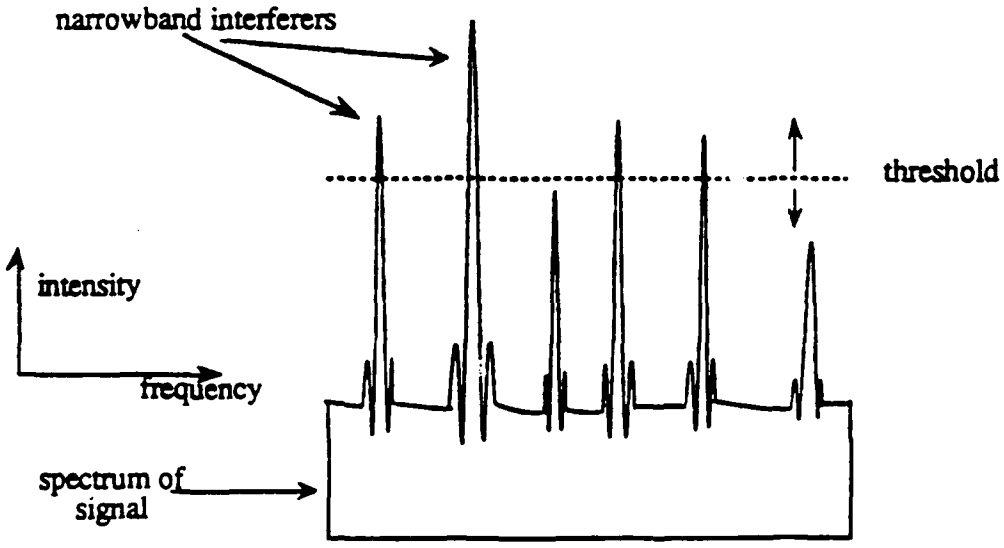

Figure 4.15: Spectrum of a signal distorted by narrowband interferers

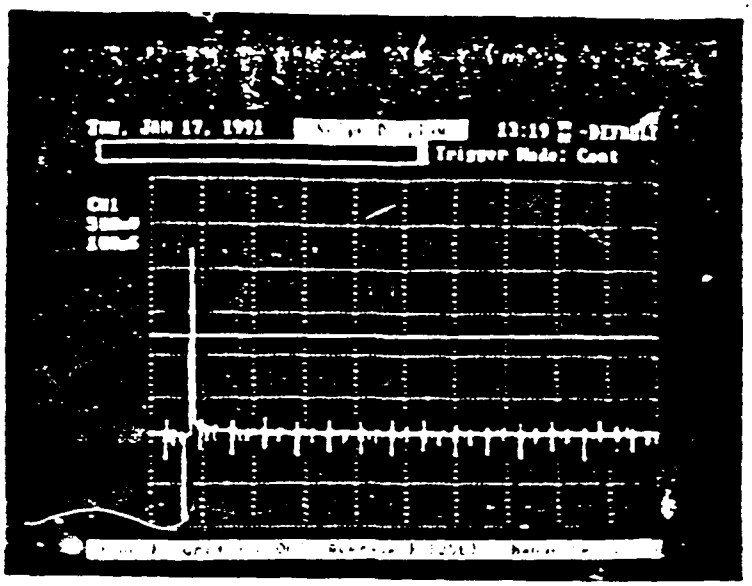

Figure 4.16: The display with one narrowband interferer excised

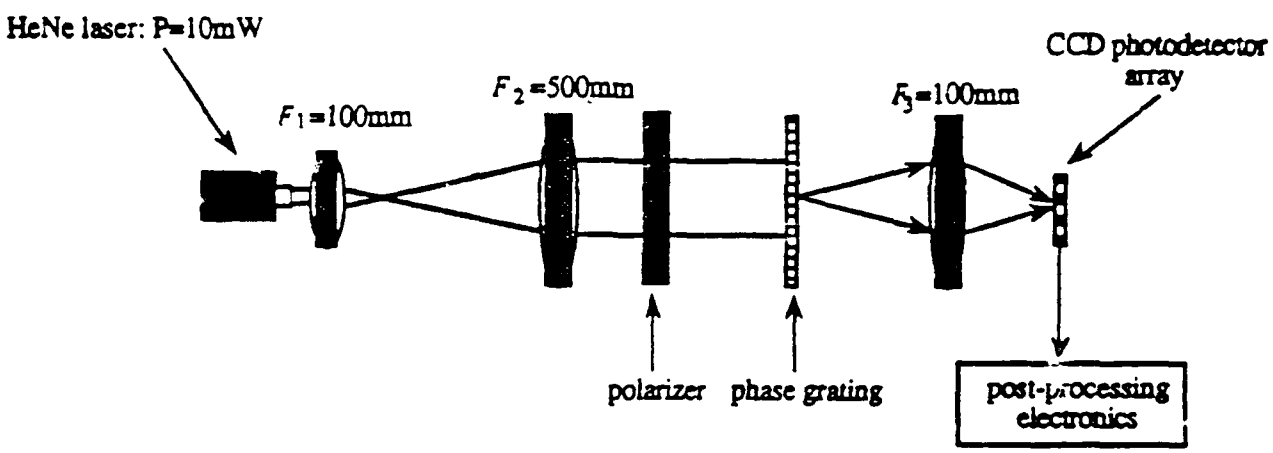

Figure 4.17: Experimental setup for the testing of the post-processing electronics

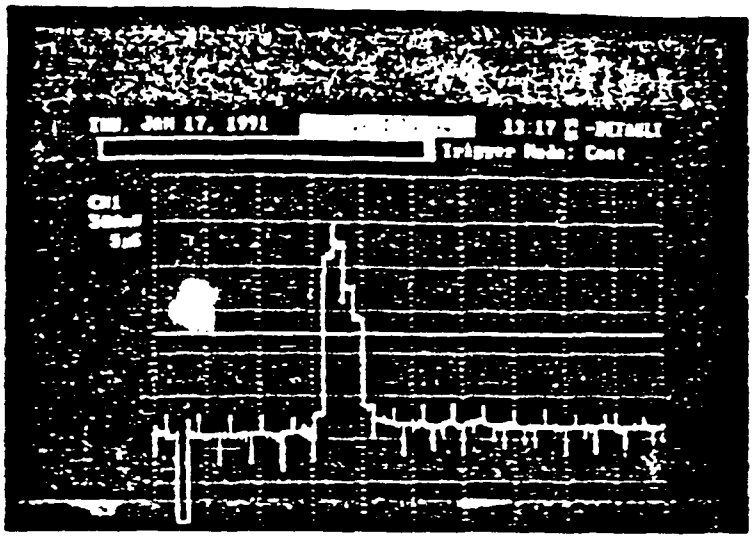

Figure 4.18: The spectrum with the threshold level at a steady-state value

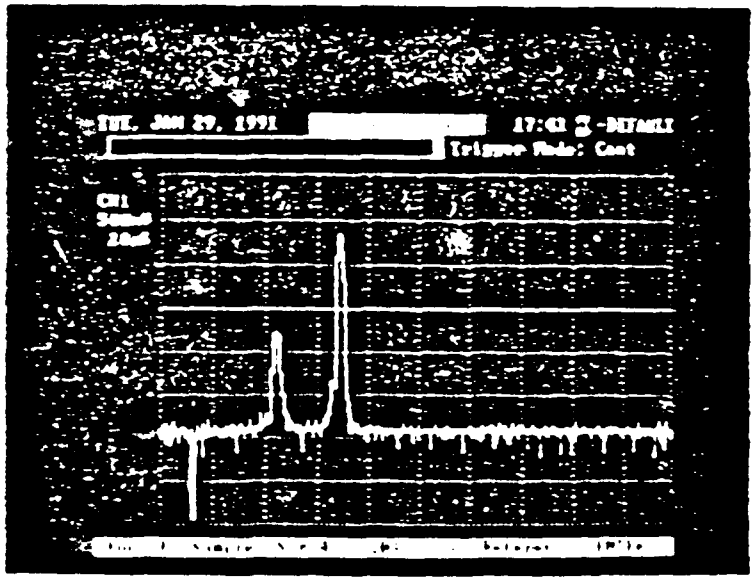

Figure 4.19: The spectrum with with two different strength interferers with the threshold at a steady state value

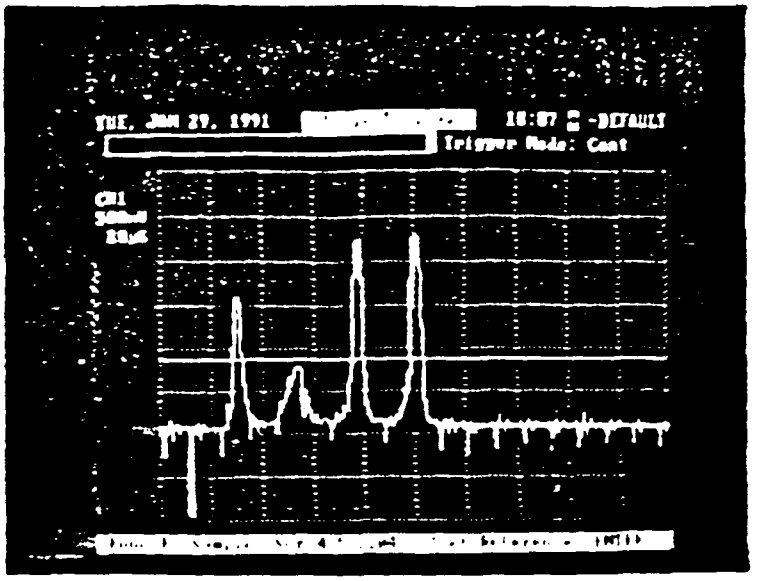

Figure 4.20: The spectrum with multiple narrowband interferers

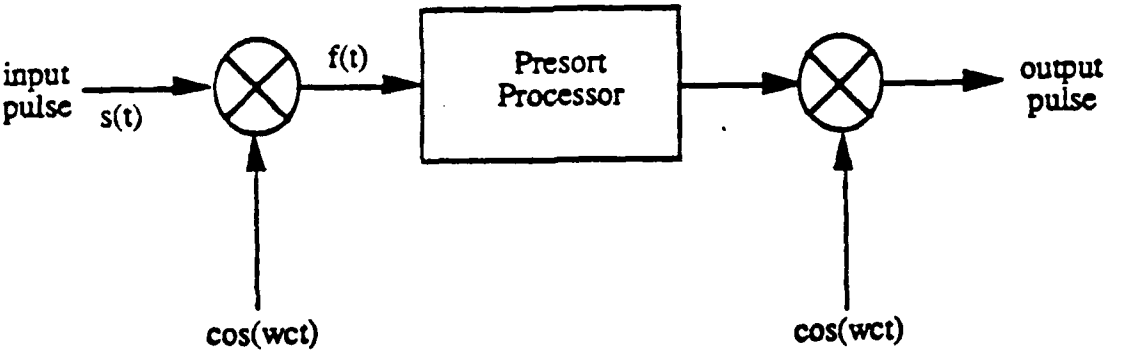

Figure 5.1: Block diagram of the experimental system

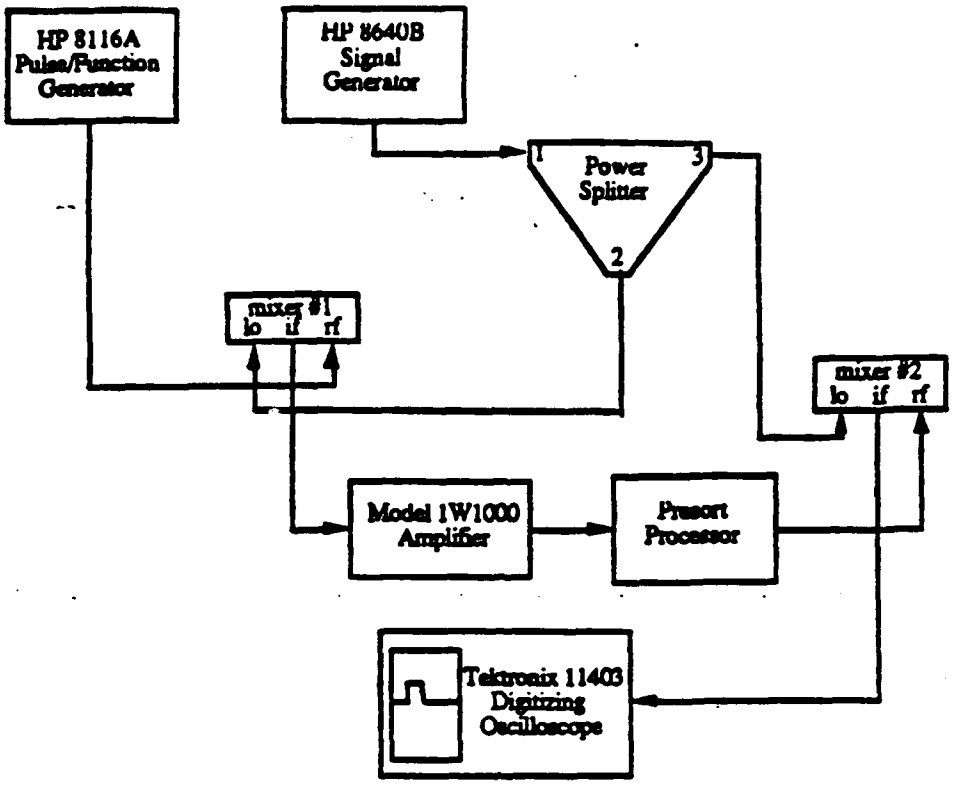

Figure 5.2: Experimental equipment setup

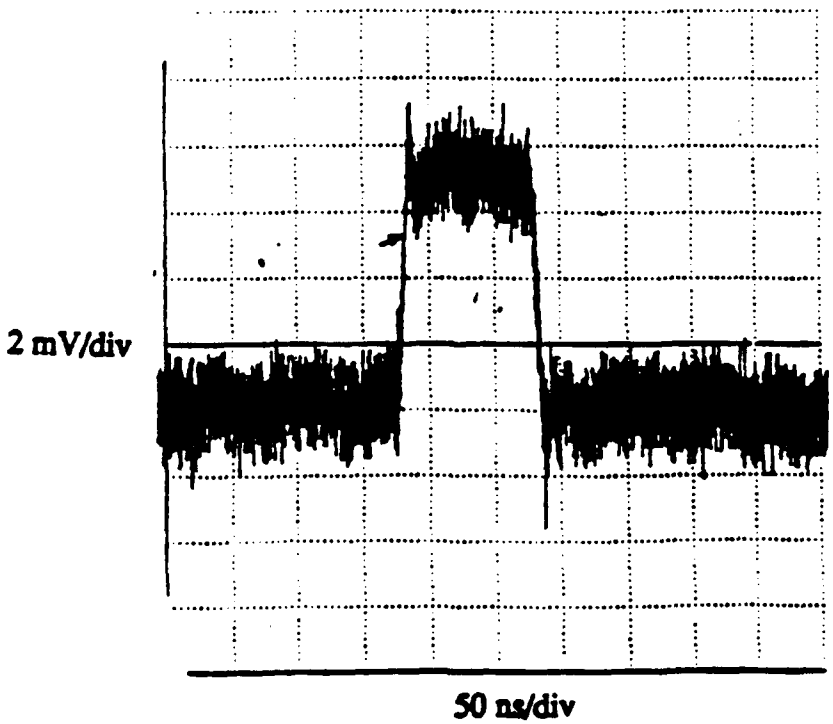

Figure 5.3: Signal that is available on a one-shot basis

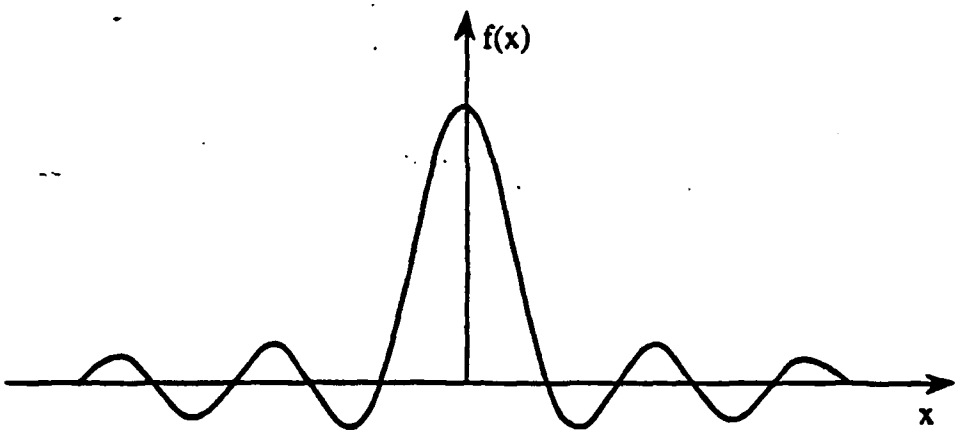

(a) Fourier transform of a pulse

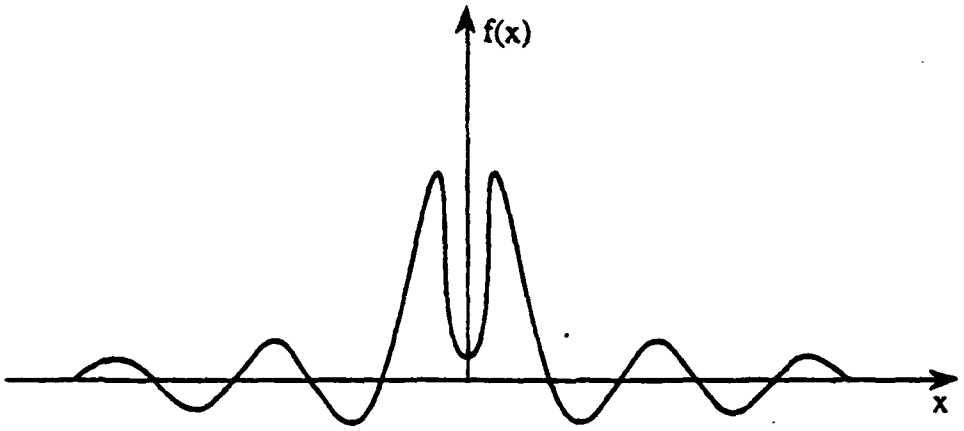

(b) Center-value of sinc function removed

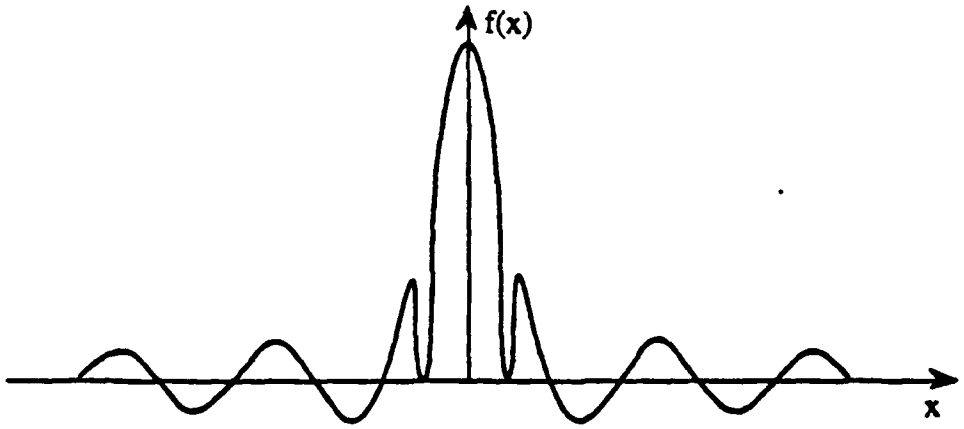

(c) Symmetric removal of frequency components from a sinc function

Figure 5.4: Examples of various frequency components removed from a sinc function

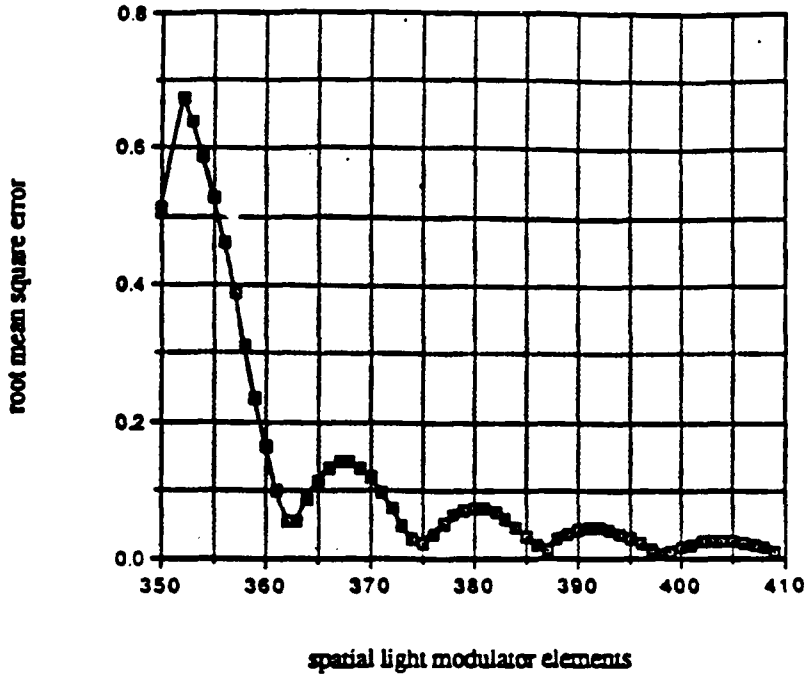

Figure 5.5: Computer simulation: root mean square error versus spatial light modulators elements

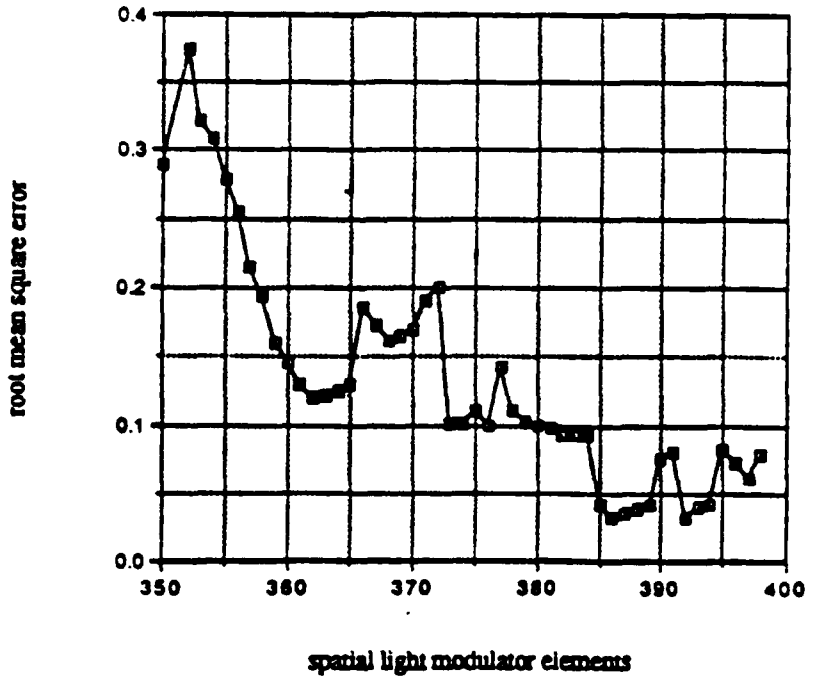

Figure 5.6: Experimental results: root mean square error versus spatial light modulators elements

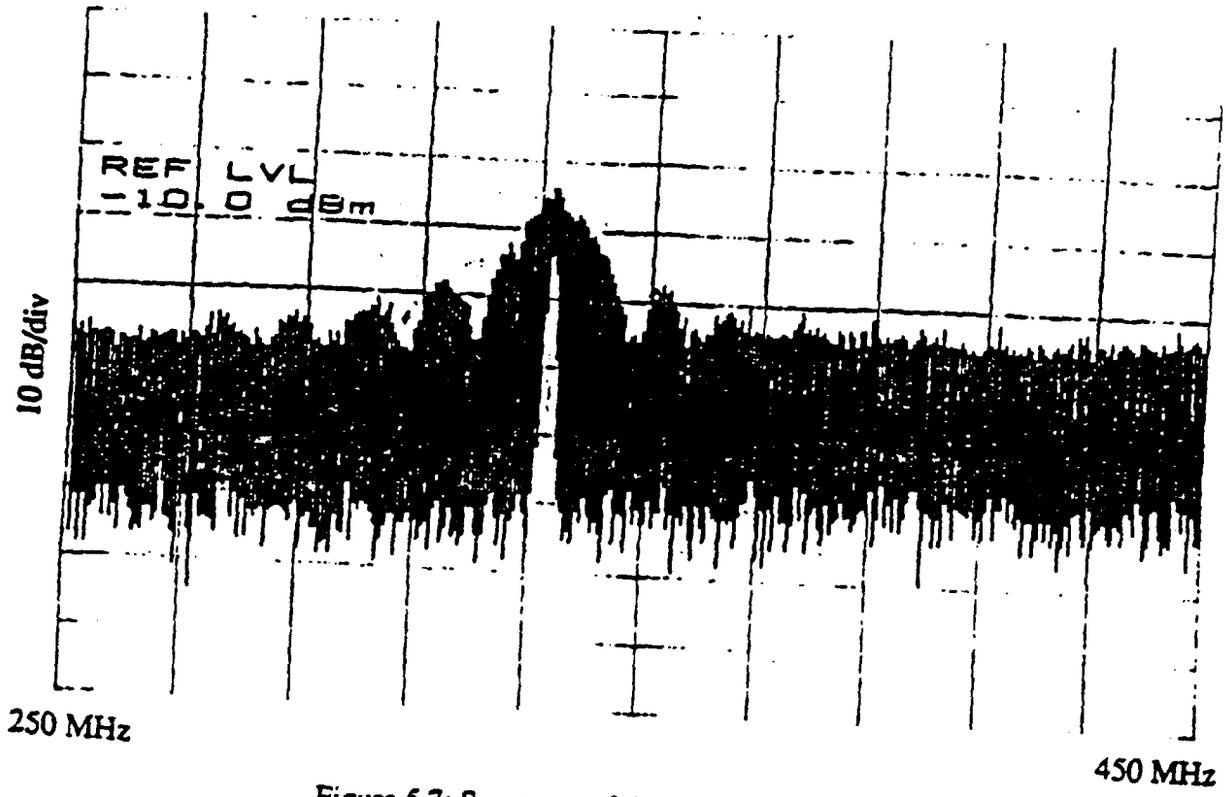

Figure 5.7: Spectrum of the 78 ns pulse

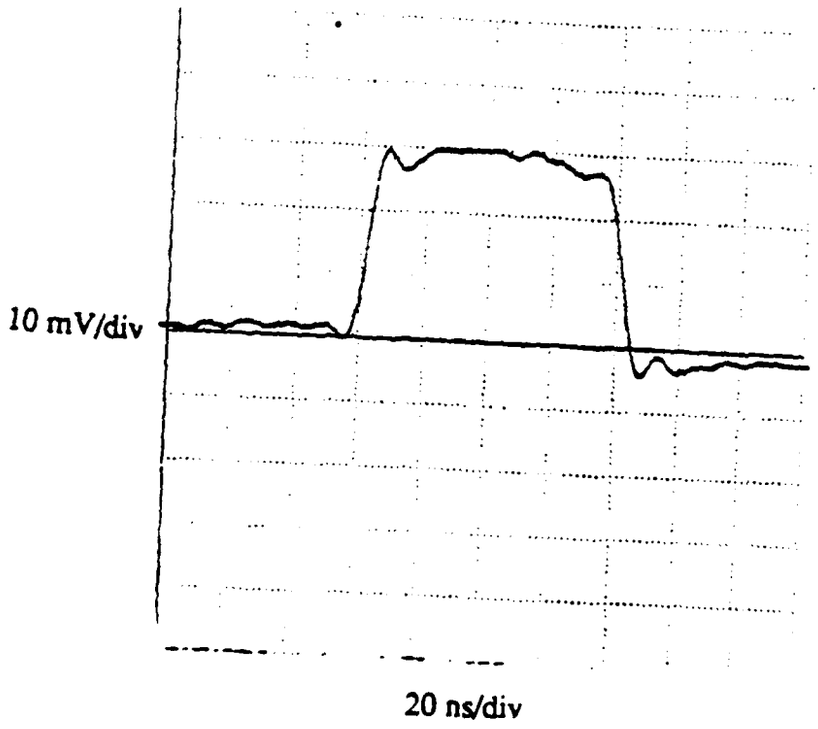

Figure 5.8: The experimental reference pulse

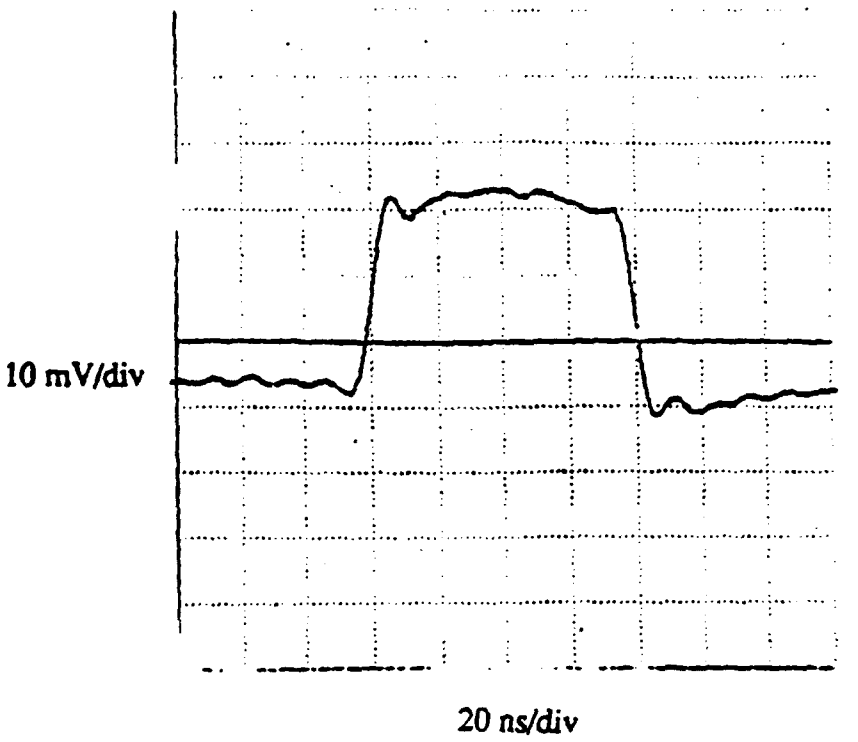

Figure 5.9: The 78 ns pulse with the d.c. value removed

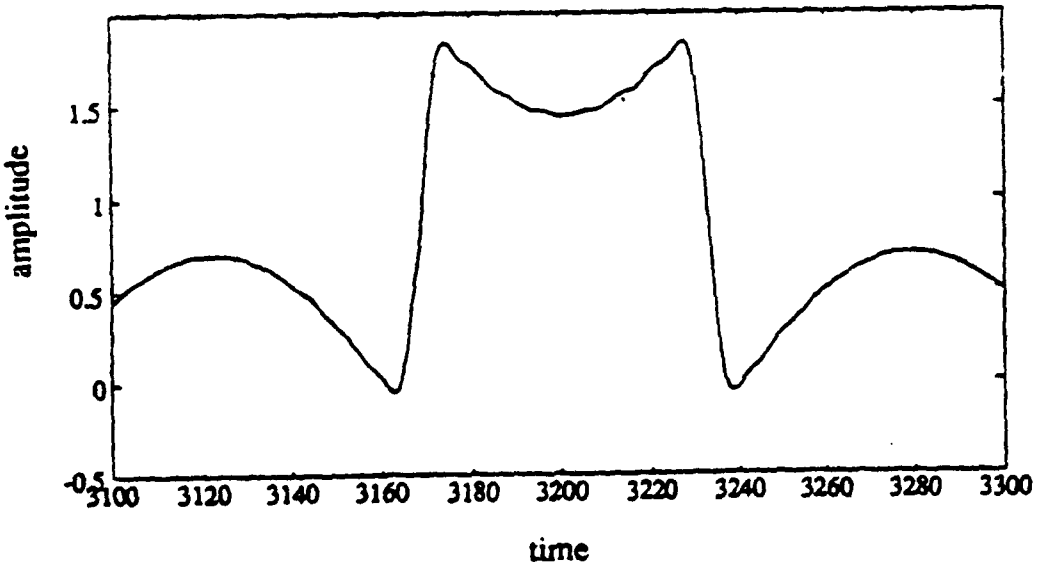

(a) Computer simulation result: spatial light modulator elements 345 and 355 switched

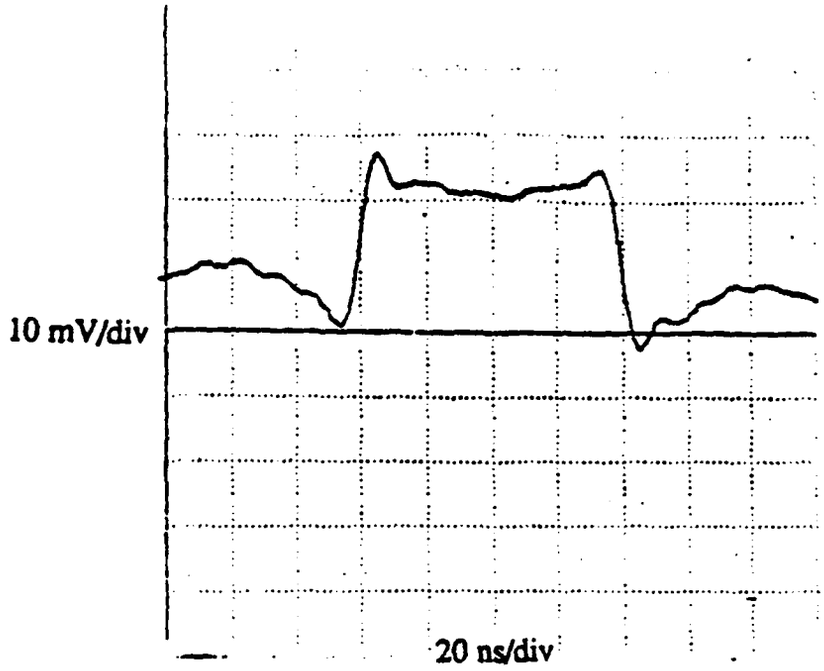

(b) Experimental result: spatial light modulator elements 345 and 355 switched

Figure 5.10: The 78 ns pulse with a symmetric removal of frequency components

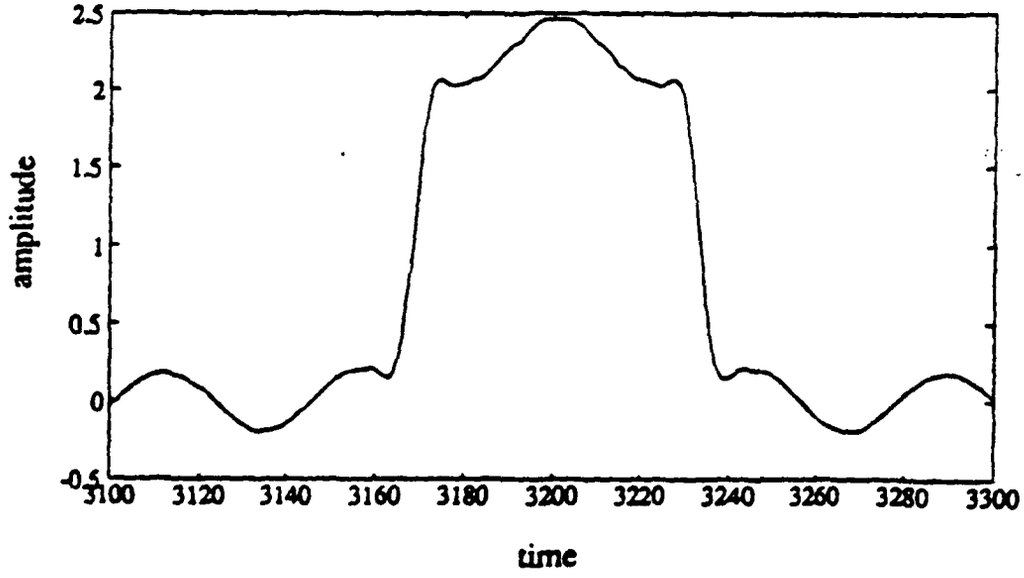

(a) Computer simulation result: spatial light modulator elements 332 and 368 switched

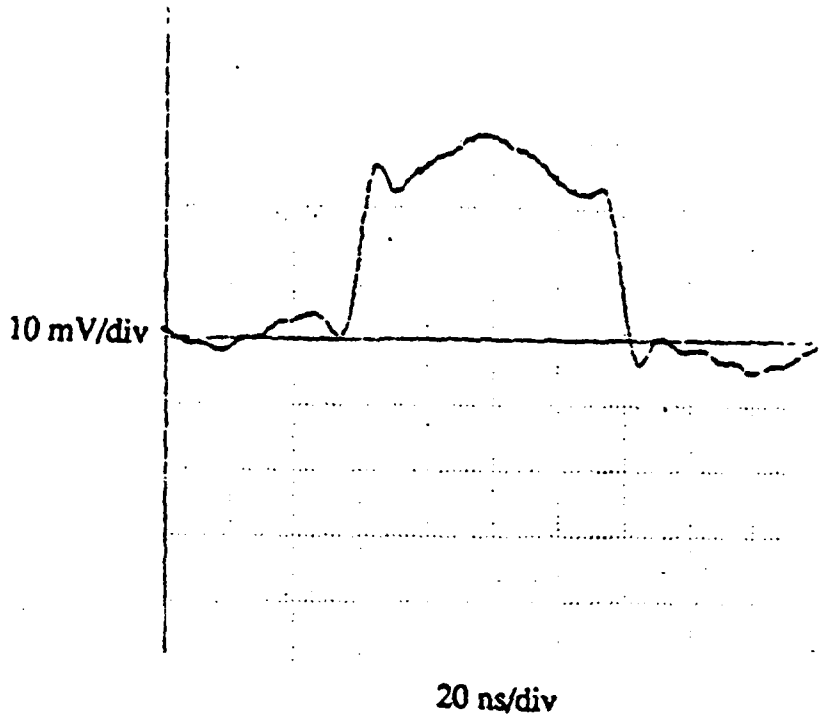

(b) Experimental result: spatial light modulator elements 332 and 368 switched

Figure 5.11: The 78 ns pulse with a symmetric removal of frequency components in the sidelobes

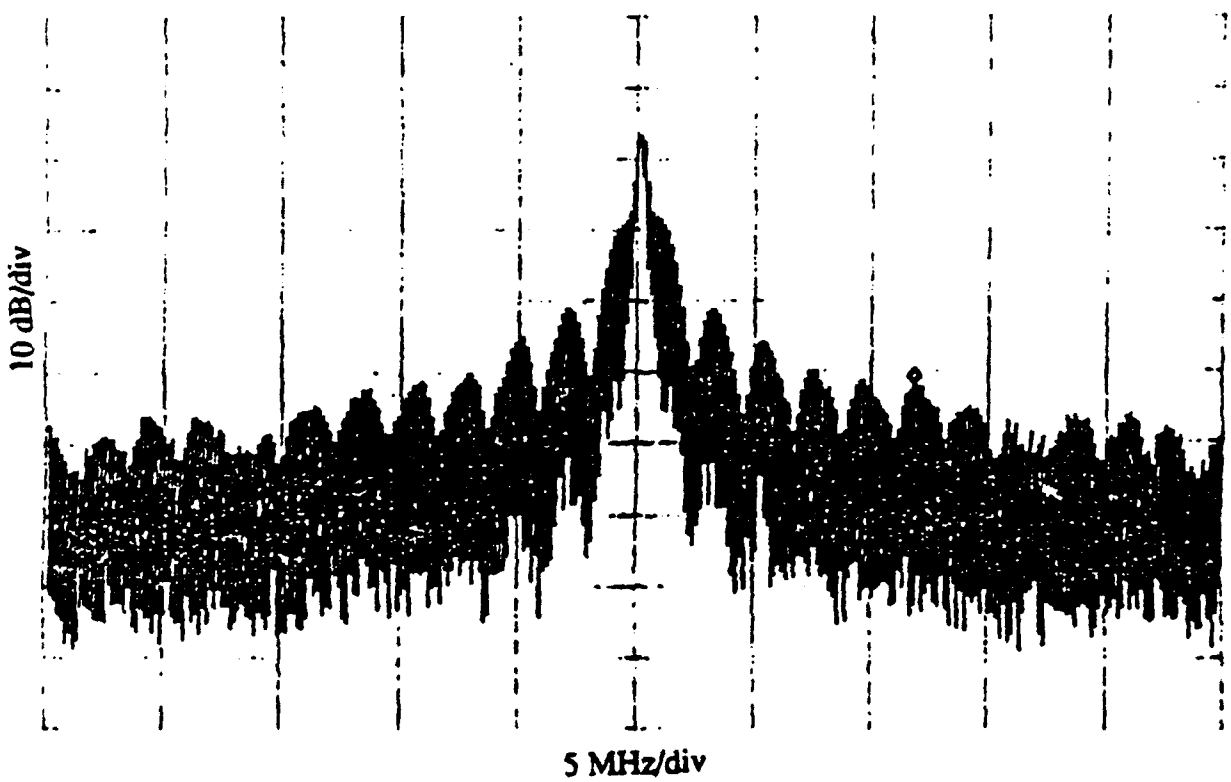

Figure 5.12: Spectrum of the 468 ns pulse

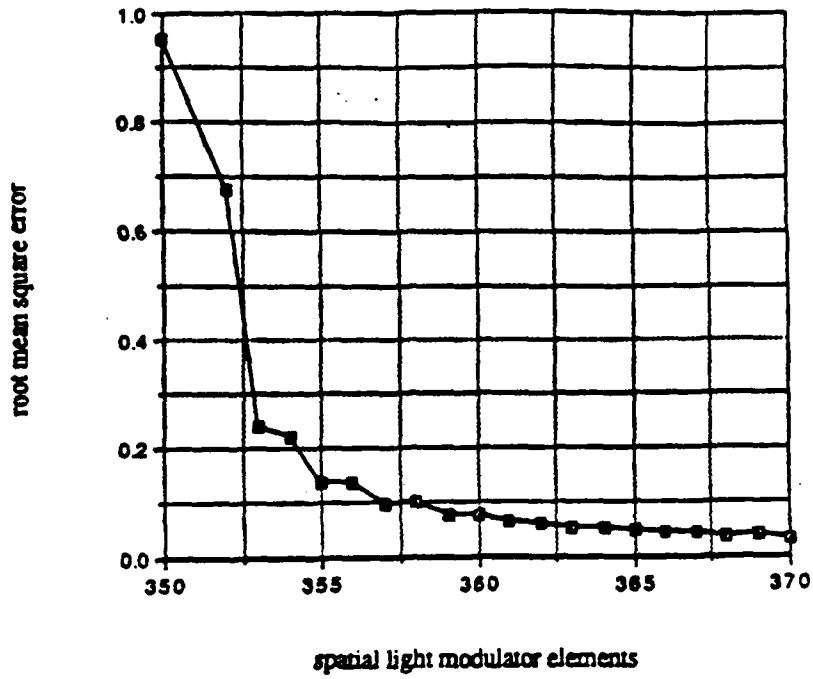

(a) Computer simulation: root mean square error versus spatial light modulators elements

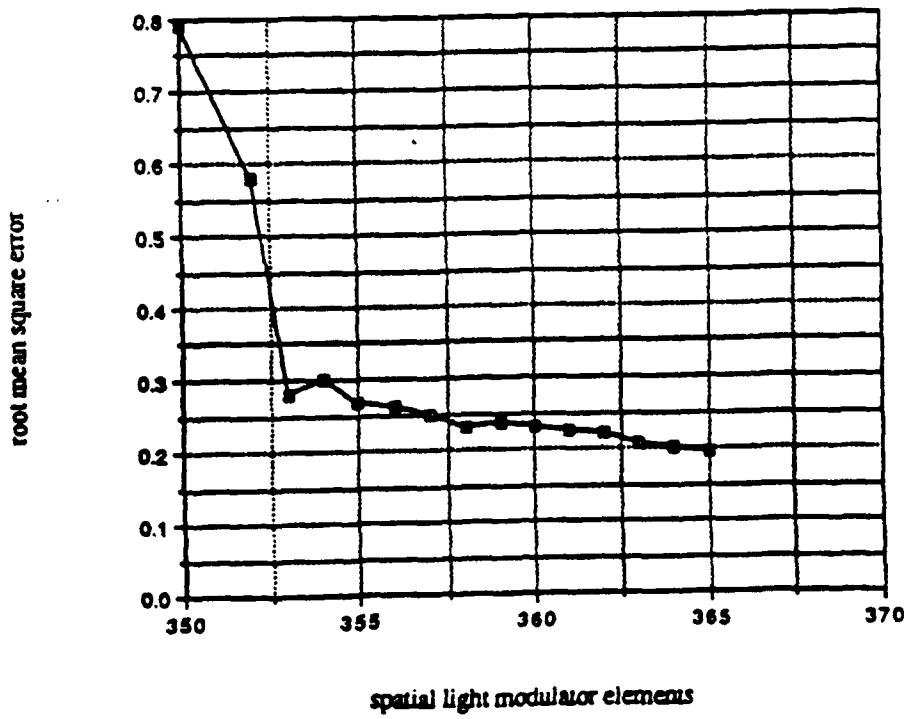

(b) Experimental results: root mean square error versus spatial light modulators elements

Figure 5.13: Root mean square error of the 468 ns pulse

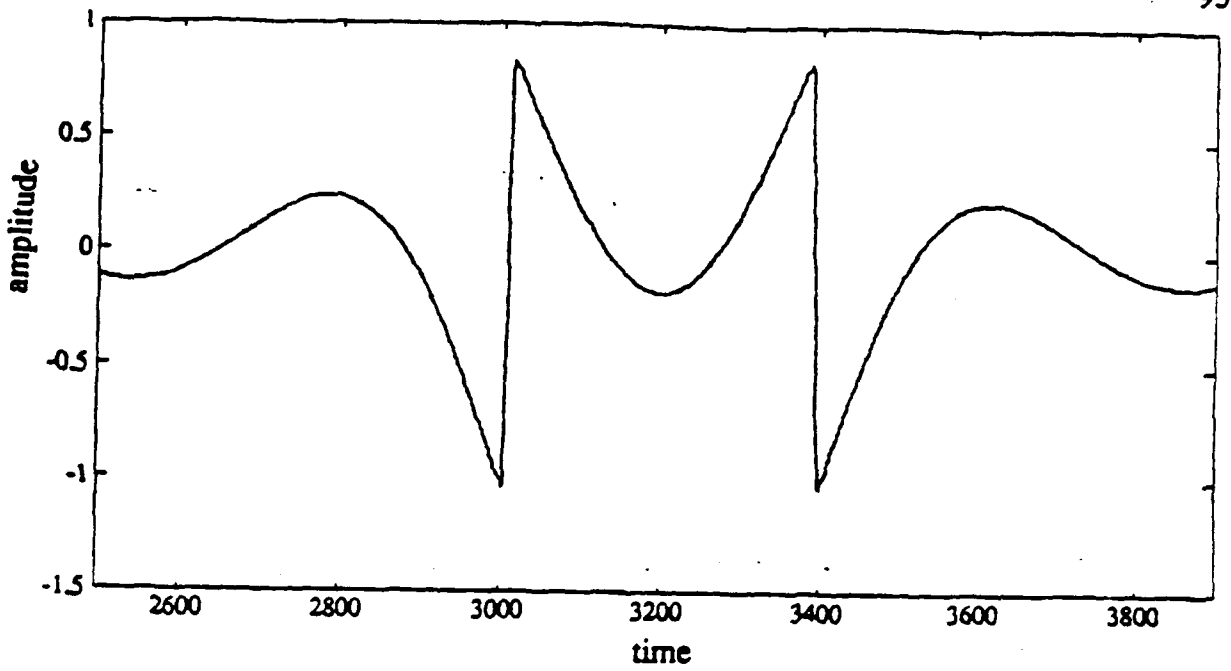

(a) Computer simulation result

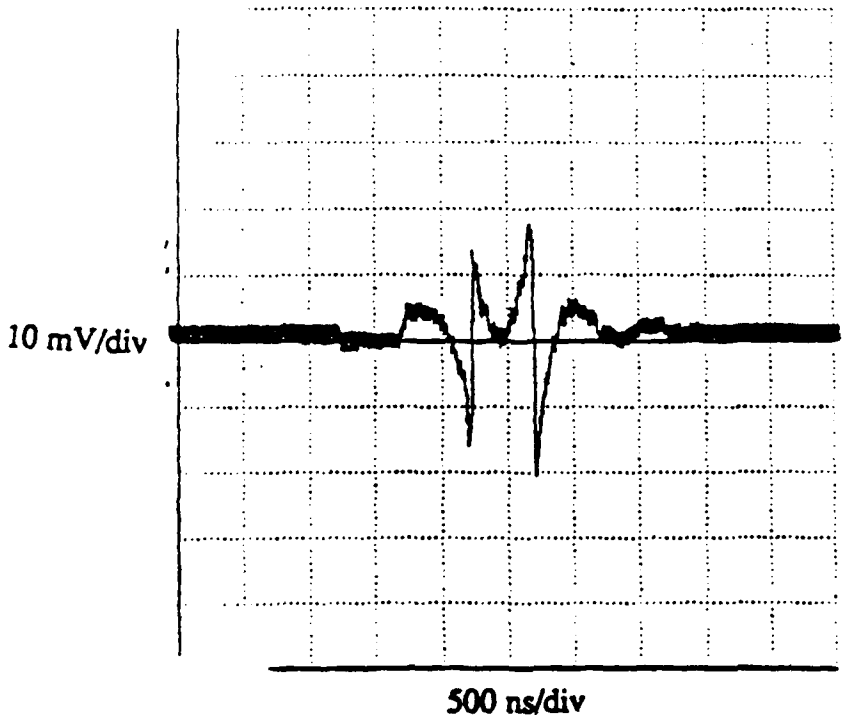

(b) Experimental result

Figure 5.14: The 468 ns pulse when the three centered spatial light modulator elements are switched

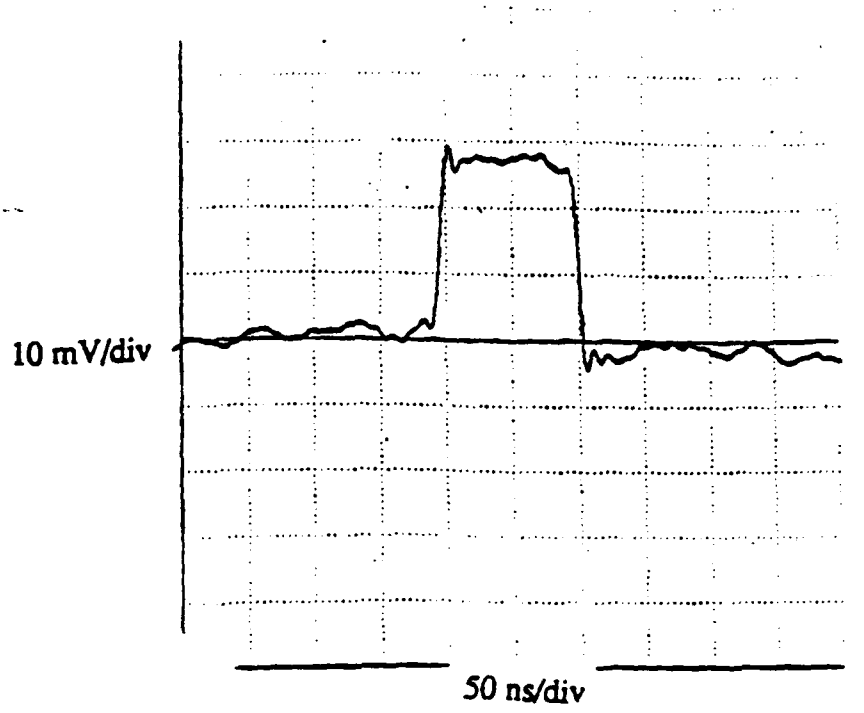

Figure 5.15: The reference 100 ns pulse

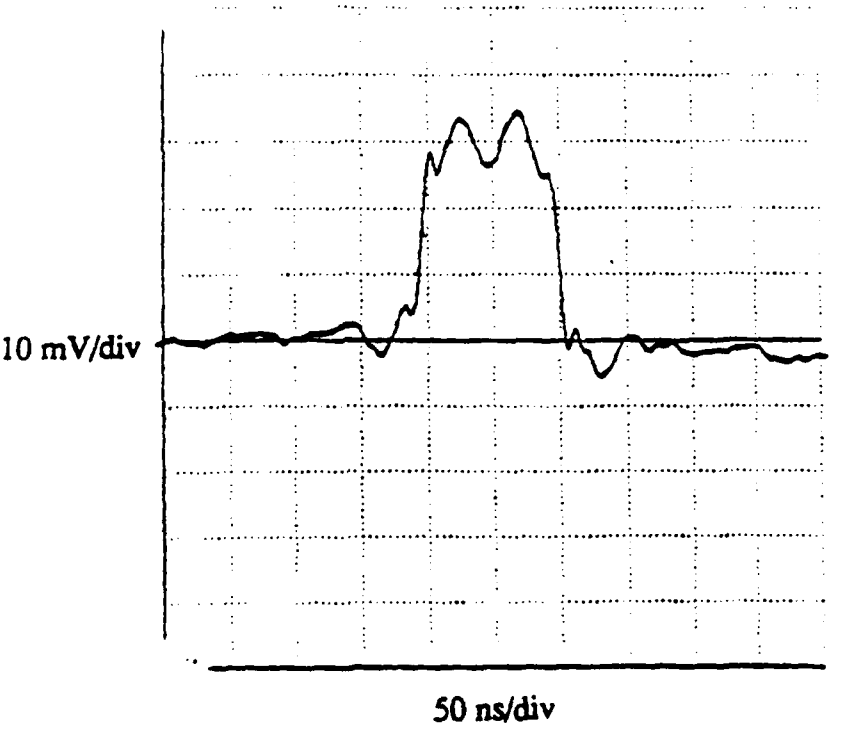

Figure 5.16: The 100 ns pulse when the second sidelobes are removed

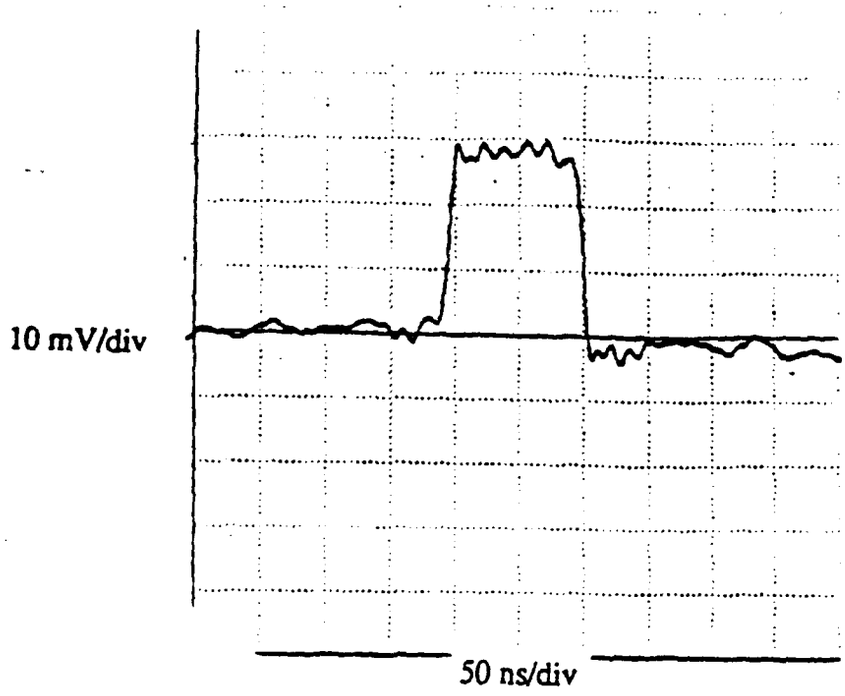

Figure 5.17: The 100 ns pulse with the sixth sidelobes removed

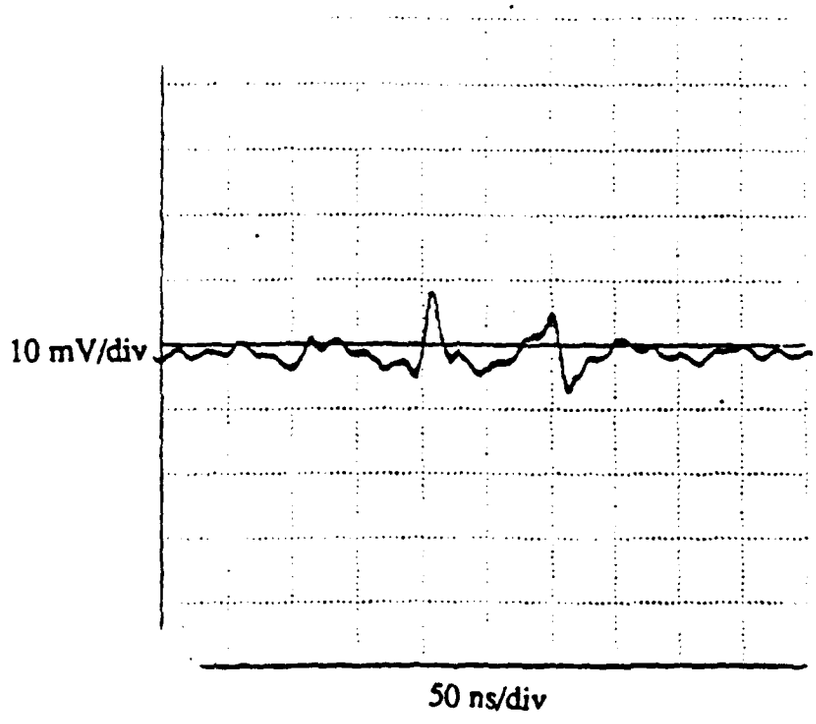

(a) The 100 ns pulse with the mainlobe removed

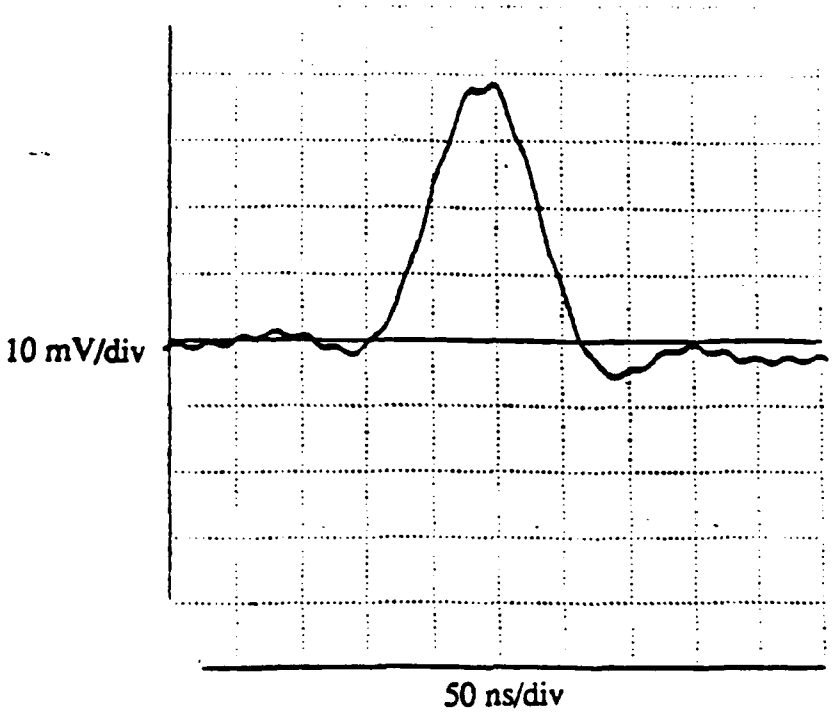

(b) The 100 ns pulse with all the sidelobes removed

Figure 5.18: The experimental 100 ns pulse with various sidelobes removed

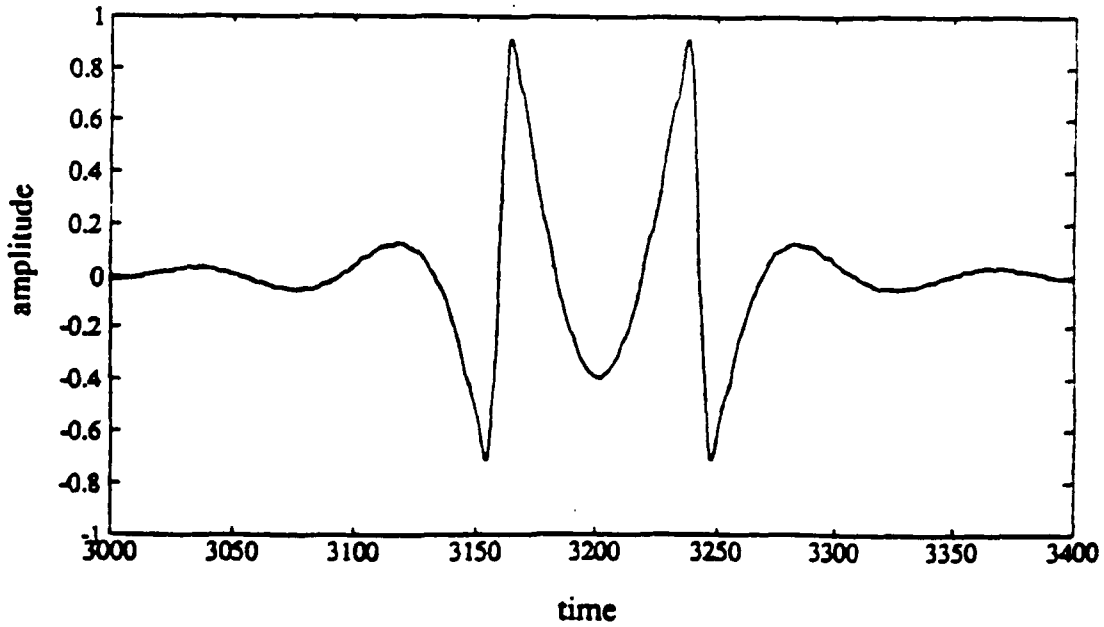

(a) Computer simulation result of the 100 ns pulse with the mainlobe removed

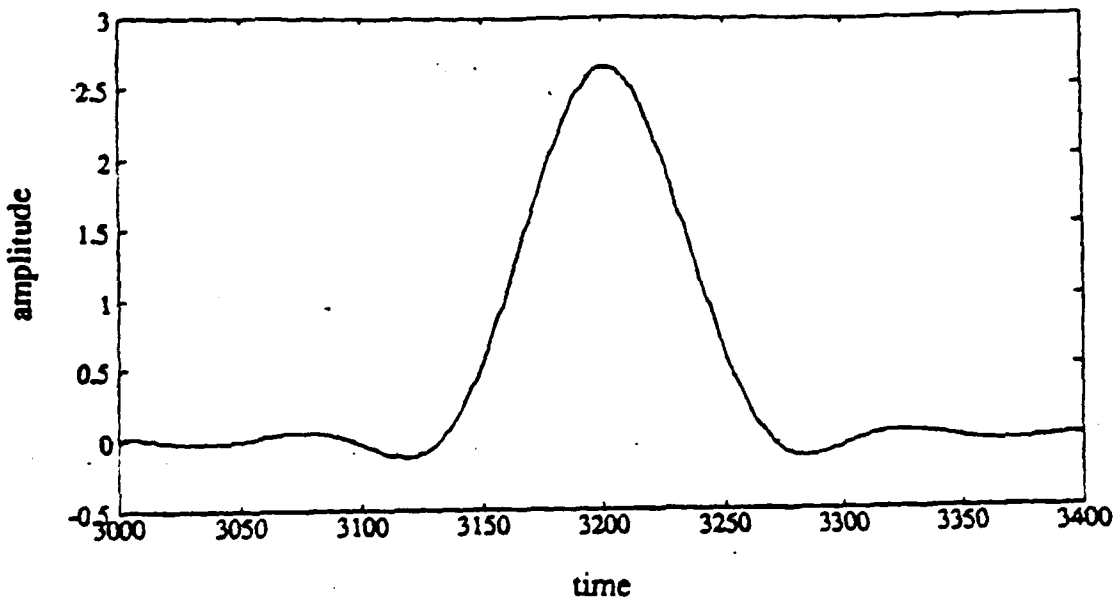

(b) Computer simulation result of the 100 ns pulse with the sidelobes removed

Figure 5.19: The computer simulations of the 100 ns pulse with various sidelobes removed

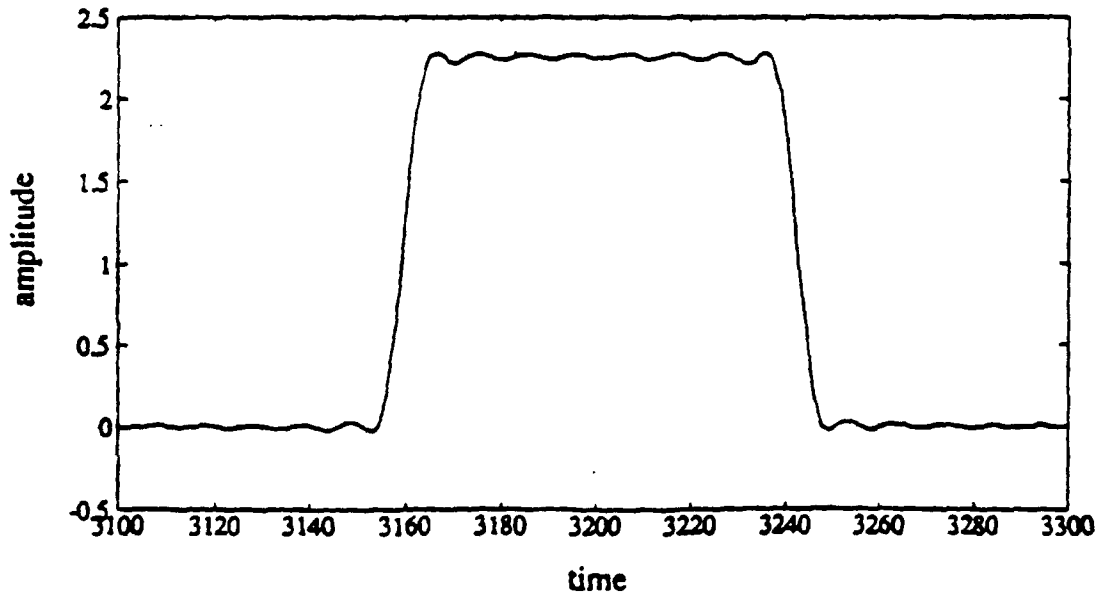

(a) Computer simulation result of the 100 ns pulse with seven sidelobes

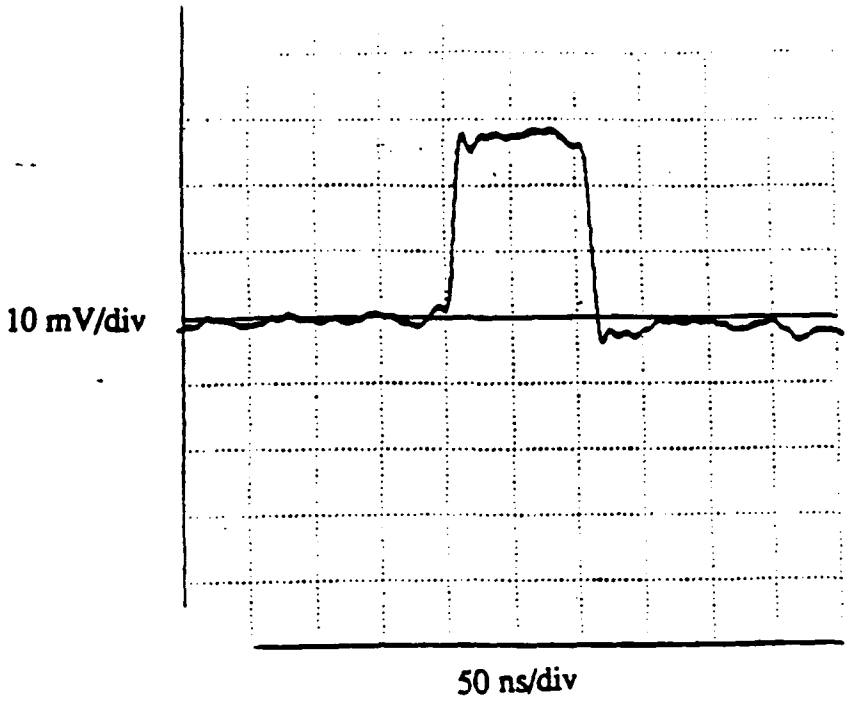

(b) Experimental result of the 100 ns pulse with seven sidelobes

Figure 5.20: The 100 ns pulse with seven sidelobes

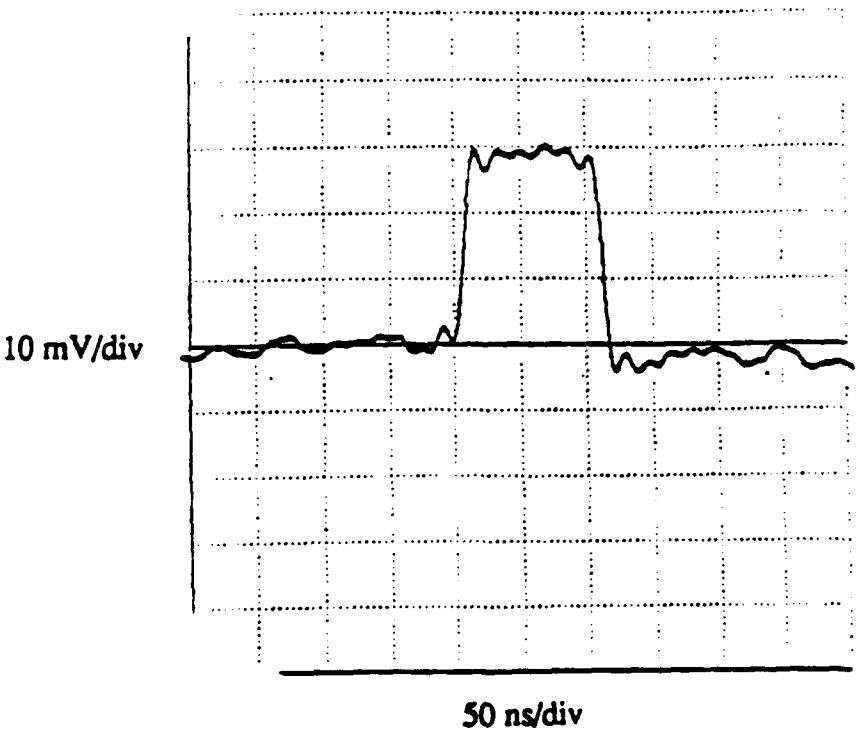

Figure 5.21: The experimental 100 ns pulse with five sidelobes

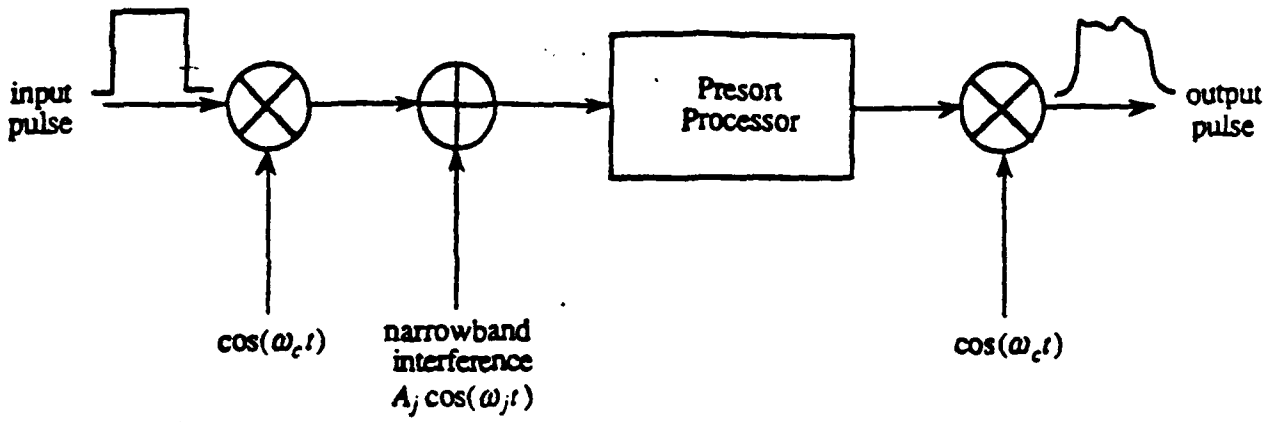

Figure 5.22: The experimental setup for the narrowband interference experiments

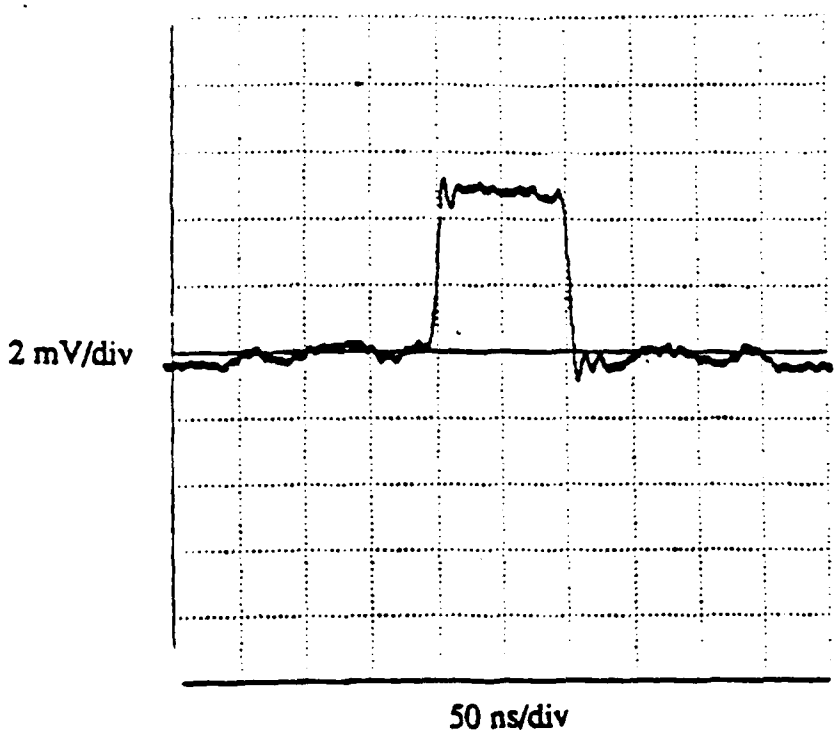

Figure 5.23: The reference pulse for the narrowband interference experiments

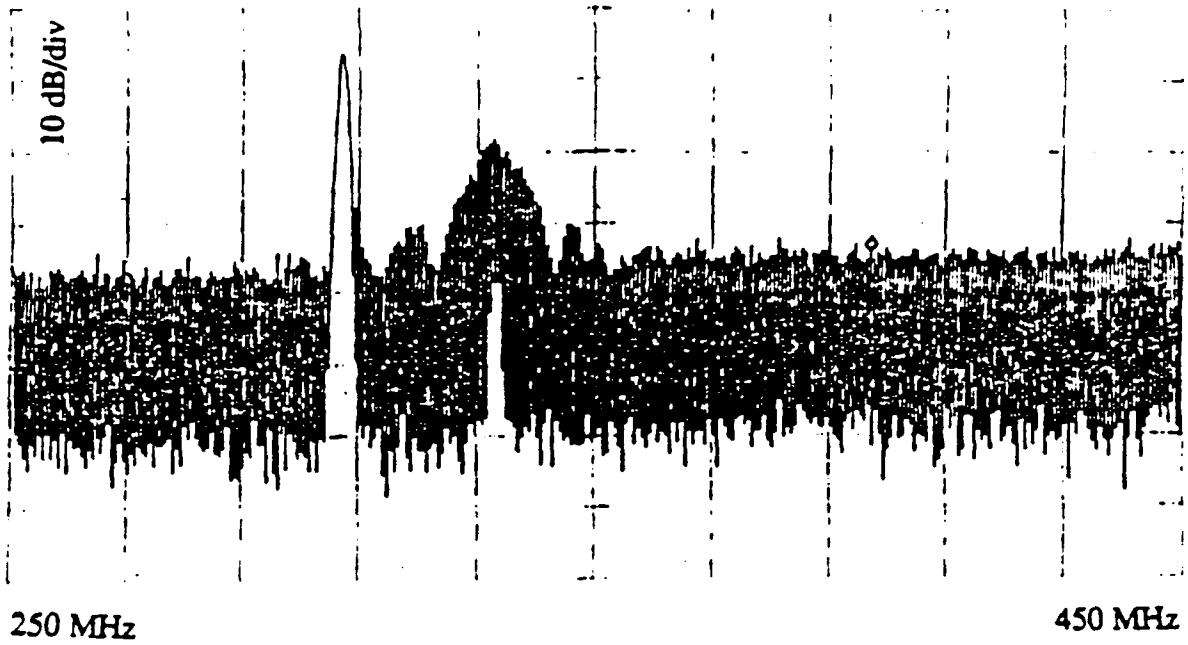

Figure 5.24: The spectrum of the pulse plus the narrowband interferer

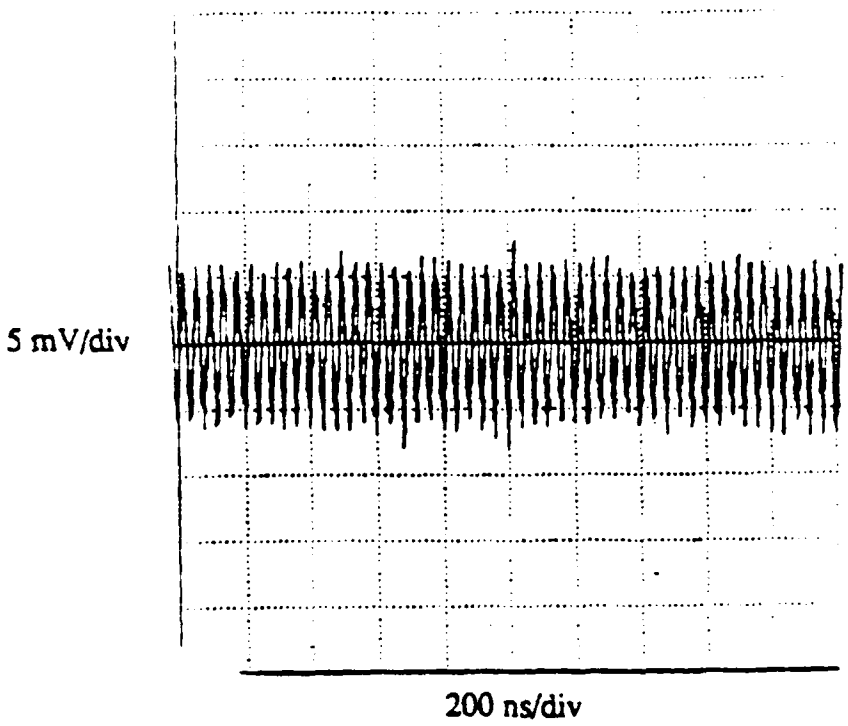

Figure 5.25: The pulse plus the narrowband interferer after demodulation

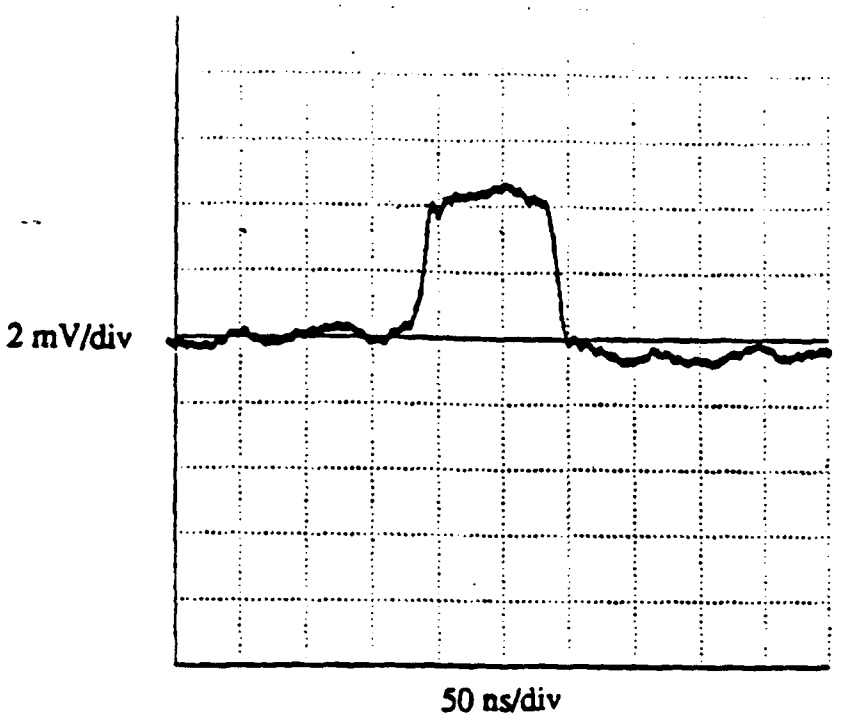

Figure 5.26: The pulse with the narrowband interferer excised

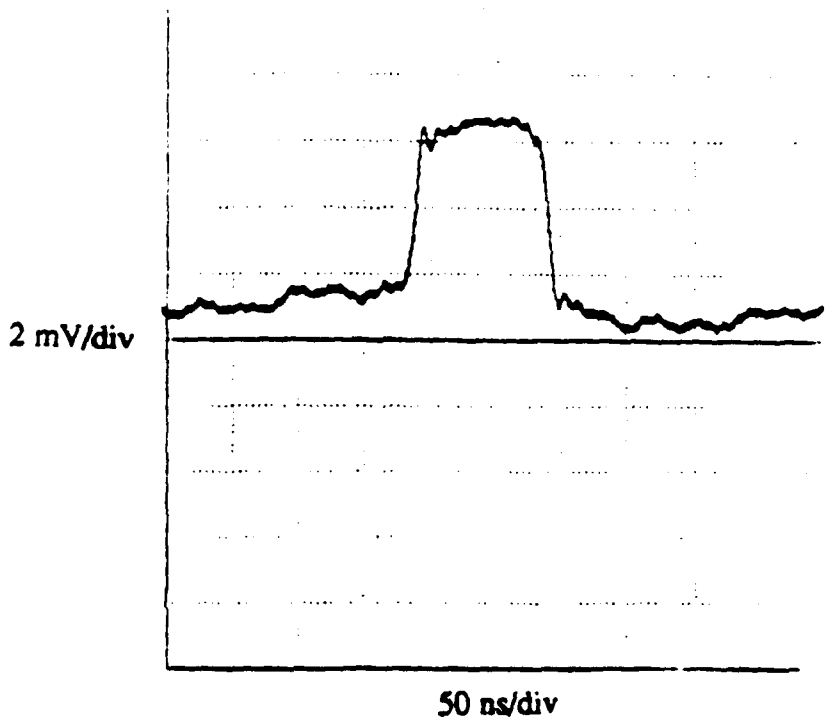

Figure 5.27: The pulse with the narrowband interferer at 304.5 MHz excised

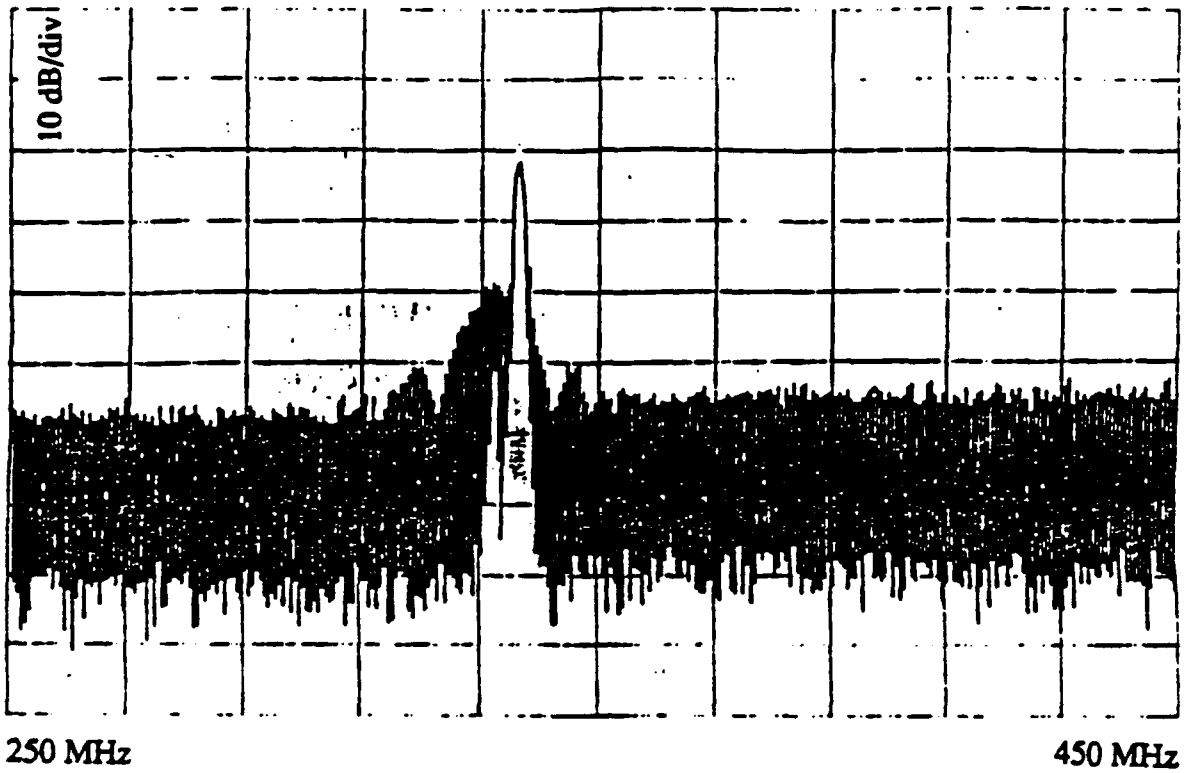

Figure 5.28: Spectrum of the pulse plus the narrowband interferer in the mainlobe

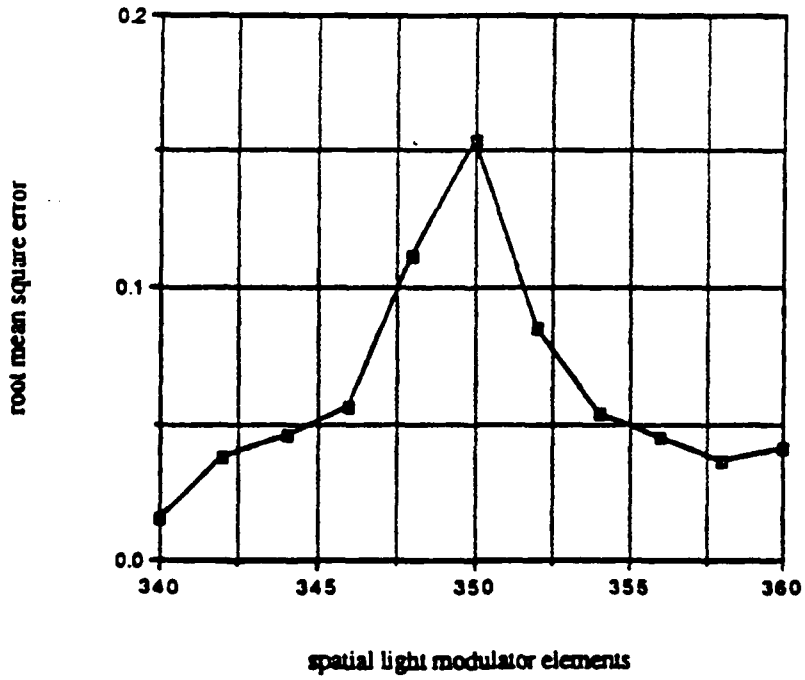

Figure 5.29: The root mean square error versus spatial light modulator elements with the narrowband interferer in the mainlobe

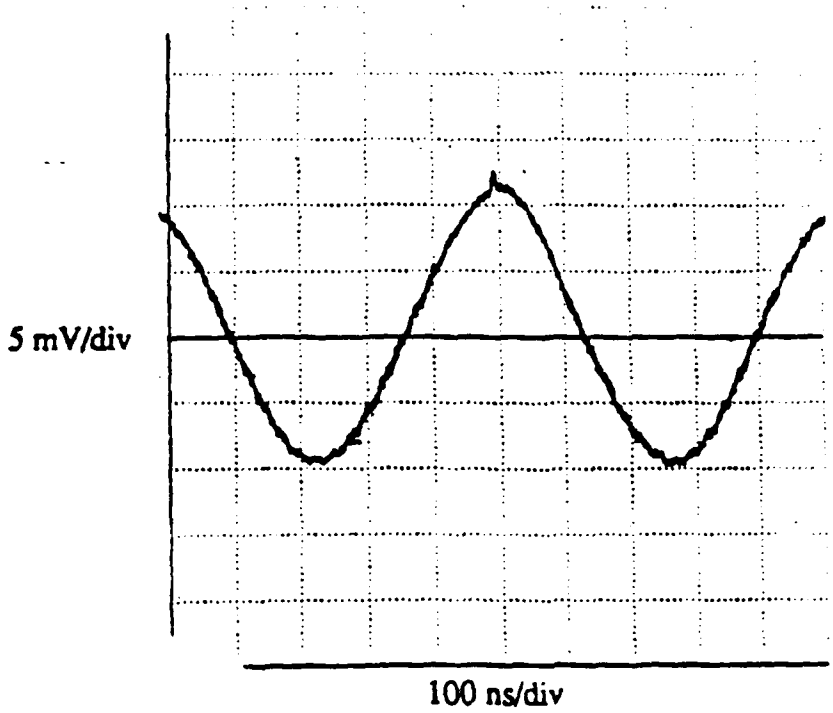

Figure 5.30: The pulse plus the narrowband interferer 2 MHz from the modulating frequency

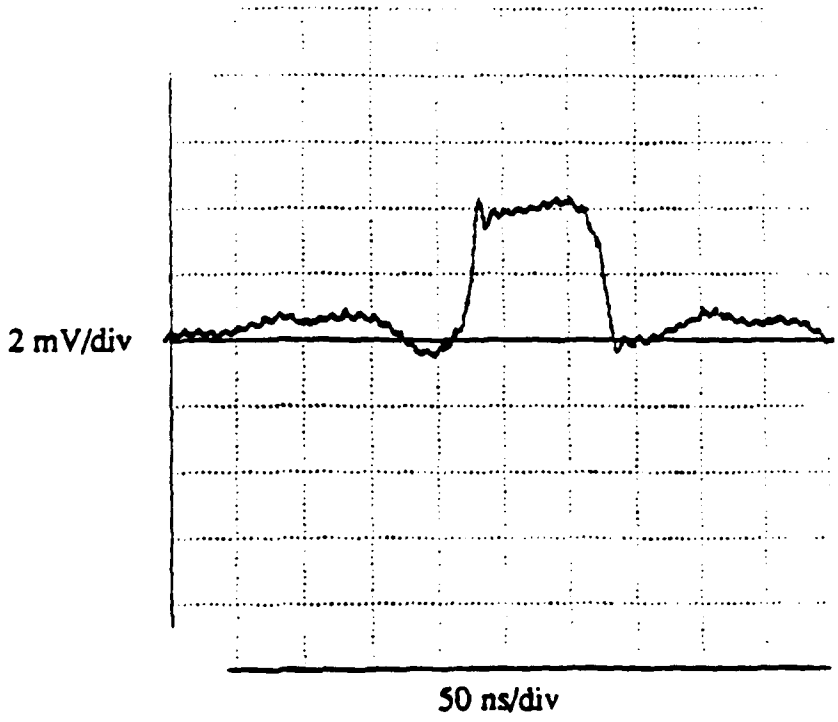

Figure 5.31: The pulse with the narrowband interferer excised: RMSE=0.15

MISSION

OF

ROME LABORATORY

Rome Laboratory plans and executes an interdisciplinary program in research, development, test, and technology transition in support of Air Force Command, Control, Communications and Intelligence (C^3I) activities for all Air Force platforms. It also executes selected acquisition programs in several areas of expertise. Technical and engineering support within areas of competence is provided to ESD Program Offices (POs) and other ESD elements to perform effective acquisition of C^3I systems. In addition, Rome Laboratory's technology supports other AFSC Product Divisions, the Air Force user community, and other DOD and non-DOD agencies. Rome Laboratory maintains technical competence and research programs in areas including, but not limited to, communications, command and control, battle management, intelligence information processing, computational sciences and software producibility, wide area surveillance/sensors, signal processing, solid state sciences, photonics, electromagnetic technology, superconductivity, and electronic reliability/maintainability and testability.